Conseil Européen pour la Recherche Nucléaire (CERN)

Baryon Antibaryon Symmetry Experiment (BASE)

Summer Student Report

Potential Studies

Temperature Evaluation

Author:
Timm Kielinski

Supervisor:
Stefan Ulmer

September 26, 2019

Table of Contents

1. Introduction

The aim of every theory is to construct a framework to describe the world correctly. Unfortunately, despite all attempts, there exists no theory which is able to fully explain all physical phenomena. So far the best model in particle physics is the Standard Model (SM) which unifies three of the four fundamental forces, i.e. electromagnetic, weak and strong interactions. The first unified fundamental force was electromagnetism described by Maxwell [1] in 1865. More than half a decade later, in 1934, Fermi started the development of the weak interaction with his ideas on β-decay [2]. A few years later, in the 1960s, Glashow [3], Salam [4] and Weinberg [5] combined the electromagnetic force and weak interaction in the frame of electroweak unification and received the Nobel Prize in 1979. In the 70s the strong interaction was added and the full Standard Model was born [6]. Although the Standard Model is believed to be self-consistent and its remarkable ability to predict many experimental results its known to be incomplete [7]. Beside not including General Relativity (GR) there are also several phenomena which the Standard Model can not explain. For example it can not explain neutrino oscillations and masses [8, 9]. Furthermore according to data analysis of the PLANCK space telescope only 5% of the universe can be explained by the Standard Model where the other 95% are made of dark matter and energy [8]. Moreover, the Standard Model can not explain the matter-antimatter asymmetry in the universe. The underlying fundamental symmetry of the Standard Model is the CPT-invariance which implies that the relativistic quantum field theories of the Standard Model are invariant under the combined transformation of charge (C), parity (P) and time (T) [10]. As a direct consequence matter particles and the corresponding antimatter particles should have the same properties but conjugated charge. Consequently matter and antimatter should have been created evenly during the Big Bang. Therefore the observed matter-antimatter asymmetry is in strong contraction to the Standard Model. To find the source of this imbalance between matter and antimatter nowadays many experiments are testing CPT-symmetry. For this purpose the Baryon Antibaryon Symmetry Experiment (BASE), which is located in the Antiproton Decelarator (AD) at the Conseil Européen pour la Recherche Nucléaire (CERN), measures and compares fundamental properties of the proton and antiproton as the charge to mass ratio q/m and the g-factor.

Charge to Mass Ratio

The charge to mass ratio q/m is related to the free cyclotron frequency ω_c as

$$\frac{q}{m} = \frac{\omega_c}{B} \tag{1.1}$$

where B denotes the external magentic field of the Penning trap.

g-factor

The g-factor is a dimensionless proportionality constant of the magnetic moment $\vec{\mu}_S$ and the spin $\vec{S}$

$$\vec{\mu}_s = g\frac{q}{2m}\vec{S}. \tag{1.2}$$

Considering the free cyclotron frequency ω_c (1.1) and the Larmor frequency

$$\omega_L = \frac{g}{2}\frac{q}{m}B \tag{1.3}$$

the g-factor can be expressed as

$$\frac{g}{2} = \frac{\omega_L}{\omega_c}. \tag{1.4}$$

The overall structure is as follows. In section 2 a theoretical description of the Penning trap is given. Frequency shifts due to electrostatic anharmonicities are derived in section 3 and then discussed on a theoretical basis for the current Penning trap used at BASE in section 4. In section 5 the basic detection principle in the BASE experiment is presented. A method to evaluate the temperature of the system is developed in section 6. In section 7 the idea of phase sensitive methods is presented and fundamental measurements are discussed.

Since my internship was during the large shutdown due to the high luminosity upgrade of the Large Hadron Collider (LHC), the Antiproton Decelerator (AD) was not working. Therefore the BASE team worked only with protons instead of antiprotons. Consequently in the following always protons are considered as long as it is not explicitly said that anitprotons are considered.
During the whole work Wolfram Mathematica is used as a computer algebra system since it combines analytical and numerical computing routines which both were used by turns.

2. Penning Trap

The origin of the name 'Penning trap' goes back to F. M. Penning in 1936 whose work was pioneering for the later development of the Penning trap. During his work on improvements of the sensitivity of vacuum gauges, he had the idea to add a magnetic field which forces the electrons on a circular orbit. The gauge chamber is realised by two cylindrical tubes where the inner one is the anode and the outer one is the cathode. If the imposed magnetic field is high enough, the electron emitted from the cathode does not hit the anode but gets deflected to the cathode. Additionally, on its trajectory the electron collides with some remaining gas molecules inside the chamber. If the electron loses a total energy higher than the work function due to those collisions, the electron can not return to the cathode. Therefore the electron trajectory gets much larger and finally terminates at the anode [11]. In 1949 J. R. Pierce investigated Penning's idea in a more theoretical way to prevent particle losses in the magnetic field. Pierce solution was to superimpose the magnetic field with an electrostatic quadrupole potential [12]. Finally in 1959 H. G. Dehmelt build and used such a device for electron storage for the first time [13]. In the following years Dehmelt and his colleagues continued developing the Penning trap and operated a number of spectroscopic measurements. Furthermore Dehmelt performed first precision measurements, e.g. measuring the magnetic moment of the electron and positron [14, 15]. In 1989 Dehmelt, together with W. Paul and N. F. Ramsey, was awarded with the Nobel Prize for developing the ion trap technique [16].

Today the Penning trap has become an essential device in the field of fundamental precision measurements and is the main tool in the BASE experiment.

2.1. The Ideal Penning trap

The Penning trap consists of a superposition of a electrostatic and magnetic field as mentioned before. The reason to use such a combination of both types of fields instead of a single field is the fact that neither a static electric or magnetic field in isolation can trap a charged particle.
Trying to realise a trap only using a magnetic field the particle could escape in the direction parallel to the field lines since the Lorentz force only acts in the plane perpendicular to the field lines. In the case of using an electrostatic field in isolation the inability to trap the particle is a consequence of the Earnshaw-theorem [17]. Nowadays it can be

understood as a direct consequence of Maxwell's equations [1]. If an electrostatic potential in isolation is considered to trap a charged particle, the field lines around such a equilibrium position have to point inwards, i.e. to the equilibrium position. This would lead to a negative divergence $\vec{\nabla} \cdot \vec{E}$ of the electric field which is in direct conflict with Maxwell's equation $\vec{\nabla} \cdot \vec{E} = 0$ which states that the divergence of an electrostatic field in absence of any additional charges has to vanish. Consequently there are no local maxima or minima such that an equilibrium position can not exist. Thus a superposition of a magnetic and electrostatic field has to be used to trap a charged particle.

The fundamental force to study the physics of the Penning trap is the Lorenz force

$$\vec{F}_L = q\left(\vec{E} + \vec{v} \times \vec{B}\right) \tag{2.1}$$

acting on a particle with charge q and velocity $\vec{v}$. Considering only the magnetic field $\vec{B} = B\vec{e}_z$ the Lorenz force acts as a centripetal force

$$\begin{aligned} \vec{F}_L &= \vec{F}_Z && (2.2) \\ \Leftrightarrow qvB &= \frac{mv^2}{r} \text{ with } v = \omega_z r \\ \omega_c &= \frac{qB}{m} && (2.3) \end{aligned}$$

and therefore constrains the particle to an oscillation with the so called cyclotron frequency ω_c perpendicular to the magnetic field. For a complete description of the particle in the Penning trap the quadrupole field

$$\begin{aligned} \phi(z,\rho) &= V_r C_2 \left(z^2 - \frac{\rho^2}{2}\right) \text{ with } \rho = \sqrt{x^2+y^2} && (2.4) \\ \Leftrightarrow \vec{E}(z,\rho) &= -\nabla\phi(z,\rho) \\ &= -2V_r C_2 \left(z\vec{e}_z - \frac{\rho}{2}\vec{e}_\rho\right) \\ &= -2V_r C_2 \left(z\vec{e}_z - \frac{x}{2}\vec{e}_x - \frac{y}{2}\vec{e}_y\right) && (2.5) \end{aligned}$$

must be added, where V_r is the voltage of the ring electrode and C_2 is a trap specific parameter with the dimension of inverse length which is specified later. The electrostatic potential saddle created in the Penning trap is shown in Figure 2.1.

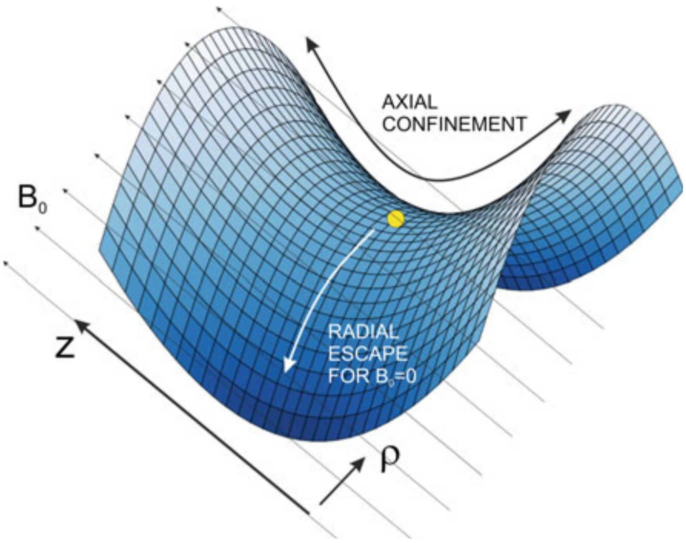

Figure 2.1: Ideal electrostatic potential in the Penning trap [18].

Taking into account the magnetic and electrostatic field the Lorenz force leads to a set of coupled equations of motion

$$\begin{aligned} m\ddot{\vec{r}} &= q\left(\vec{E} + \vec{v}\times\vec{B}\right) \\ \Leftrightarrow m\begin{pmatrix}\ddot{x}\\ \ddot{y}\\ \ddot{z}\end{pmatrix} &= q\begin{pmatrix}2V_rC_2\frac{x}{2} + \dot{y}B\\ 2V_rC_2\frac{y}{2} - \dot{x}B\\ -2V_rC_2z\end{pmatrix} \\ \Leftrightarrow \begin{pmatrix}\ddot{x}\\ \ddot{y}\\ \ddot{z}\end{pmatrix} &= \begin{pmatrix}\frac{\omega_z^2}{2}x + \omega_c\dot{y}\\ \frac{\omega_z^2}{2}y - \omega_c\dot{x}\\ -\omega_z^2 z\end{pmatrix} \end{aligned} \tag{2.6}$$

with the axial frequency defined by

$$\omega_z = \sqrt{\frac{2qV_rC_2}{m}}. \tag{2.7}$$

The axial motion is simply given by a harmonic oscillator with frequency ω_z and can be tuned by changing the ring voltage V_r. To decouple the equations of motion for the radial direction the change of variables $u = x + iy$ can be performed. This leads to the combined equation of motion

$$\ddot{u} + i\omega_c \dot{u} - \frac{\omega_z^2}{2} u = 0. \tag{2.8}$$

Now a simple exponential ansatz $e^{i\omega t}$ can be used which, combined with the differential equation, leads to

$$\omega^2 - \omega_c \omega + \frac{\omega_z^2}{2} = 0 \tag{2.9}$$

$$\Rightarrow \quad \omega_\pm = \frac{1}{2}\left(\omega_c \pm \sqrt{\omega_c^2 - 2\omega_z^2}\right). \tag{2.10}$$

Consequently the eigenmodes of the radial motion are the so called modified cyclotron frequency ω_+ and magnetron frequency ω_-. From (2.10) it is easy to see that stable particle storage requires the condition

$$\omega_c^2 - 2\omega_z^2 \geq 0 \Leftrightarrow V_r < \frac{qB^2}{4mC_2}. \tag{2.11}$$

However, this property can be useful to remove particle species with a higher $\frac{q}{m}$ ratio, i.e. protons and antiprotons have a much higher mass than electrons and therefore it is easy to get rid of electrons which contaminate the Penning trap by lowering the ring voltage V_r below the given threshold.
For the physical understanding it is helpful to point out a more general solution of the differential equation (2.8). The solution can be written as

$$u(t) = \rho_+ e^{i\omega_+ t} + \rho_- e^{i\omega_- t} \tag{2.12}$$

where ρ_+ and ρ_- denote the modified cyclotron radius and magnetron radius respectively. It shows that the radial motion is a superposition of the modified cyclotron and magnetron oscillation. The expressions for $x(t)$ and $y(t)$ can be found by considering the real and imaginary part of the solution $u(t)$:

$$x(t) = \mathrm{Re}(u(t)) = \rho_- \cos\left(\frac{\omega_-}{2} t\right) + \rho_+ \cos\left(\frac{\omega_+}{2} t\right) \tag{2.13}$$

$$y(t) = \mathrm{Im}(u(t)) = \rho_- \sin\left(\frac{\omega_-}{2} t\right) + \rho_+ \sin\left(\frac{\omega_+}{2} t\right). \tag{2.14}$$

The typical hierarchy of eigenmodes used in experiments is $\omega_+ \gg \omega_z \gg \omega_-$ and a typical trajectory of the three eigenmodes in the Penning trap is shown in Figure 2.2. Using

(2.10) relations between the eigenmodes can be derived which link ω_+, ω_z and ω_-:

$$\omega_+ + \omega_- = \omega_c \tag{2.15}$$

$$\omega_+ \omega_- = \frac{1}{2}\omega_z^2 \Leftrightarrow \omega_- = \frac{\omega_z^2}{2\omega_+}. \tag{2.16}$$

Combining those relations in $(\omega_+ + \omega_-)^2 = \omega_+^2 + 2\omega_+\omega_- + \omega_-^2$ leads to the most important one called the invariance theorem

$$\omega_c^2 = \omega_+^2 + \omega_z^2 + \omega_-^2. \tag{2.17}$$

While (2.15) and (2.16) are only valid in the ideal Penning trap, the invariance theorem (2.17) also holds in presence of trap imperfections or misalignment [19].

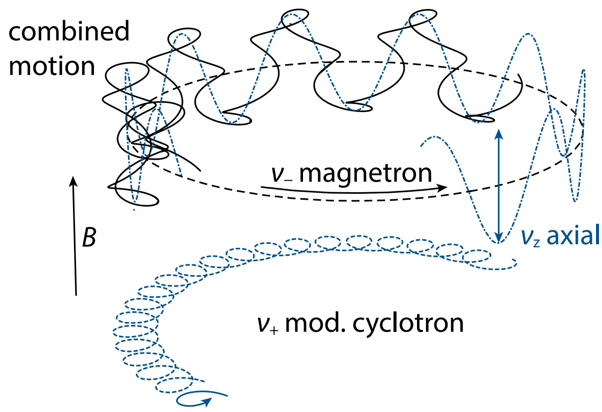

Figure 2.2: Typical trajectory of the particle in the Penning trap consisting of the three eigenmotions [20].

2.2. The Real Penning Trap

The previous section dealt with the ideal field configuration of the Penning trap. This section describes how the Penning trap is realised in the experiment to be as close as possible to the ideal case. Although a hyperbolic design [13] is used in many experiments to reproduce the shape of a quadrupole field, a cylindrical trap can also be used and has the advantage that a system of several electrodes can be easily connected, e.g. to load the trap, and furthermore cylindrical electrodes can be manufactured more precisely [21]. In the experiment a five-pole cylindrical Penning trap placed in a superconducting magnet is used. Unfortunately the resulting fields show a deviation from the ideal case. For certain choices of the trap geometry it is possible to design the trap compensated and orthogonoal, i.e.

- compensated: First higher orders of correction terms, i.e. C_4 and C_6, are simultaneously tuned to zero,
- orthogonal: The resonance frequency is independent of the voltage V_{ce} applied to the correction electrodes.

To obtain the trapping potential of such an electrode geometry potential theory can be used and the potential is given by the solution of the Laplace equation where cylindrical coordinates are used because of the given symmetry. The Laplace equation reads

$$\Delta\phi = 0 \quad \Leftrightarrow \quad \left[\frac{1}{\rho}\frac{\partial}{\partial\rho}\left(\rho\frac{\partial}{\partial\rho}\right) + \frac{1}{\rho^2}\frac{\partial^2}{\partial\varphi^2} + \frac{\partial^2}{\partial z^2}\right]\phi = 0 \tag{2.18}$$

with Dirichlet boundary conditions $\phi(a, z) = V$ where V describes the voltage applied to the electrode at position z. Due to the rotational symmetry of the trap the potential ϕ is independent of the angle φ. Moreover, the Laplace equation does not include mixed terms of derivatives, such that a simple separation ansatz $\phi(\rho, z) = R(\rho)Z(z)$ can be chosen to solve the Laplace equation. The separation yields in independent differential equations for $Z(z)$ and $R(\rho)$

$$\frac{1}{\rho}\frac{\partial}{\partial\rho}\left(\rho\frac{\partial}{\partial\rho}R(\rho)\right) - \lambda^2 R(\rho) = 0 \tag{2.19}$$

$$\frac{\partial^2}{\partial z^2}Z(z) + \lambda^2 Z(z) = 0 \tag{2.20}$$

where λ^2 denotes the separation constant. The equation for the axial as well as the radial term are well known. The solution of the axial part is given by trigonometric functions while the radial part is solved by the modified Bessel functions $I_k(\rho)$. Hence the most general solution is given by

$$\phi(\rho, z) = \sum_{n=1}^{\infty} I_0(k_n\rho)A_n \sin(k_n z) \text{ with } k_n = \frac{n\pi}{\Lambda} \tag{2.21}$$

where A_n are coefficients defined by the Dirichlet boundary conditions and Λ is the total length of the trap. After calculating the coefficients A_n [22] the total potential for a trap with p stacked electrodes reads

$$\begin{aligned}\phi(\rho,z) =& \frac{2}{\Lambda}\sum_{n=1}^{\infty}\left[\frac{V_1\cos(k_n z_0)-V_p\cos(k_n\Lambda)}{k_n}+\sum_{i=2}^{p}\frac{V_i-V_{i-1}}{k_n^2 d}\left(\sin(k_n z_{2i-2})-\sin(k_n z_{2i-3})\right)\right]\\ &\times\frac{I_0(k_n\rho)}{I_0(k_n a)}\sin(k_n z)\end{aligned} \tag{2.22}$$

where d is the distance of the gap between two adjacent electrodes, z_{2i-2} the axial start of the electrode i and z_{2i-3} the axial end of the electrode $i-1$. For the five-pole Penning trap the potential simplifies after shifting the origin to the trap centre to

$$\begin{aligned}\phi(\rho,z) =& \frac{2}{\Lambda}\sum_{n=1}^{\infty}\left[\frac{V_1\cos(k_n z_0)-V_5\cos(k_n\Lambda)}{k_n}+\sum_{i=2}^{5}\frac{V_i-V_{i-1}}{k_n^2 d}\left(\sin(k_n z_{2i-2})-\sin(k_n z_{2i-3})\right)\right]\\ &\times\frac{I_0(k_n\rho)}{I_0(k_n a)}\sin\left(k_n\left(z+\frac{\Lambda}{2}\right)\right).\end{aligned} \tag{2.23}$$

The schematic trap design, electrostatic potential and magnetic field lines are shown in Figure 2.3.

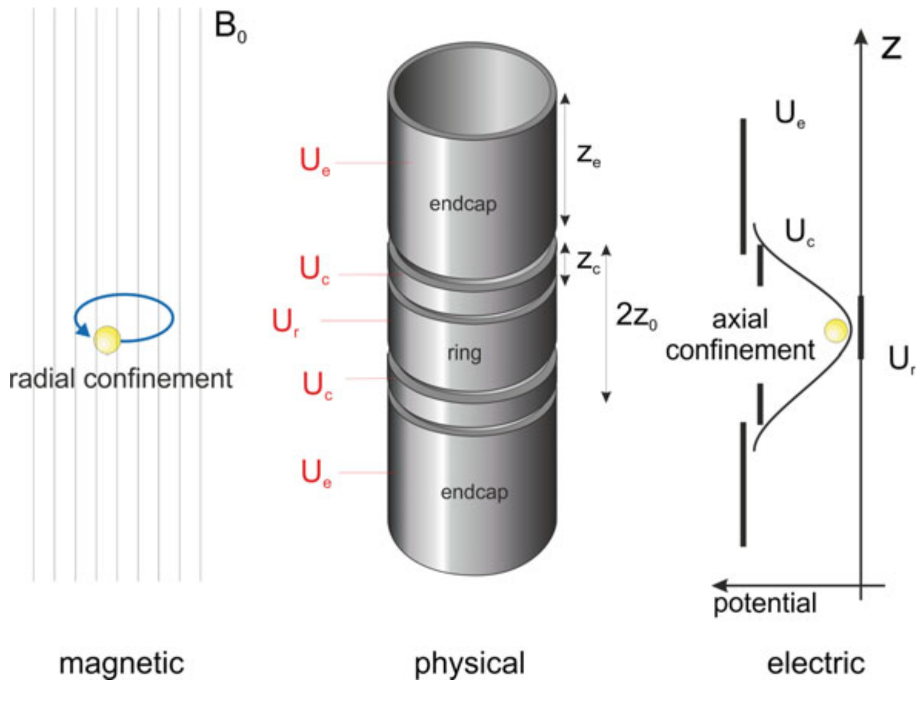

Figure 2.3: Schematic trap design, electrostatic potential and magnetic field lines [18].

As a consequence of the product structure of the potential the radial part is uniquely defined if the axial part is known. To investigate the axial potential in more detail it is convenient to Taylor expand the potential in the centre of the cylindrical trap, i.e. at $\rho = 0$:

$$\phi(0, z) = V_r \sum_{j=0}^{\infty} C_j z^j \tag{2.24}$$

where the expansion coefficients are derived in Appendix A to be

$$\begin{aligned} C_j =& \frac{2}{j! V_r \Lambda} \sum_{n=1}^{\infty} \left[\frac{V_1 \cos(k_n z_0) - V_5 \cos(k_n \Lambda)}{k_n} + \sum_{i=2}^{5} \frac{V_i - V_{i-1}}{k_n^2 d} \left(\sin(k_n z_{2i-2}) - \sin(k_n z_{2i-3}) \right) \right] \\ &\times \frac{(n\pi/\Lambda)^j}{I_0(k_n a)} \sin\left(\frac{\pi}{2}(n+j) \right). \end{aligned} \tag{2.25}$$

In the later discussion of anharmonicities coefficients C_j with j odd will be ignored since they generate forces which average to zero around a complete orbit and therefore do not produce a frequency shift to first order [23].
To be consistent with the description of the Penning trap used in the BASE experiment shown in Figure 2.4, the constraints are $V_r = V_3$, $V_{ce} = V_2 = V_4$ and $V_1 = V_5 = 0$. It is common to introduce the tuning ratio $TR = \frac{V_{ce}}{V_r}$. Since in the experiment the voltage of the ring electrode V_r is mostly fixed, the correction electrodes V_{ce} can be used to tune and optimise the potential with respect to compensation and orthogonality.
Furthermore, after grounding the endcaps it can be easily seen that if the voltage $V_{ce} = V_r \cdot TR$ is applied to the correction electrodes, the coefficients C_j can be written as

$$C_j = E_j + D_j \cdot TR \tag{2.26}$$

where E_j and D_j are coefficients and are defined by the dimensions of the trap electrodes. For an above mentioned orthogonal trap the axial frequency ω_z is independent of the tuning ratio TR, i.e. $\frac{\partial \omega_z}{\partial TR} = 0$, such that D_2 vanishes.

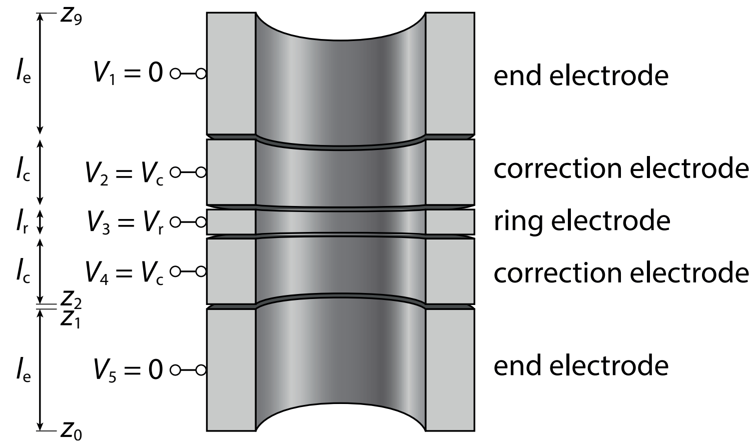

Figure 2.4: Sketch of the trap design in the BASE experiment [20].

3. Effects of Electrostatic Anharmonicities

In section 2 the ideal and real Penning trap were discussed. In contrast to the ideal Penning trap electrostatic imperfections occur in the real Penning trap. Those imperfections lead to higher order contributions to the electric field (2.24) compared to the ideal case (2.4). Unfortunately the imperfections result in amplitude dependent frequency shifts. Although the frequency shifts are not the only consequence of the imperfections, they are often the most significant one [24]. Consequently, these frequency shifts have to be well understood to estimate systematic experimental errors and eventually correct them by calibrating the contributions. To calculate the frequency shifts, rising from small imperfections, perturbation theory can be used which yields analytic formulas for the relevant parameters in the experiment. Subsequently the resulting dependencies can be used to optimise the trap with respect to the imperfections. In the case of the real Penning trap a first attempt is to obtain a compensated trap, i.e. to tune the coefficients C_4 and C_6 of the expansion of the electrostatic expansion to zero applying a voltage $V_{ce} = TR \cdot V_r$ to the correction electrodes as discussed in subsection 2.2. In conclusion, it is of great importance to examine those frequency shifts due to electrostatic imperfections.

3.1. Method of Harmonic Balance

In this section the fundamental principle of the method of harmonic balance is discussed while a detailed discussion ca be found in [25].

The method of harmonic balance is a technique to deal with approximately harmonic solutions of non-linear differential equations of the form

$$\ddot{z} + f(z) = 0 \tag{3.1}$$

where f is an arbitrary function of z. Since the problem is considered to be approximately harmonic the solution is given by

$$z(t) = Z_0 + Z_1 \cos(\omega t) + Z_2 \sin(\omega t). \tag{3.2}$$

Without loss of generality the initial condition $\dot{z}(0) = 0$ can be fulfilled and additionally Z_2 can be transformed to vanish. Thus the solution denotes

$$z(t) = Z_1 \cos(\omega t). \tag{3.3}$$

Using this solution the force reads

$$f(z) = f(Z_1 \cos(\omega t)). \tag{3.4}$$

Now the force can be expanded in terms of a Fourier series

$$f(z) = \sum_k a_k \cos(n\omega t) \approx a_1 \cos(\omega t) \tag{3.5}$$

where a_k are the Fourier coefficients and only the first one, which dominates since it is assumed to be a quasi harmonic motion, given by

$$\begin{aligned} a_1 &= \frac{2}{T} \int_0^T f(Z_1 \cos(\omega t)) \cos(n\omega t) && (3.6) \\ &= \frac{1}{\pi} \int_0^\pi f(Z_1 \cos(\omega t)) \cos(n\omega t), && (3.7) \end{aligned}$$

will be taken into account to get the first-order frequency shift. With (3.5) and (3.7) the force can be expressed as

$$f(z) = \frac{a_1}{Z_1} z. \tag{3.8}$$

Thus the differential equation (3.1) can be written as

$$\ddot{z} + \omega^2(Z_1) z = 0 \tag{3.9}$$

where $\omega(Z_1) = \frac{a_1}{Z_1}$ is the perturbed frequency of the system.
Consequently the non-linearities of the differential equation were transformed to an amplitude dependent frequency.

Example: Duffing Equation

To give a simple example which is also useful for the further calculations it is convenient to apply the formalism to the Duffing oscillator which is commonly used to model driven and damped oscillators. The equation of motion is given by

$$\ddot{z} + \omega_0^2 z + \epsilon z^3 \tag{3.10}$$

where ω_0 describes the unperturbed frequency of the oscillator and ϵ is a constant which describes the strength of the non-linearity of the restoring force. Following the algorithm above the force reads

$$f(t) = \omega_0^2 Z_1 \cos(\omega t) + \epsilon Z_1^3 \cos^3(\omega t) \tag{3.11}$$

$$\approx \omega_0^2 Z_1 \cos(\omega t) \left(1 + \frac{3\epsilon Z_1^2}{4\omega_0^2}\right) \tag{3.12}$$

where $\cos^3(x) = \frac{1}{4}(3\cos(x) + \cos(3x))$ was used. According to (3.9) this already yields the perturbed frequency of the Duffing oscillator

$$\omega^2(Z_1) = \omega_0^2 \left(1 + \frac{3\epsilon Z_1^2}{4\omega_0^2}\right). \tag{3.13}$$

In summary, the method of harmonic balance is easy to apply and can be used to regard a wide range of perturbed oscillators. In the following the technique is used to calculate frequency shifts of a particle in a Penning trap.

3.2. Frequency Shifts in the Penning Trap due to Electrostatic Anharmonicities

As described before the electrostatic potential of the Penning trap is given by

$$V(z) = V_r \sum_k C_k z^k \tag{3.14}$$

and therefore the equation of motion for a particle in the Penning trap denotes

$$\ddot{z} + \frac{qV_r}{m} \sum_k k C_k z^{k-1} = 0. \tag{3.15}$$

As already mentioned before coefficients C_j with j odd will be ignored since they generate forces which average to zero around a complete orbit and therefore do not produce a frequency shift to first order [23].
In the following the frequency shifts due to electrostatic anharmonicities for the 4^{th}, 6^{th},

8^{th} and 10^{th} order of the expansion given in (3.14) are calculated.

Frequency Shifts up to 4th order

To obtain the frequency shifts up to 4th order the equation of motion

$$\ddot{z} + \frac{2qV_r}{m}C_2 z + \frac{4qV_r}{m}C_4 z^3 = 0 \tag{3.16}$$

has to be considered. Accordingly the result of the duffing equation can be used by substituting

$$\epsilon = \frac{4qV_r}{m}C_4. \tag{3.17}$$

This leads to the perturbed frequency

$$\omega^2(Z_1) = \omega_0^2 \left(1 + \frac{3qV_r C_4 Z_1^2}{m\omega_0^2}\right). \tag{3.18}$$

Since the perturbation is assumed to be small it is convenient to Taylor the expression in brackets to get rid of the squares according to $\sqrt{1+x} = 1 + \frac{x}{2}$ for $x \ll 1$. Thus

$$\omega(Z_1) = \omega_0 \left(1 + \frac{3qV_r C_4 Z_1^2}{2m\omega_0^2}\right). \tag{3.19}$$

The next step is to insert the unperturbed frequency $\omega_0^2 = \frac{2qV_r}{m}C_2$ again

$$\omega(Z_1) = \omega_0 \left(1 + \frac{3C_4 Z_1^2}{4C_2}\right). \tag{3.20}$$

Moreover its possible to replace the amplitude Z_1 of the particle by its energy using the classical relation for the energy $E_z = \frac{1}{2}m\omega_0^2 Z_1^2$. Rearranging this equation to

$$Z_1^2 = \frac{2E_z}{m\omega_0^2} = \frac{E_z}{qV_r C_2}, \tag{3.21}$$

where the unperturbed frequency ω_0 was used, gives

$$\omega(E_z) = \omega_0 \left(1 + \frac{3C_4}{4C_2^2}\frac{E_z}{qV_r}\right). \tag{3.22}$$

Calculating the frequency shift $\Delta\omega = \omega(E_z) - \omega_0$ finally results in the relative frequency shift of

$$\frac{\Delta\omega}{\omega_0} = \frac{3C_4}{4C_2^2}\frac{E_z}{qV_r}. \tag{3.23}$$

Frequency Shifts of Higher Orders

After the example for the 4^{th} order of anharmonicity now it is easy to proceed with higher orders, i.e. including C_6, C_8 and C_{10}. Instead of including all orders individually, the full calculation will be done first and afterwards the frequency shifts up to certain orders will be presented.
Taking the anharmonities up to the 10th order into account, the equation of motion reads

$$\ddot{z} + \frac{2qV_rC_2}{m}z + \frac{4qV_rC_4}{m}z^3 + \frac{6qV_rC_6}{m}z^5 + \frac{8qV_rC_8}{m}z^7 + \frac{10qV_rC_10}{m}z^9 = 0 \tag{3.24}$$

$$\ddot{z} + \omega_0^2 z + \alpha z^3 + \beta z^5 + \gamma z^7 + \delta z^9 = 0 \tag{3.25}$$

where $\omega_0^2, \alpha, \beta, \gamma and \delta$ were substituted for simplicity as follows

$$\omega_0^2 = \frac{2qV_rC_2}{m} \tag{3.26}$$

$$\alpha = \frac{4qV_rC_4}{m} \tag{3.27}$$

$$\beta = \frac{6qV_rC_6}{m} \tag{3.28}$$

$$\gamma = \frac{8qV_rC_8}{m} \tag{3.29}$$

$$\delta = \frac{10qV_rC_{10}}{m}. \tag{3.30}$$

Analogously to before the force is given by

$$f(t) = \omega_0^2 Z_1 \cos(\omega t) + \alpha Z_1^3 \cos^3(\omega t) + \beta Z_1^5 \cos^5(\omega t) + \gamma Z_1^7 \cos^7(\omega t) + \delta Z_1^9 \cos^9(\omega t). \tag{3.31}$$

Expressing the different powers of cosine by

$$\cos^n(x) = \frac{1}{2^n}\sum_{k=0}^{n}\binom{n}{k}\cos((n-2k)x), \text{ i.e.} \tag{3.32}$$

$$\cos^3(x) = \frac{1}{4}\left(3\cos(x)+\cos(3x)\right) \tag{3.33}$$

$$\cos^5(x) = \frac{1}{16}\left(10\cos(x)+5\cos(3x)+\cos(5x)\right) \tag{3.34}$$

$$\cos^7(x) = \frac{1}{128}\left(70\cos(x)+42\cos(3x)+14\cos(5x)+2\cos(7x)\right) \tag{3.35}$$

$$\cos^9(x) = \frac{1}{512}\left(252\cos(x)+168\cos(3x)+72\cos(5x)+18\cos(7x)+2\cos(9x)\right) \tag{3.36}$$

and neglecting higher harmonics of ω leads to

$$f(t) \approx \omega_0^2 Z_1 \cos(\omega t)\left(1+\frac{3\alpha Z_1^2}{4\omega_0^2}+\frac{5\beta Z_1^4}{8\omega_0^2}+\frac{35\gamma Z_1^6}{64\omega_0^2}+\frac{63\delta Z_1^8}{128\omega_0^2}\right). \tag{3.37}$$

Consequently the perturbed frequency can be determined to be

$$\omega^2(Z_1) = \omega_0^2\left(1+\frac{3\alpha Z_1^2}{4\omega_0^2}+\frac{5\beta Z_1^4}{8\omega_0^2}+\frac{35\gamma Z_1^6}{64\omega_0^2}+\frac{63\delta Z_1^8}{128\omega_0^2}\right) \tag{3.38}$$

$$\Rightarrow \omega(Z_1) = \omega_0\left(1+\frac{3\alpha Z_1^2}{8\omega_0^2}+\frac{5\beta Z_1^4}{16\omega_0^2}+\frac{35\gamma Z_1^6}{128\omega_0^2}+\frac{63\delta Z_1^8}{256\omega_0^2}\right) \tag{3.39}$$

$$= \omega_0\left(1+\frac{3C_4 Z_1^2}{4C_2}+\frac{15C_6 Z_1^4}{16C_2}+\frac{35C_8 Z_1^6}{32C_2}+\frac{315C_{10} Z_1^8}{256\omega_0^2}\right) \tag{3.40}$$

$$= \omega_0\left(1+\frac{3C_4}{4C_2^2}\left(\frac{E_z}{qV_r}\right)+\frac{15C_6}{16C_2^3}\left(\frac{E_z}{qV_r}\right)^2+\frac{35C_8}{32C_2^4}\left(\frac{E_z}{qV_r}\right)^3+\frac{315C_{10}}{256C_2^5}\left(\frac{E_z}{qV_r}\right)^4\right) \tag{3.41}$$

where the Taylor expansion already was done, $\omega_0, \alpha, \beta, \gamma$ and δ were inserted and the amplitude Z_1 of the particle was expressed in terms of the axial energy E_z. Finally the relative frequency shift can be calculated:

$$\frac{\Delta\omega}{\omega_0} = \left(\frac{3C_4}{4C_2^2}\left(\frac{E_z}{qV_r}\right)+\frac{15C_6}{16C_2^3}\left(\frac{E_z}{qV_r}\right)^2+\frac{35C_8}{32C_2^4}\left(\frac{E_z}{qV_r}\right)^3+\frac{315C_{10}}{256C_2^5}\left(\frac{E_z}{qV_r}\right)^4\right). \tag{3.42}$$

To summarise the results, the relative frequency shift for taking correction terms up to 4^{th}, 6^{th}, 8^{th} and 10^{th} order are listed:

Frequency shifts up to 4^{th} order:

$$\frac{\Delta\omega}{\omega_0} = \frac{3C_4}{4C_2^2}\left(\frac{E_z}{qV_r}\right) \tag{3.43}$$

Frequency shifts up to 6$^{\text{th}}$ order:

$$\frac{\Delta\omega}{\omega_0} = \left(\frac{3C_4}{4C_2^2}\left(\frac{E_z}{qV_r}\right) + \frac{15C_6}{16C_2^3}\left(\frac{E_z}{qV_r}\right)^2\right) \tag{3.44}$$

Frequency shifts up to 8$^{\text{th}}$ order:

$$\frac{\Delta\omega}{\omega_0} = \left(\frac{3C_4}{4C_2^2}\left(\frac{E_z}{qV_r}\right) + \frac{15C_6}{16C_2^3}\left(\frac{E_z}{qV_r}\right)^2 + \frac{35C_8}{32C_2^4}\left(\frac{E_z}{qV_r}\right)^3\right). \tag{3.45}$$

Frequency shifts up to 10$^{\text{th}}$ order:

$$\frac{\Delta\omega}{\omega_0} = \left(\frac{3C_4}{4C_2^2}\left(\frac{E_z}{qV_r}\right) + \frac{15C_6}{16C_2^3}\left(\frac{E_z}{qV_r}\right)^2 + \frac{35C_8}{32C_2^4}\left(\frac{E_z}{qV_r}\right)^3 + \frac{315C_{10}}{256C_2^5}\left(\frac{E_z}{qV_r}\right)^4\right). \tag{3.46}$$

In Figure 3.1 the frequency shifts for 4$^{\text{th}}$, 6$^{\text{th}}$, 8$^{\text{th}}$ and 10$^{\text{th}}$ orders of anharmonicity are shown in comparison where the tuning ratio TR was chosen such that C_4 vanishes.

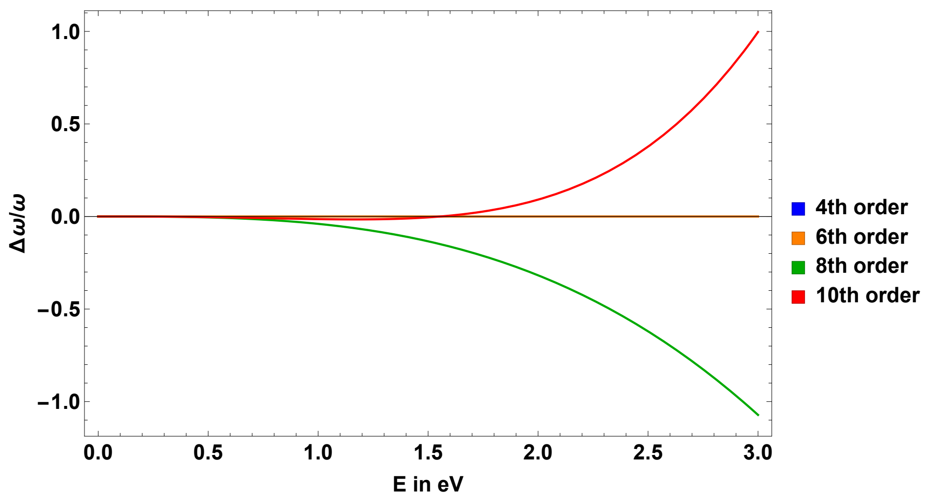

Figure 3.1: Frequency shifts for each order of anharmonicity discussed before with the tuning ratio TR chosen such that C_4 is compensated.

In Figure 3.2 the frequency shifts for each order are compared for tuning ratios TR such that C_4 and C_6 are compensated respectively.

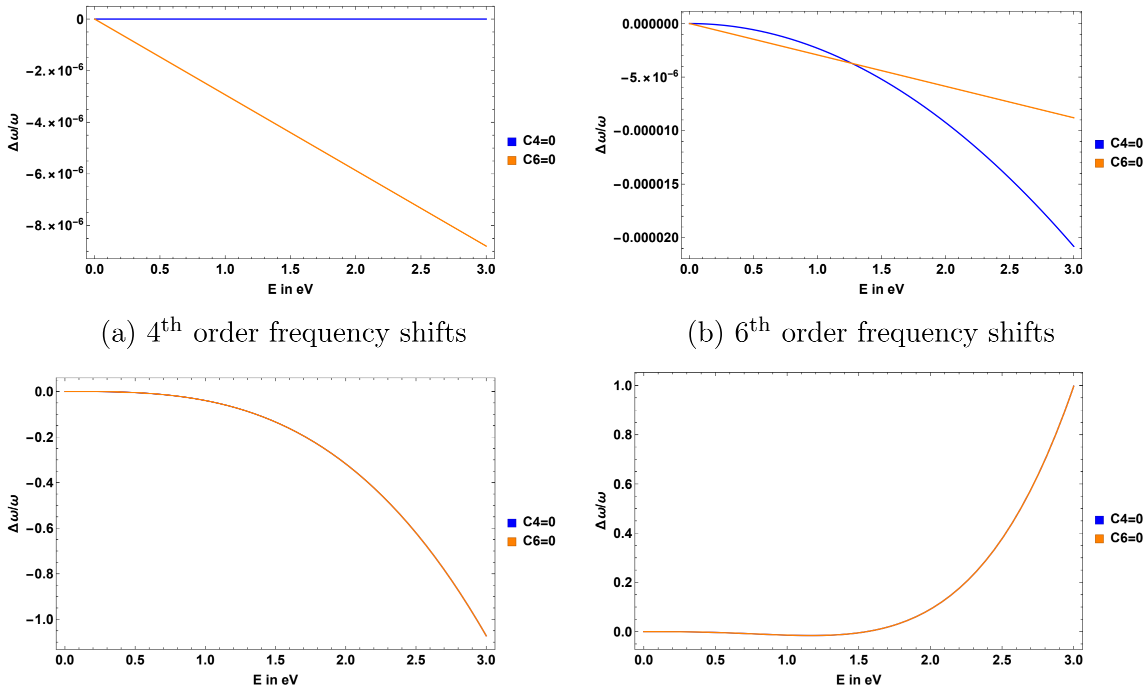

(a) 4^{th} order frequency shifts

(b) 6^{th} order frequency shifts

(c) 8^{th} order frequency shifts

(d) 10^{th} order frequency shifts

Figure 3.2: Frequency shifts for each order for tuning ratios TR such that C_4 and C_6 are compensated respectively.

Having a closer look at the frequency shift including up to the 10^{th} order reveals that the relative frequency shift $\frac{\Delta\omega}{\omega_0}$ is zero for the specific energy of $E_{z,0} = 1.5545\,\text{eV}$. After exciting the particle to this energy the axial frequency is not shifted. Unfortunately the energy $E_{z,0} = \frac{1}{2}m\omega_z^2 z_0^2$ corresponds to an axial amplitude of $z_0 = 4.29\,\text{mm}$ which is much larger than the length of the ring electrode l_r. Furthermore during cooling the particle undergoes a frequency shift of approximately 63 kHz. Thus it is not reasonable to excite the particle to the energy $E_{z,0}$.

In conclusion, the frequency shifts depend on the C_j coefficients of higher orders and the axial energy E_z. The C_j coefficients of higher orders introduce the anharmonicities due to electrostatical imperfections with respect to the ideal Penning trap. Therefore the more harmonic the electrostatic potential is the smaller the frequency shifts are. The aim of section 4 is to tune the coefficients C_j such the frequency shifts can be reduced. The dependency of the axial energy E_z becomes important if the particle is excited to perform peak measurements (see section 5). For the special case of phase sensitive methods this is discussed in section 7.

4. Potential Studies - Electrostatic Potential

In section 3 the impact of anharmonicities of the electrostatic potential and the resulting frequency shifts were discussed. This section deals with those anharmonicities and the attempt to minimise or even compensate them. As seen in subsection 2.2 the C_j coefficients depend on the explicit trap geometry and the voltages applied to the electrodes. Obviously it is much simpler to change the applied voltages instead of modifying the whole trap. Therefore the voltages applied to the electrodes are varied for the given trap geometry in the experiment.

Note: During this investigations machining imperfections are not considered.

4.1. Trap geometry in the BASE Experiment

Solving the Laplace equation (2.18) with Dirichlet boundary conditions results in the full solution of the electrostatic potential (2.2) which strongly depends on the trap geometry. Thus, before trying to tune the trap, first the trap geometry and basic properties of the trap have to be discussed. Usually the classical 5-pole Penning trap is considered to tune the trap. Unfortunately the possibilities are rather limited due to the number of available electrodes which can be tuned. To overcome this constraints in the following investigations also a more complex model of an extended electrode stack is considered.

4.1.1. 5-Pole Penning Trap

The 5-pole Penning trap was already shortly discussed in section 2 and is shown in Figure 2.4. The trap is a cylindrical stack of five electrodes with radius $a = 4.5\,\mathrm{mm}$. The main component is the ring electrode with length $l_r = 1.21\,\mathrm{mm}$ and the voltage applied to this electrode is denoted by V_r. Next to the ring electrode are two correction electrodes with length l_{ce} where the according voltage is denoted with V_{ce}. The two remaining electrodes are the so called endcaps which have the same length as the correction electrodes. However, in the following calculations the length of the endcaps is set to $\bar{l}_{ec} = 4\,\mathrm{mm}$ since the point of interest is the trap centre and the other electrodes in the trap stack (see subsubsection 4.1.2) are grounded too. The endcaps are usually set to ground, i.e. the applied voltage is $V_{ec} = 0$. The single electrodes are separated by saphir rings with rings with length $d = 140\,\mu$m. A schematic sketch of the 5-pole Penning trap is shown in Figure 4.1.

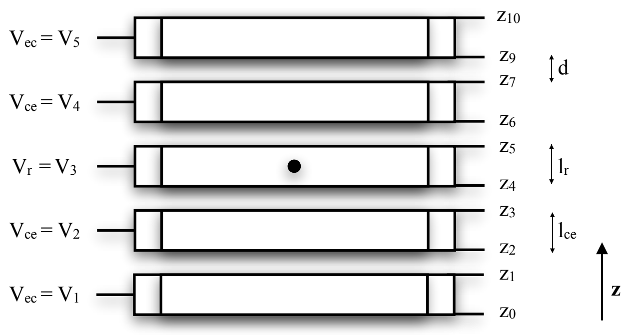

Figure 4.1: Schematic sketch of the 5-pole Penning trap.

To examine if the 5-pole Penning trap with the given trap geometry is 'compensated' it is necessary to check if C_4 and C_6 can be compensated for the same tuning ratio TR, i.e. the equations $C_4(TR) = 0$ and $C_6(TR) = 0$ have to be solved. Unfortunately the optimal tuning ratio for compensating C_4 is $TR_{opt,C_4} = 0.881019$ while the optimal tuning ratio for compensating C_6 is $TR_{opt,C_6} = 0.881015$. Thus the 5-pole Penning trap used in the BASE experiment is not perfectly 'compensated' since the optimal tuning ratios differ by the order of 10^{-6}. The relative coefficient strength is shown in Figure 4.2. Another attempt is to use an offset voltage between the two correction electrodes. Unfortunately also with this attempt it is not possible to compensate C_4 and C_6 at the same time. Those properties also hold for the extended electrode stack since only additional electrodes are considered there.

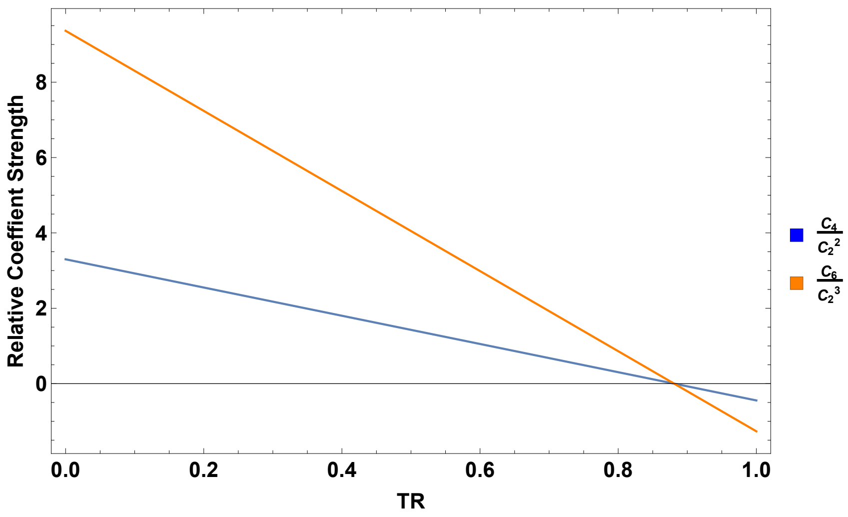

Figure 4.2: Relative coefficient strength for C_4 and C_6.

4.1.2. Extended Electrode Stack

The idea to use more electrodes out of the trap stack is the aim to compensate at least the coefficients C_4 and C_6 at the same time. In addition to the 5-pole Penning trap discussed in subsubsection 4.1.1 more electrodes are considered. A schematic sketch of the extended electrode stack is shown in Figure 4.3 next to the corresponding extract of the connection diagram of the current trap stack. The model was chosen in the way that electrode T4 coincides with electrode V_4 and consequently electrode T6 coincides with V_{17}. The electrodes V_1 to V_3 were added to the model to obtain a symmetric trap. This can be justified by assuming that the electrodes before are grounded anyway. The additional electrodes have the same dimensions as the correction and endcap electrodes.

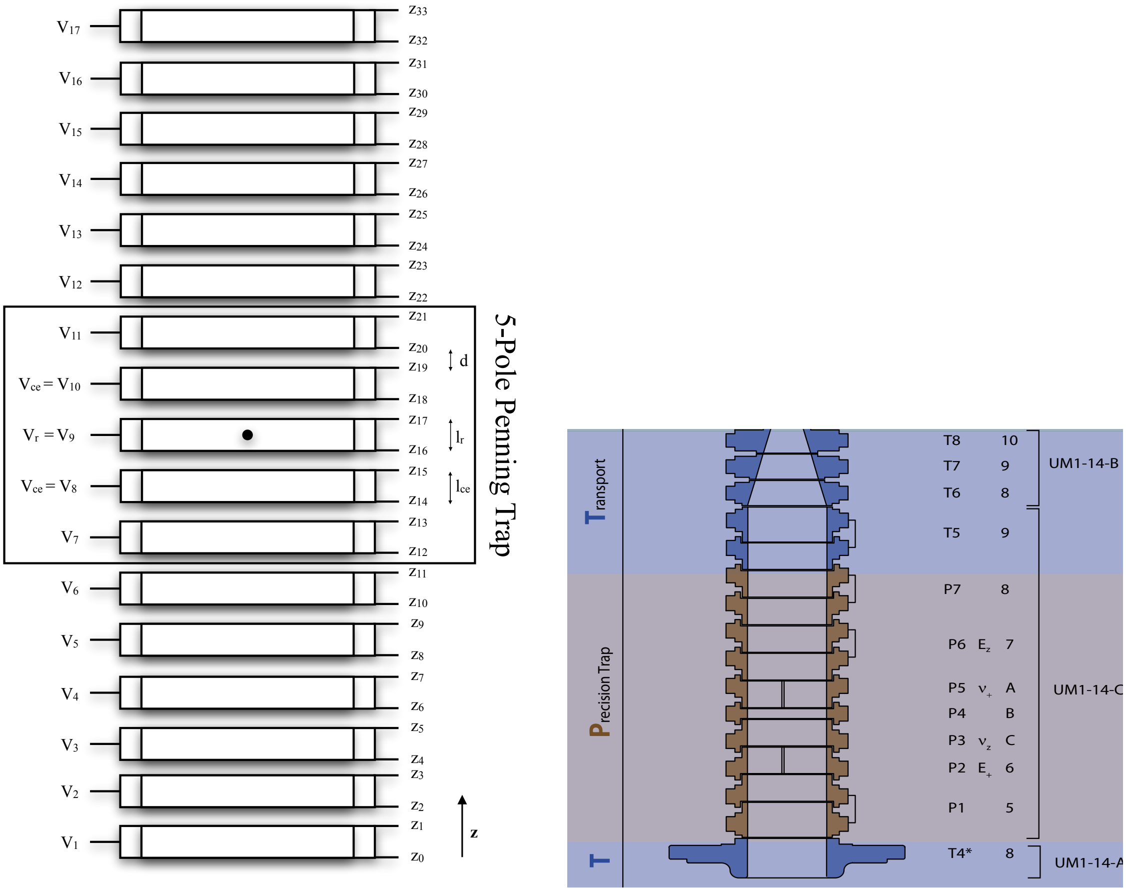

(a) Extended electrode stack

(b) Connection diagram

Figure 4.3: Schematic sketch of the extended electrode stack.

4.1.3. Convergence of coefficients C_j

In subsection 2.2 the expansion coefficients C_j (2.25) of the electrostatic potential in axial direction were derived. Using a computer algebra system the infinite sum is not realisable. Therefore the sum has to be approximated by stopping at an upper limit t. To determine which upper level t is sufficiently large, the convergence of the C_j coefficients with respect to t has to be examined. In the following the attempt is to find the optimal tuning ratio TR_{opt} where C_4 is examined. Thus it is reasonable to take this as a quantity to study the convergence of the coefficients C_j. The optimal tuning ratios TR_{opt} to compensate C_4 and C_6 respectively as a function of the upper limit t are shown in Figure 4.4.

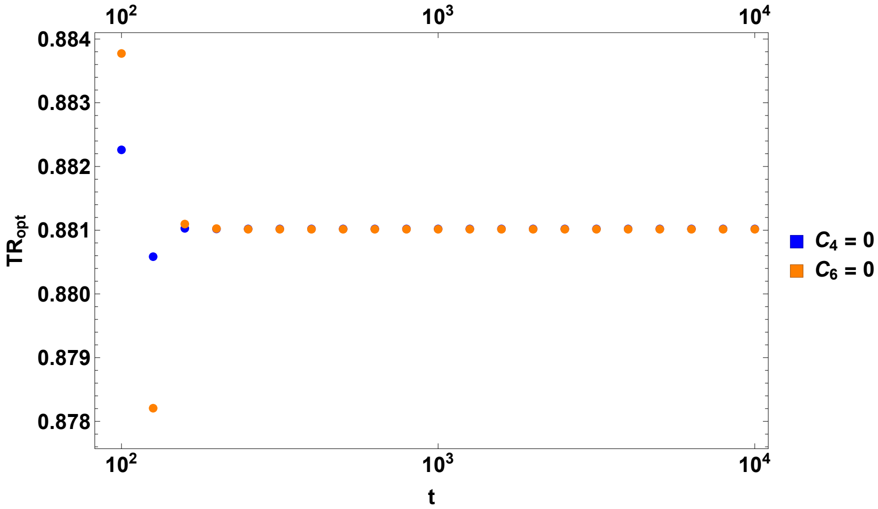

Figure 4.4: Convergence of the tuning ratio TR_{opt} such that C_4 and C_6 vanish respectively with respect to the upper limit of the sum t.

To quantify if the upper limit t is large enough it is convenient to compare those deviations with deviations resulting from machining imperfections of the trap. The machining imperfections for the radius a, the ring electrode length l_r and the correction electrode length l_{ce} are $5\,\mu$m while for the length of the saphir rings d it is $10\,\mu$m. The resulting dependencies on these machining imperfections are shown in Figure 4.5. Obviously those deviations are already larger than those due to the upper limit for approximately $t = 10^{2.3}$. In the following at least $t = 10^3$ is used to suppress the impact of deviations due to the convergence of the coefficients C_j.

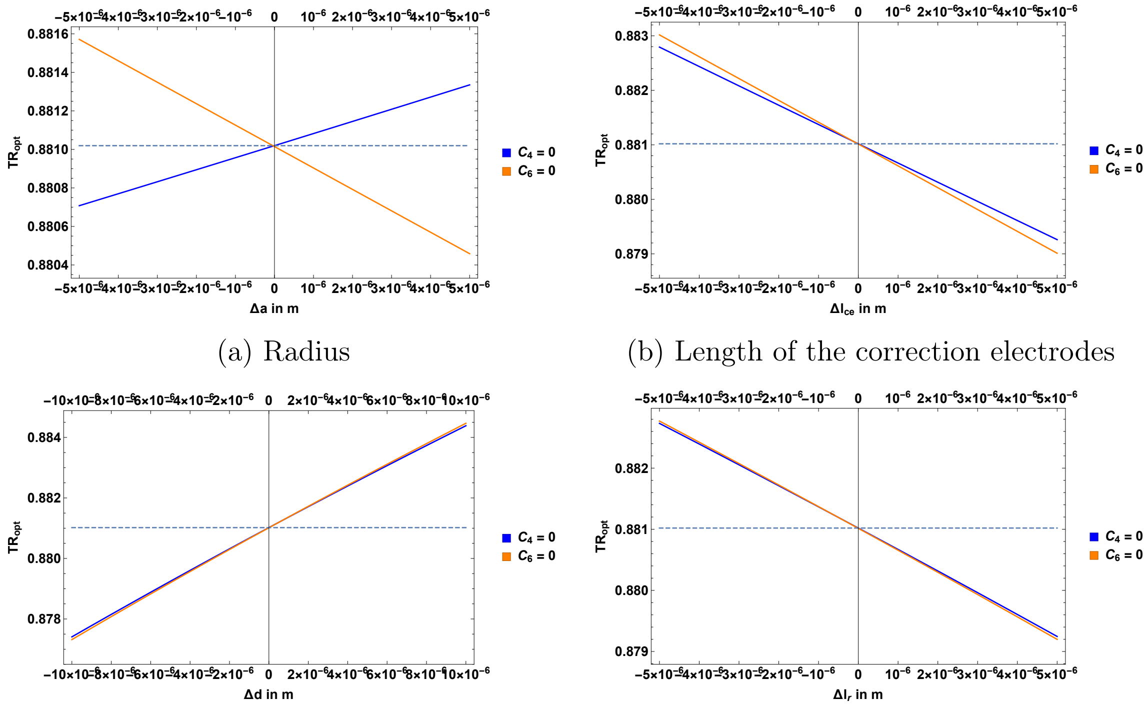

(a) Radius

(b) Length of the correction electrodes

(c) Length of the separation saphir rings

(d) Length of the ring electrode

Figure 4.5: Impact of machining imperfections on the tuning ratio TR_{opt} such that C_4 and C_6 respectively vanish.

4.2. Methods to Minimise Frequency Shifts

The Penning trap in the experiment is fixed as described in subsection 4.1. Furthermore the ring voltage V_r typically is also assumed to be fixed since in first order it defines the axial frequency $\omega_z = \sqrt{\frac{2qV_rC_2}{m}}$, together with the harmonic expansion coefficient C_2. The detection system described in section 5 usually is build such that it is most sensitive for a given range of the axial frequency. Hence, it is convenient to keep the axial frequency in this regime while tuning the electrostatical trap, i.e. around 640 kHz.

The basic idea of trap tuning with respect to the electrostatical potential is to apply voltages to the correction electrodes to tune the C_j coefficients and thus try to control the frequency shifts. For the 5-pole Penning trap this only includes the the correction electrodes next to the ring electrode since the endcaps are grounded. Considering the extended electrode stack, there is a variety of additional electrodes which can be used to tune the electrostatical potential. It is important to keep in mind that the main interest is the 'harmonicity' in the trap centre where the particle is trapped, which in the chosen coordinate system coinsides with the origin.

In the following a numerical and an analytical approach is presented to minimise frequency shifts. The main concept is to determine the tuning ratios TR_i applied to the correction electrodes with respect to the ring voltage to compensate as many coefficients as possible. Obviously for each coefficient which has to be tuned to zero an additional correction electrode has to be considered since at least as many parameters as equations are necessary to get a solution.
For both approaches first the 5-pole Penning trap is considered to characterise the routine and to determine the limits of this model. Afterwards the model and routines are modified for the extended electrode stack.

4.3. Numerical Approach

The first approach is to model the potential numerically since the analytical solution discussed in subsection 2.2 takes a lot of computation time. Hence it is not possible to scan quickly through several tuning ratios TR_i to find the most harmonic configuration. Therefore an array of the electrostatical potentials ϕ_i with a resolution of $\mathrm{d}z$ for every single electrode with a normalised voltage of 1 V is calculated using the analytical solution (2.2). Afterwards any potential ϕ can be obtained by superimposing the potentials ϕ_i of the single electrodes since the Laplace equation (2.18) is linear. The advantage is that the potentials ϕ_i only have to be calculated once while the superposition itself just takes a small amount of time. Finally the obtained potential ϕ can be fitted in the trap centre to determine the expansion coefficients C_j.

4.3.1. 5-Pole Penning Trap and Characterisation of the Fitting Routine

As described before the first step is to calculate the potentials ϕ_i for every single electrode using a normalised voltage 1 V which can be seen in Figure 4.6.

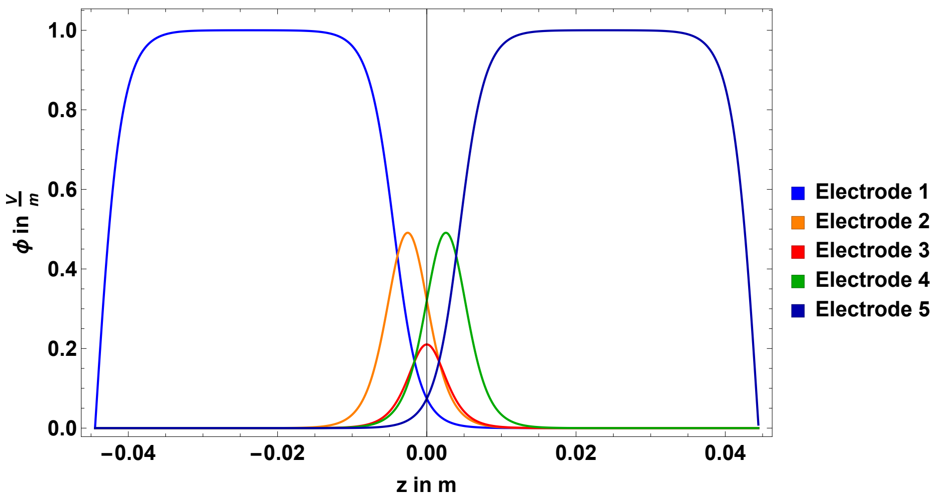

Figure 4.6: Electrostatic potentials for each single electrode.

Superimposing the potentials ϕ_i can be done by simply adding them up since the Laplace equation (2.18) is linear. An example for a superposition is shown in Figure 4.7 in comparison to the analytical solution.

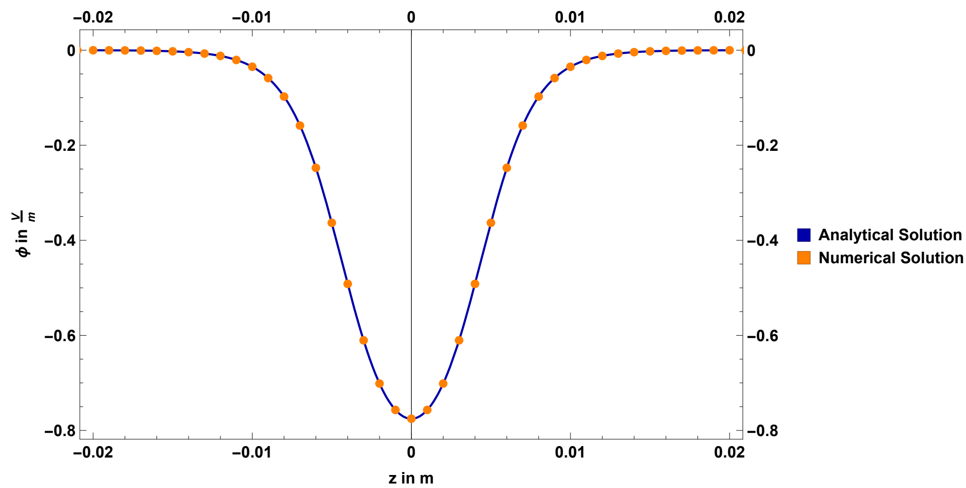

Figure 4.7: Superposition of electrostatic potentials compared to the analytical solution where less points were used to compare easier.

The next step is to characterise the fitting routine and parameters. In a first approach this can be done by determining the deviation of the fitted function of the analytical solution. An example is given in Figure 4.8 for the fit function

$$\phi(z) = C_0 + C_2 z^2 + C_4 z^4 + C_6 z^6 + C_8 z^8 + C_{10} z^{10} \tag{4.1}$$

where only even coefficients are used as discussed in subsection 3.2. The resulting deviations of the fitted potential in the trap centre (where a fitting width was chosen to be equal to the length of the ring electrode l_r) are on the order of 10^{-11} which is very small compared to the abolute value of the potential ϕ on the order of 1.

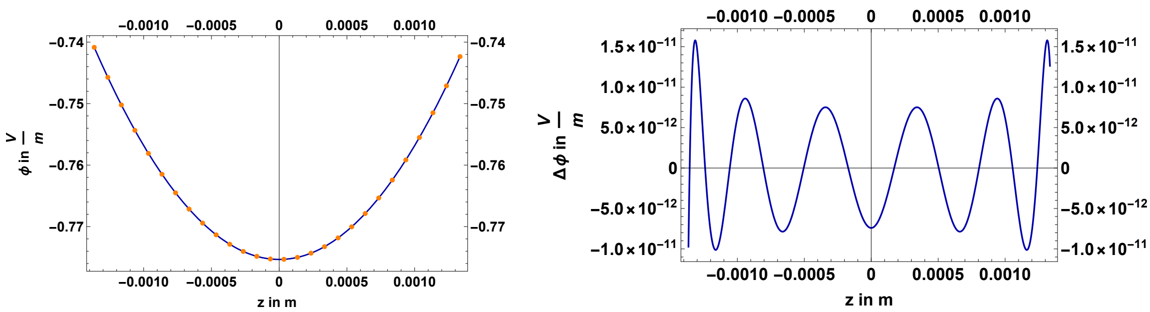

(a) fit and analytical solution (blue: analytical solution, orange: numerical simulation)

(b) Deviation of fit and analaytical solution

Figure 4.8: Comparison of the fit and the analytical solution in the trap centre.

A more complex and detailed test is to compare the optimal tuning ratio TR_{opt} where the first higher expansion coefficient C_4 is compensated, i.e. $C_4\big|_{TR_{opt}} = 0$. For this studies it is necessary to fit the potential ϕ for several tuning rations TR and to determine each C_4 coefficient. Then the set $\{(TR, C_4)\}$ can be fitted and the optimal tuning ratio TR_{opt} can be determined by calculating the root of the fitted function, i.e. the tuning ration TR where C_4 vanishes. Since the coefficient C_4 depends linearly on the tuning ratio TR the number of considered tuning ratios can be rather small. The deviation of this optimal tuning ratio TR_{opt} from the analytical one $TR_{opt,theo}$, which can be simply obtained by solving $C_4(TR) = 0$, can by examined with respect to several parameters. The most interesting parameters are the fitting order, i.e. to which coefficient C_j the potential is fitted, and the fitting width Δz centred at the potential minimum, since the point of interest is the trap centre but oscillations of the particle has to be taken into account. As shown in Figure 4.9 the best results are obtained for fits up to 10^{th} order and for fitting widths of the order of the length of the ring electrode.

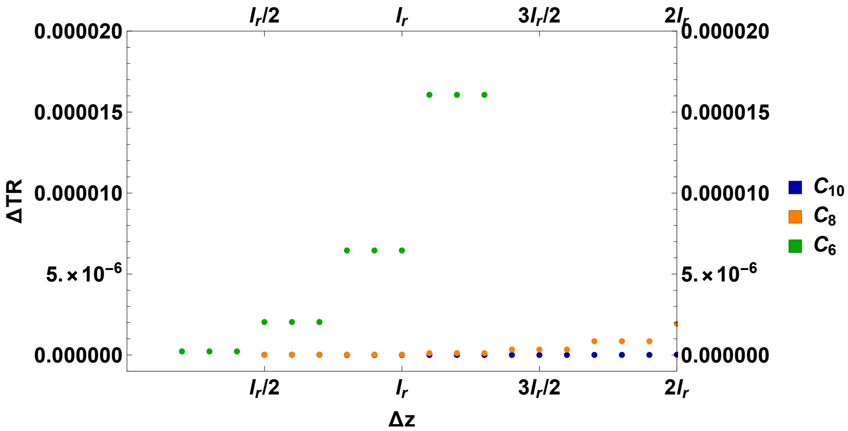

Figure 4.9: Deviation of the tuning ratio ΔTR as a function of the fit width Δz for different orders of the fit.

After characterising the fitting routine and parameters the procedure can be modified for the extended electrode stack. As mentioned before, the advantage of the extended electrode stack is that more than only one set of correction electrodes can be used to tune the trap potential.

4.3.2. Extended Electrode Stack

In principle the same routine as for the 5-pole Penning trap can be used for the extended electrode stack. Furthermore additional electrodes from the stack can be used. In the following this is shown for the example of considering electrode T4. The same routine as for the 5-pole Penning can be used to determine the optimal tuning ratio TR_{opt} such that the coefficient C_4 vanishes. Now this model is extended in the way that the optimal tuning ratio TR_{opt} for the correction electrodes next to the ring electrode, which are denoted by TR_1, is determined for different tuning ratios TR_2 applied to electrode T4. Consequently a set $\{(TT_2, TT_1)\}$ is obtained where TR_1 is a linear function of TR_2. Moreover, the same calculation can be done for tuning the coefficient C_6 to zero. Fitting the sets $\{(TT_2, TT_1)\}$ linearly for compensating C_4 or C_6 respectively, an intersection of the resulting linear fits can be calculated which can be represented by the tuple $(TT_{2,opt}, TT_{1,opt})$ where C_4 as well as C_6 are compensated. As a last step the results have to be cross-checked, since during the routine numerical errors of the routine itself and because of the machining precision of Mathematica itself can occur. Using the tuple $(TT_{2,opt}, TT_{1,opt})$ to calculate C_4 and C_6 the coefficients should be sufficiently small. But, they are not. In fact they are approximately of the order of 10^3. To understand this it is helpful to have a look at the general scaling of the coefficient C_4 as a function of the tuning ratio TR_1 which is shown in Figure 4.10. In Table 4.1 the impact of deviations from the analytical tuning ratio on the coefficient C_4 are shown.

$\Delta TR = \lvert TR - TR_{\text{alaytical}} \rvert$	C_4 in m^{-1}
10^{-2}	-1.28313×10^{7}
10^{-4}	-1.28313×10^{5}
10^{-6}	-1.28313×10^{3}
10^{-8}	-1.28313×10^{1}
10^{-10}	-1.28313×10^{-1}

Table 4.1: Impact of deviations of the tuning ratio TR from the analytical value $TR_{analytical} = 0.881019$ on the C_4 coefficient. For $TR_{analytical}$ the coefficient reads $C_4 = -1.23293 \times 10^{-7}\text{m}^{-1}$, where the fact that it is unequal zero is due to the machining precision of Mathematica.

Obviously the coefficient C_4 changes sensitively to deviations of the tuning ratio TR_1, even for adjustments on the order of less than 10^{-6}. Consequently it is not possible to determine the tuning ratios TR_i accurate enough to continue the studies. Therefore an analytical approach has to be considered.

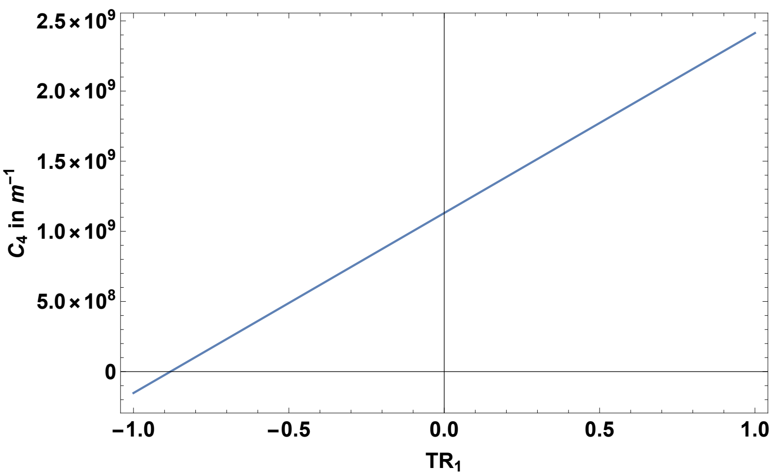

Figure 4.10: General scaling of the coefficient C_4 as a function of the tuning ratio TR.

4.4. Analytical Approach

In contrast to the numerical approach, in the case of the analytical approach the potential ϕ is not longer modelled to obtain the coefficients C_j. Consequently there is no fitting routine necessary. Furthermore all interesting properties of the 5-pole Penning trap were already discussed in subsubsection 4.1.1. Therefore only the extended electrode stack has to be considered.

Instead of modelling the potential ϕ, the basic idea is to deal with the coefficients C_j directly. To reduce the computation time the C_j coefficients are factorised in terms of the voltages V_i, which are applied to the electrodes, such that for a p-electrode Penning trap the coefficients read

$$C_j = \frac{1}{V_r} \sum_{i=1}^{p} f_{i,j} V_i \tag{4.2}$$

where $f_{i,j}$ are the factors in front of the voltages V_i. The factors $f_{i,j}$ are given by

$$\begin{aligned}
f_{1,j} =& \frac{2}{j!\Lambda} \sum_{n=1}^{\infty} \left[\frac{\cos(k_n z_0)}{k_n} - \frac{1}{k_n^2 d} \left(\sin(k_n z_2) - \sin(k_n z_1) \right) \right] \frac{(n\pi/\Lambda)^j}{I_0(k_n a)} \sin\left(\frac{\pi}{2}(n+j) \right) \\
f_{i,j} =& \frac{2}{j!\Lambda} \sum_{n=1}^{\infty} \frac{1}{k_n^2 d} \big[\sin(k_n z_{2i-2}) - \sin(k_n z_{2i-3}) - \sin(k_n z_{2i}) + \sin(k_n z_{2p-1}) \big] \\
& \times \frac{(n\pi/\Lambda)^j}{I_0(k_n a)} \sin\left(\frac{\pi}{2}(n+j) \right) \quad \text{for } 2 \leq i \leq p-1 \qquad (4.3) \\
f_{p,j} =& \frac{2}{j!\Lambda} \sum_{n=1}^{\infty} \left[-\frac{\cos(k_n \Lambda)}{k_n} + \frac{1}{k_n^2 d} \left(\sin(k_n z_{2p-2}) - \sin(k_n z_{2p-3}) \right) \right] \frac{(n\pi/\Lambda)^j}{I_0(k_n a)} \sin\left(\frac{\pi}{2}(n+j) \right).
\end{aligned}$$

The advantage of this factorisation is that now the sums only has to be evaluated once in the beginning and afterwards the coefficients C_j can by calculated by superimposing the factors weighted with the applied voltages, i.e. the idea is similar to the one in the numerical approach. Besides the improved computation time, now the expansion coefficients C_j written as in (4.2) are even simpler linear functions of the voltages V_i. Therefore calculating the optimal tuning ratios $TR_{i,opt}$ by solving $C_j(\{TR_i\}) = 0$ is just a set of linear equations which is easy to solve. The tuning ratios TR_i are always given in relation to the ring voltage V_r which in this chapter is set to $V_r = -1\,\mathrm{V}$.

In the following three different configurations of additional correction electrodes are considered.

Configuration 1

The first attempt is to consider the electrodes T4, which is described by V_4 in the extended electrode stack with tuning ratio TR_2, P7, which is described by $V_{13}\&V_{14}$ in the extended electrode stack with tuning ratio TR_3, and T5, which is described by $V_{15}\&V_{16}$ in the extended electrode stack with tuning ratio TR_4, since they are easily accessible and not many modifications have to be done with respect to the actual experimental setup.
First for each single correction electrode the optimal tuning ratios $TR_{1,opt}$ of the correction electrodes next to the ring electrode and the additional electrode $TR_{\{2,3,4\},opt}$ are determined to compensate C_4 and C_6 simultaneously. Basically there exists a solution if the curves $TR_{1,opt}(TR_{\{2,3,4\}})$ such that $C_4 = 0$ or $C_6 = 0$ respectively have an intersection which is shown in Figure 4.11. This can easily be done and the results are shown in Table 4.2.

	Electrode T4	Electrode P7	Electrode T5
$TR_{\{2,3,4\}}$	-8.21087×10^{-3}	-1.02123×10^{-3}	-5.11283×10^{-2}
TR_1	8.81016×10^{-1}	8.81016×10^{-1}	8.81016×10^{-1}
C_2 in m^{-1}	-1.85087×10^{4}	-1.85087×10^{4}	-1.85087×10^{4}
C_4 in m^{-1}	1.19209×10^{-7}	2.38419×10^{-7}	-2.51334×10^{5}
C_6 in m^{-1}	-3.90625×10^{-3}	-3.90625×10^{-3}	-2.33433×10^{9}
C_8 in m^{-1}	3.88216×10^{17}	3.88216×10^{17}	3.88206×10^{17}
$\frac{C_4}{C_2^2}$ in m	3.47983×10^{-16}	6.95965×10^{-16}	-7.32828×10^{-4}
$\frac{C_6}{C_2^3}$ in m^2	6.16072×10^{-16}	6.16072×10^{-16}	3.67524×10^{-4}
$\frac{C_8}{C_2^4}$ in m^3	3.30802	3.30802	3.30036

Table 4.2: Compensating the coefficients C_4 and C_6 at the same time using only one electrode. Displayed are the tuning ratios TR_i, coefficients C_j and the relative coefficient strength $\frac{C_j}{C_2^{j/2}}$.

Note that using the resulting tuning ratios the coefficients still not vanish. This is due to the machining precision of Mathematica, the sensitivity of the coefficients C_j on the tuning ratios and the upper limit t in the sum of the coefficients. Additionally to the value of the coefficients C_j also the relative coefficient strength $\frac{C_j}{C_2^{j/2}}$ are displayed which denotes the contribution of the coefficient to the frequency shift.

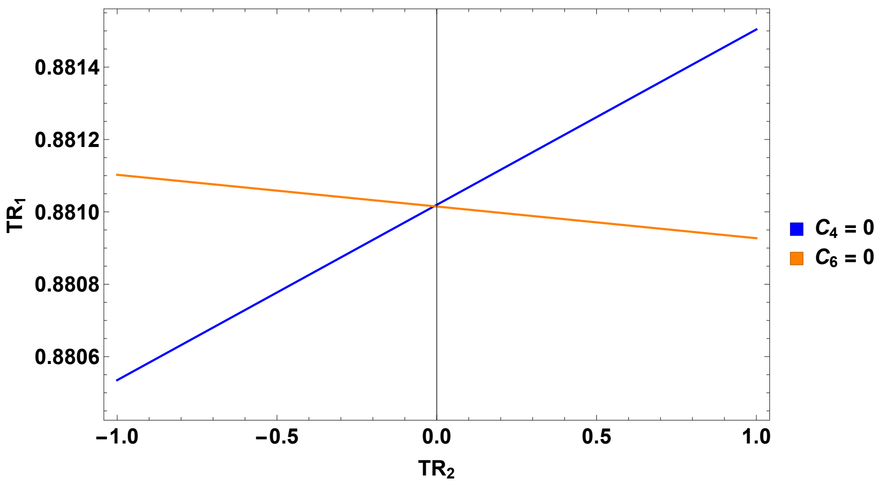

Figure 4.11: Tuning ratio TR_1 of the correction electrodes as a function of the tuning ratio TR_2 of electrode T4 such that C_4 and C_6 are compensated respectively.

The model can be extended to vary two of the three electrodes at the same time to tune the coefficient C_8 to zero additionally. Obviously it would also be possible to try to compensate C_4 and C_6 using two or three electrodes and to compensate C_4, C_6 and C_8 using three electrodes. But this would only lead to more experimental difficulties since every additional free parameter is a source of error and furthermore would require more high-precision voltage supplies. The procedure can be visualised by considering the three planes $TR_{1,opt}$ as a function of two of the three tuning ratios $TR_{2,3,4}$ for compensating C_4, C_6 and C_8 respectively. The solution for compensating all three coefficients is represented by the intersection of all three planes which is shown in Figure 4.13 for the third configuration since there exists a reasonable intersection.
Using two electrodes to compensate C_4, C_6 and C_8 the results for the optimal tuning rations are shown in Table 4.3.

	Electrode T4 & P7 ($i=1, j=2$)	Electrode T4 & T5 ($i=1, j=3$)	Electrode P7 & T5 ($i=2, j=3$)
TR_i	-4.55573×10^4	5.03411×10^5	-2.47966×10^3
TR_j	5.6662×10^3	-3.13469×10^6	1.2651×10^5
TR_1	9.54985×10^{-1}	9.54816×10^{-1}	1.02968
C_2 in m^{-1}	-9.57496×10^3	-9.60658×10^3	-1.28524×10^4
C_4 in m^{-1}	2.67029×10^{-5}	-1.2207×10^{-4}	1.81198×10^{-5}
C_6 in m^{-1}	1.875×10^{-1}	-1.5	1.46451×10^{13}
C_8 in m^{-1}	1.024×10^3	-2.048×10^3	7.38516×10^{16}
$\frac{C_4}{C_2^2}$ in m	2.91262×10^{-13}	-1.32273×10^{-12}	1.09695×10^{-13}
$\frac{C_6}{C_2^3}$ in m^2	-2.13595×10^{-13}	1.69194×10^{-12}	-6.89829
$\frac{C_8}{C_2^4}$ in m^3	1.2183×10^{-13}	-2.40466×10^{-13}	2.70661

Table 4.3: Compensating the coefficients C_4, C_6 and C_8 at the same time using two electrodes. Displayed are the tuning ratios TR_k, coefficients C_j and the relative coefficient strength $\frac{C_j}{C_2^{j/2}}$.

Unfortunately the resulting tuning ratios are not realisable since at least one of them exceeds the typical range of the current voltage supplies of $-10\,\mathrm{V}$ to $10\,\mathrm{V}$ and also would influence the potential in the regime of the particle oscillation significantly.

The used electrodes in this configuration are not symmetrically arranged around the ring electrode which also could lead to high tuning ratios since they have to compensate the additional coefficient C_8 and the anharmonicity introduces by using a non-symmetric configuration. Thus it might be worth it to vary all three electrodes at the same time despite the resulting difficulties mentioned before. Varying all three electrodes the system on linear equations is overdetermined, i.e. the solution is dependent on one of the tuning ratios. An example is given in Figure 4.12. The plot shows that even using all three electrodes no realisable tuning ratios can be achieved.

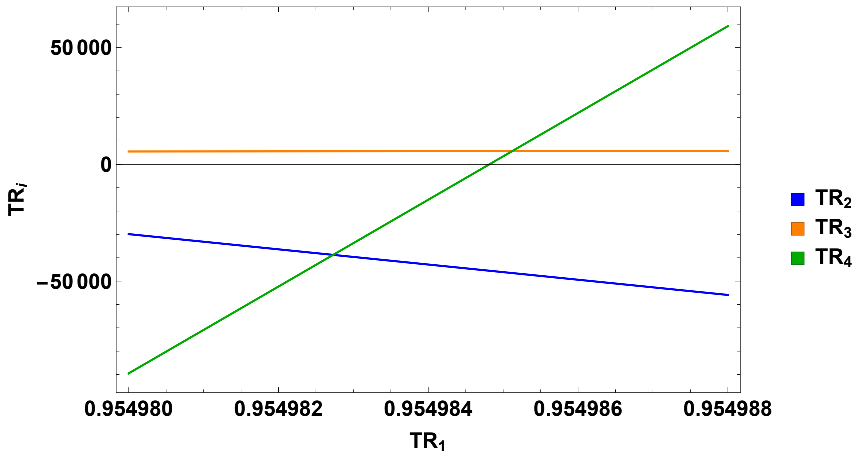

Figure 4.12: Tuning ratios TR_2, TR_3 and TR_4 as a function of the tuning ratio TR_1 such that C_4, C_6 and C_8 are compensated simultaneously.

The next two configurations are similar to each other. Both use a symmetric configuration around the ring electrode but with different distances from the centre. Furthermore the considered electrodes are closer to the ring electrode than in the first configuration. Unfortunately, to realise these configurations significant changes of the experimental setup have to be done. Besides, the closer the electrodes are to the trap centre the more precise the voltage supplies have to be, since the potential and thus the coefficients C_j act more sensitive on closer contributions.

Configuration 2

The second attempt considers the additional electrodes V_5, V_6, V_{12} and V_{13} where $V_5\&V_{13}$ and $V_6\&V_{12}$ are connected. The set of electrodes $V_5\&V_{13}$ is denoted as E_2, with the corresponding tuning ratio TR_2, where the set of electrodes $V_6\&V_{12}$ is denoted as E_3, with the corresponding tuning ratio TR_3. The procedure is the same as for the first configuration. Compensating C_4 and C_6 using only one additional set of electrodes leads to the results shown in Table 4.4.

	Electrode E_2	Electrode E_3
$TR_{\{2,3\}}$	-5.83143×10^{-4}	-9.31349×10^{-5}
TR_1	8.81016×10^{-1}	8.81015×10^{-1}
C_2 in m^{-1}	-1.85087×10^{4}	-1.85087×10^{4}
C_4 in m^{-1}	-1.43051×10^{-6}	1.19209×10^{-6}
C_6 in m^{-1}	-3.90625×10^{-3}	3.90625×10^{-3}
C_8 in m^{-1}	3.88216×10^{17}	3.88217×10^{17}
$\frac{C_4}{C_2^2}$ in m	-4.17579×10^{-15}	3.47982×10^{-15}
$\frac{C_6}{C_2^3}$ in m^2	6.16072×10^{-16}	-6.16069×10^{-16}
$\frac{C_8}{C_2^4}$ in m^3	3.30802	3.30801

Table 4.4: Compensating the coefficients C_4 and C_6 at the same time using one set of electrodes. Displayed are the tuning ratios TR_k, coefficients C_j and the relative coefficient strength $\frac{C_j}{C_2^{j/2}}$.

Considering both sets of additional electrodes to compensate C_4, C_6 and C_8 gives the tuning ratios shown in Table 4.5.

TR_2	-2.10877×10^{2}
TR_3	3.36795×10^{1}
TR_1	9.57212×10^{-1}
C_2 in m^{-1}	-9.15397×10^{3}
C_4 in m^{-1}	-5.96046×10^{-7}
C_6 in m^{-1}	1.5625×10^{-2}
C_8 in m^{-1}	-2.56×10^{2}
$\frac{C_4}{C_2^2}$ in m	-7.11314×10^{-15}
$\frac{C_6}{C_2^3}$ in m^2	-2.037×10^{-14}
$\frac{C_8}{C_2^4}$ in m^3	-3.64588×10^{-14}

Table 4.5: Compensating the coefficients C_4, C_6 and C_8 at the same time using both sets of electrodes. Displayed are the tuning ratios TR_i, coefficients C_j and the relative coefficient strength $\frac{C_j}{C_2^{j/2}}$.

Unfortunately also with this modified configuration no realisable tuning ratios can be achieve.

To reduce the necessary tuning ratios the idea is to use electrodes closer to the ring electrode.

Configuration 3

The third attempt considers the additional electrodes V_6, V_7, V_{11} and V_{12} where $V_6\&V_{12}$ and $V_7\&V_{11}$. The set of electrodes $V_6\&V_{12}$ is denoted as E_2, with the corresponding tuning ratio TR_2, where the set of electrodes $V_7\&V_{11}$ is denoted as E_3, with the corresponding tuning ratio TR_3. The procedure is the same as for the last configurations. Compensating C_4 and C_6 using only one additional set of electrodes leads to the results shown in Table 4.6.

	Electrode E_2	Electrode E_3
$TR_{\{2,3\}}$	7.85148×10^{-5}	-9.31349×10^{-5}
TR_1	8.81025×10^{-1}	8.81015×10^{-1}
C_2 in m^{-1}	-1.85073×10^{4}	-1.85087×10^{4}
C_4 in m^{-1}	0	1.19209×10^{-6}
C_6 in m^{-1}	0	3.90625×10^{-3}
C_8 in m^{-1}	3.88186×10^{17}	3.88217×10^{17}
$\frac{C_4}{C_2^2}$ in m	0	3.47982×10^{-15}
$\frac{C_6}{C_2^3}$ in m^2	0	-6.16069×10^{-16}
$\frac{C_8}{C_2^4}$ in m^3	3.30879	3.30801

Table 4.6: Compensating the coefficients C_4 and C_6 at the same time using one set of electrodes. Displayed are the tuning ratios TR_k, coefficients C_j and the relative coefficient strength $\frac{C_j}{C_2^{j/2}}$.

Considering both sets of additional electrodes to compensate C_4, C_6 and C_8 gives the tuning ratios shown in Table 4.7.

TR_2	1.17953
TR_3	0.994446
TR_1	0.999762
C_2 in m^{-1}	-5.08661×10^{1}
C_4 in m^{-1}	5.96046×10^{-6}
C_6 in m^{-1}	1.17188×10^{-2}
C_8 in m^{-1}	0
$\frac{C_4}{C_2^2}$ in m	2.30369×10^{-9}
$\frac{C_6}{C_2^3}$ in m^2	-8.90424×10^{-8}
$\frac{C_8}{C_2^4}$ in m^3	0

Table 4.7: Compensating the coefficients C_4, C_6 and C_8 at the same time using both sets of electrodes. Displayed are the tuning ratios TR_i, coefficients C_j and the relative coefficient strength $\frac{C_j}{C_2^{j/2}}$.

The intersection of the planes of TR_1 as a function of TR_2 and TR_3 representing the coefficients C_4, C_6 and C_8 is shown in Figure 4.13.

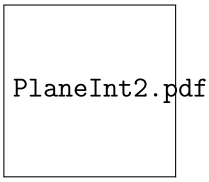

Figure 4.13: Tuning ratio TR_1 of the correction electrodes as a function of the tuning ratio TR_2 and TR_3 of electrode sets E_1 and E_2 such that C_4, C_6 and C_8 are compensated respectively for the third configuration.

Thus, for this configuration C_4, C_6 and C_8 can be compensates using realisable tuning ratios. However, the applied tuning ratios lead to a different C_2 coefficient. Hence the axial frequency changes to $\omega_z = \sqrt{\frac{2qV_rC_2}{m}} = 33\,328.2\,\mathrm{Hz}$ for a typical ring voltage of $V_r = -4.5\,\mathrm{V}$. This is a significant change in the axial frequency ω_z. Consequently the detection system would have to be modified if this configuration would be realised.

Conclusion:

In conclusion, it is possible to compensate C_4 and C_6 at the same time with one additional electrode, even using rather easily accessible electrodes as T4, P7 and T5. Unfortunately to compensate C_8 additionally a different trap configuration has to be considered and the detection has to be adjusted due to the change in the axial frequency.

5. Detection Principles

Among the confinement in the Penning trap an accurate detection system is essential to measure the free cyclotron frequency with high precision. The free cyclotron frequency is measured by measuring the three eigenmodes $\omega_\pm$ and ω_z of the Penning trap, which are related to the free cyclotron frequency via the invariance theorem (2.17). Furthermore the Larmor frequency ω_L has to be measured.

First, in subsection 5.1 the axial detection systems is discussed. Then, in subsection 5.2 the sideband technique is presented where the radial frequencies are measured by coupling them to the axial motion. Finally, in subsection 5.3 a discussion of the detection of the Larmor frequency is given.

5.1. Axial Detection System

In the following the detection principle to measure the axial frequency ω_z is discussed since the other relevant frequencies are measured indirectly by measuring the axial frequency. The modified cyclotron frequency ω_+ and the magnetron frequency ω_- are measured by sideband coupling to the axial motion and the Larmor frequency ω_L is obtained by measuring frequency shifts of the axial frequency ω_z. This is discussed in detail in subsection 5.2 for the the modified cyclotron frequency ω_+ and the magnetron frequency ω_- and in subsection 5.3 for the Larmor frequency ω_L.

In this section the detection principle is sketched while a detailed discussion can be found in [20, 22, 26, 27].

5.1.1. Image Current Detection

The motion of the particle with charge q induces a tiny image current I_p in the trap electrodes

$$I_p = \frac{q}{D_z}\dot{z} = \frac{q}{D_z}\omega_z z \tag{5.1}$$

where $v = \omega r$ was used and D_z is the effective electrode distance which depends on the trap geometry and describes the coupling strength of the particle to the detection system (for a detailed discussion see [22]). The image current, which usually is of the order of fA, can be converted to a detectable voltage U_p by connecting an inductor L to the trap electrodes.

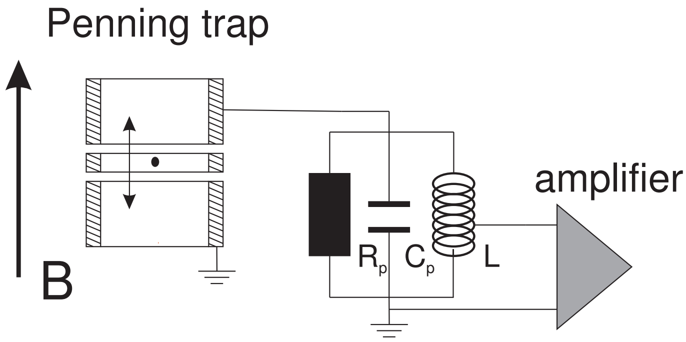

Figure 5.1: Schematic of the detector [22].

As shown in Figure 5.1 the inductor L together with its own parasitic capacity C_p, parasitic resistance R_p and capacity of the trap electrodes C_T forms a parallel resonance circuit. The induced image voltage is given by

$$U_p = Z_d I_p \tag{5.2}$$

where Z_d denotes the impedance of the resonator of the detection system and reads

$$\begin{aligned}
\frac{1}{Z_d} &= \frac{1}{R_p} + \frac{1}{i\omega L} + i\omega C_p + i\omega C_T \\
\Leftrightarrow Z_d &= \left(\frac{1}{R_p} + \frac{1}{i\omega L} + i\omega C\right)^{-1} \quad \text{with} \;\; C = C_p + C_T \\
\Leftrightarrow Z_d &= \left(\frac{1}{R_p} + i\left(\omega C - \frac{1}{\omega L}\right)\right)^{-1} \\
\Leftrightarrow Z_d &= \left(\frac{1}{R_p} + i\left(\frac{\omega}{\omega_0^2 L} - \frac{1}{\omega L}\right)\right)^{-1} \\
\Leftrightarrow Z_d &= \left(\frac{1}{R_p} + i\frac{\omega^2 - \omega_0^2}{\omega_0^2 \omega L}\right)^{-1} \\
\Leftrightarrow Z_d &= \frac{\frac{1}{R_p} - i\frac{\omega^2-\omega_0^2}{\omega_0^2\omega L}}{\frac{1}{R_p^2} + \left(\frac{\omega^2-\omega_0^2}{\omega_0^2\omega L}\right)^2}
\end{aligned} \tag{5.3}$$

where the resonance frequency of the resonator

$$\begin{aligned}\omega_0^2 &= \frac{1}{LC}\\ &= \frac{1}{L(C_p + C_T)}\end{aligned} \tag{5.4}$$

was introduced. It can be easily seen that on resonance, i.e. $\omega = \omega_0$, the parallel tuned circuit acts as a simple parallel resistance. Furthermore the particle interacts with the detection system and thus loses energy due to the real part of the impedance

$$\begin{aligned}\mathrm{Re}(Z_d) &= \frac{\frac{1}{R_p}}{\frac{1}{R_p^2} + \left(\frac{\omega^2-\omega_0^2}{\omega_0^2\omega L}\right)^2}\\ &= \frac{R_p\left(\omega_0^2\omega L\right)^2}{\left(\omega_0^2\omega L\right)^2 + R_p^2\left(\omega^2 - \omega_0^2\right)^2}.\end{aligned} \tag{5.5}$$

In experimentally more accessible quantities the real part of the detection system can be expressed as

$$\mathrm{Re}(Z_d) = R_p(\omega) = \omega_0 L Q \tag{5.6}$$

where Q is the quality factor or Q-value of the detection system and for a parallel tuned circuit is given by $Q = R\sqrt{\frac{C}{L}}$ which together with the definition of the resonance frequency ω_0 results in the expression above. Formally the quality factor Q is defined as the ratio of stored energy to energy loss per cycle. Expressed in experimentally more accessible quantities the quality factor is defined by

$$Q = \frac{\omega_0}{\Delta\omega} \tag{5.7}$$

where $\Delta\omega$ is the width of the transfer function at half maximum (FWHM). It is important to state that the resistance $R_p = R_p(\omega)$ is frequency dependent. Expressing the real part of the impedance of the detection system in terms of the quality factor Q as mentioned before it reads

$$\mathrm{Re}(Z_d) = R_p\frac{\left(\omega_0\omega\right)^2}{\left(\omega_0\omega\right)^2 + Q^2\left(\omega^2 - \omega_0^2\right)^2}. \tag{5.8}$$

Unfortunately in the experiment the parasitic capacity C_p and resistance R_p as well as the capacity of the trap electrodes C_T are not known. Therefore it is necessary to measure the effective parallel resistance R_p by measuring ω_0 and Q because the inductivity L is the only known quantity. Moreover, on resonance a voltage drop $U_p = R_p I_p = \omega_0 L Q I_p$ can be detected. Since the signal strength scales proportional to R_p it is important that it is as large as possible. Afterwards the measured signal of the detection system gets amplified and then analysed using a Fourier transformation.

5.1.2. Particle - Detector Interaction

While an excited particle dissipates in the detection system and can be measured as a peak [28], in thermal equilibrium with the detection system the particle causes a short at its axial frequency [22, 29]. This is the subject examined in this section.

In the last section it was shown that the motion of the particle generates a tiny image current. However, the particle interacts with its own image current and therefore loses energy due to the real part of the impedance of the detection system $\mathrm{Re}(Z_d) = R_p(\omega)$. This leads to an additional force

$$F_{ind} = \frac{q}{D_z} U_p. \tag{5.9}$$

Thus the equation of motion of the particle modifies from a harmonic oscillator to

$$\begin{aligned} & \ddot{z} + \omega_z^2 z + \frac{F_{ind}}{m} = 0 \\ \Leftrightarrow \quad & \ddot{z} + \frac{q^2}{D_z^2 m} R_p \dot{z} + \omega_z^2 z = 0 \end{aligned} \tag{5.10}$$

where in the second step (5.1),(5.2), (5.6) and (5.9) were used. This equation of motion describes a damped harmonic oscillator with damping or cooling constant

$$\gamma_z = \frac{q^2}{D_z^2 m} R_p \tag{5.11}$$

which leads to a Lorentz like line shape with width $\Delta\omega_z = \gamma_z$. Now (5.10) can be expressed in terms of the induced image current I_p instead of the particle position z:

$$\begin{aligned} & \frac{mD_z^2}{q^2}\dot{I}_p + \frac{mD_z^2}{q^2}\omega_z^2 \int I_p \mathrm{d}t + R_p I_p = 0 \\ \Leftrightarrow \quad & l_p \dot{I}_p + \frac{1}{c_p}\int I_p \mathrm{d}t + R_p I_p = 0 \quad \text{with} \qquad (5.12) \\ & l_p = \frac{mD_z^2}{q^2} \quad \text{and} \quad c_p = \frac{q^2}{mD_z^2\omega_z^2} \qquad (5.13) \end{aligned}$$

Consequently the particle can be described as a series tuned circuit with impedance

$$\begin{aligned} & Z_p = i\omega l_p + \frac{1}{i\omega c_p} \\ \Leftrightarrow\ & Z_p = i\left(\omega l_p - \frac{1}{\omega c_p}\right) \\ \Leftrightarrow\ & Z_p = i\left(\omega l_p - \frac{\omega_z^2 l_p}{\omega}\right) \\ \Leftrightarrow\ & Z_p = i\frac{l_p}{\omega}\left(\omega^2 - \omega_z^2\right) \qquad (5.14) \end{aligned}$$

where the axial resonance frequency of the particle

$$\omega_z^2 = \frac{1}{l_p c_p} \qquad (5.15)$$

was used. The total impedance can be calculated by connecting the series tuned circuit of the particle in parallel to the parallel tuned circuit of the detection system:

$$\begin{aligned} & \frac{1}{Z_{tot}} = \frac{1}{Z_d} + \frac{1}{Z_p} \\ \Leftrightarrow\ & Z_{tot} = \left(\frac{1}{Z_d} + \frac{1}{Z_p}\right)^{-1} \\ \Leftrightarrow\ & Z_{tot} = \left[\frac{1}{R_p} + i\left(\frac{\omega^2-\omega_0^2}{\omega_0^2\omega L} - \frac{\omega}{l_p}\frac{1}{\omega^2-\omega_z^2}\right)\right]^{-1} \\ \Leftrightarrow\ & Z_{tot} = \frac{\frac{1}{R_p} - i\left(\frac{\omega^2-\omega_0^2}{\omega_0^2\omega L} - \frac{\omega}{l_p}\frac{1}{\omega^2-\omega_z^2}\right)}{\frac{1}{R_p^2} + \left(\frac{\omega^2-\omega_0^2}{\omega_0^2\omega L} - \frac{\omega}{l_p}\frac{1}{\omega^2-\omega_z^2}\right)^2}. \qquad (5.16) \end{aligned}$$

To describe the expected signal in the frequency domain the real part of Z_{total} has to be considered

$$\begin{aligned}\chi(\omega) &= \mathrm{Re}(Z_{tot}) \\ &= \frac{R_p}{1 + R_p^2\left(\frac{\omega^2-\omega_0^2}{\omega_0^2\omega L} - \frac{\omega}{l_p}\frac{1}{\omega^2-\omega_z^2}\right)^2} \\ &= R_p \frac{\left(\omega^2-\omega_z^2\right)^2}{\left(\omega^2-\omega_z^2\right)^2 + \left(\frac{R_p}{\omega_0^2\omega L}\left(\omega^2-\omega_0^2\right)^2 - R_p\frac{\omega}{l_p}\right)^2}.\end{aligned} \tag{5.17}$$

This expression can be simplified according to

$$\frac{R_p}{\omega_0^2\omega L} = \frac{1}{\omega\Delta\omega_0} \tag{5.18}$$

where (5.4), (5.6) and (5.7) were used and

$$\frac{R_p}{l_p} = \Delta\omega_z \tag{5.19}$$

where (5.11), (5.13) and (5.15) were used. The resulting line shape after changing the sign in the last term of the denominator reads

$$\chi(\omega) = R_p \frac{\left(\omega^2-\omega_z^2\right)^2}{\left(\omega^2-\omega_z^2\right)^2 + \left(\frac{1}{\omega\Delta\omega_0}\left(\omega_0^2-\omega^2\right) + \omega\Delta\omega_z\right)^2}. \tag{5.20}$$

Typical line shapes for small and large detuning of the axial frequency with respect to the resonator resonance frequency are shown in Figure 5.2.

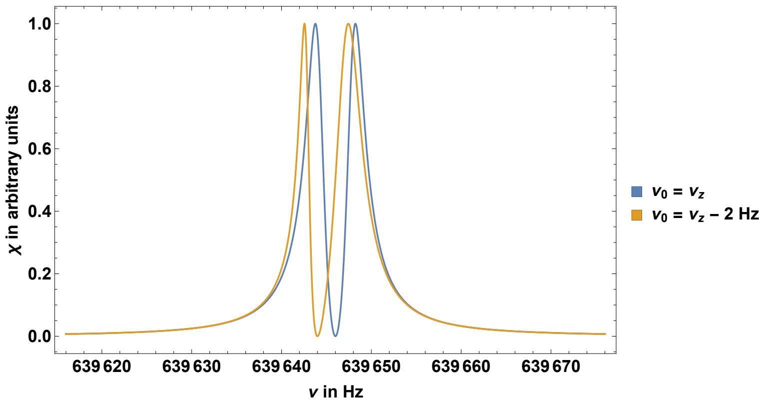

(a) $\chi(\nu)$ for ν_0 close to ν_z

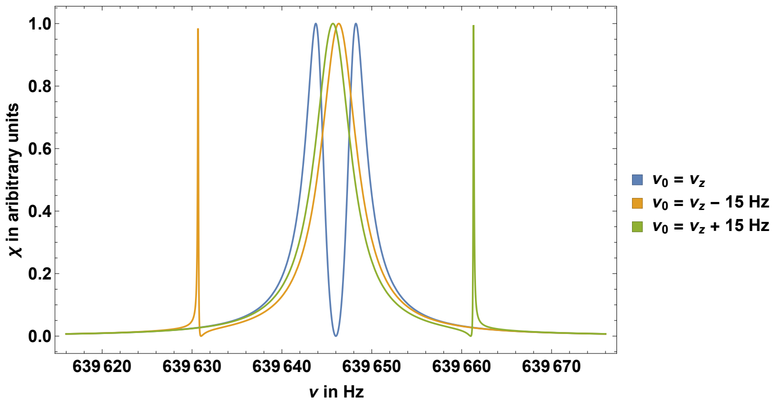

(b) $\chi(\nu)$ for ν_0 far detuned from ν_z

Figure 5.2: Typical line shapes for small and large detuning of the axial frequency with respect to the resonator resonance frequency. ($\nu_z = 639\,646\,\mathrm{Hz}$)

Note that the line shape in (5.20) sometimes is also denotes as the effective resistance $R_{eff} = \chi(\omega)$.
From this result it can be easily seen that

- if the particle is on resonance, i.e. $\omega = \omega_z$, $\chi(\omega)$ vanishes and therefore the particle represented by a series tuned circuit acts as a perfect short to the detector which can be observed as a dip in the resonator spectrum.

- if the system is operated at the resonance frequency of the detection system, i.e.

$\omega = \omega_0$, the effective resistance reads

$$R_{eff}\Big|_{\omega=\omega_0} = R_p \frac{\left(\omega^2 - \omega_z^2\right)^2}{\left(\omega^2 - \omega_z^2\right)^2 + \left(\omega\Delta\omega_z\right)^2} \tag{5.21}$$

with the FWHM of $\Delta\omega_z = \gamma_z = \frac{q^2}{D_z^2 m} R_p$.

- if the frequency is far detuned from ω_z then $\chi(\omega)$ is given by R_p.

The fact that the particle shorts the detector at its resonance frequency is used to measure the axial frequency ω_z in thermal equilibrium with the detection system at temperatures of a few Kelvins. This minimizes frequency shifts which increase with higher energy and therefore higher temperature. To understand the whole measuring principle thermal noise has to be taken into account.

5.1.3. Noise Spectrum

The noise of a resistor R at a certain temperature T with bandwidth $\Delta\nu$ is given by the Johnson-Nyquist-noise [30, 31]

$$u_n = \sqrt{4k_B T R \Delta\nu} \;\; \text{in units} \;\; \left[\frac{V}{\sqrt{Hz}}\right] \tag{5.22}$$

where k_B is the Boltzmann constant. However, it is convenient to consider the Jonson-Nyquist-noise per unit bandwidth

$$u_n = \sqrt{4k_B T R} \;\; \text{in units} \;\; \left[\frac{V}{Hz}\right]. \tag{5.23}$$

To obtain precise measurements a large signal compared to the noise background is required. Additionally there are several other noise sources. The noise sources are denoted by e_n. Finally the signal to noise ratio SNR reads

$$SNR = \sqrt{\frac{u_n^2 + \sum_n e_n^2}{\sum_n e_n^2}}. \tag{5.24}$$

Since $u_n \gg e_n$ the noise sources e_n often are neglected in the numerator.

5.1.4. Effective System

In the previous sections the combined system of particle and detector were discussed which led to an effective resistance R_{eff}. Additionally in this section the coupling to the amplifier is considered. If the amplifier would be directly coupled to the resonator the input resistance R_{in} of the amplifier would limit the Q factor [22]. Therefore the model in Figure 5.3 is introduced.

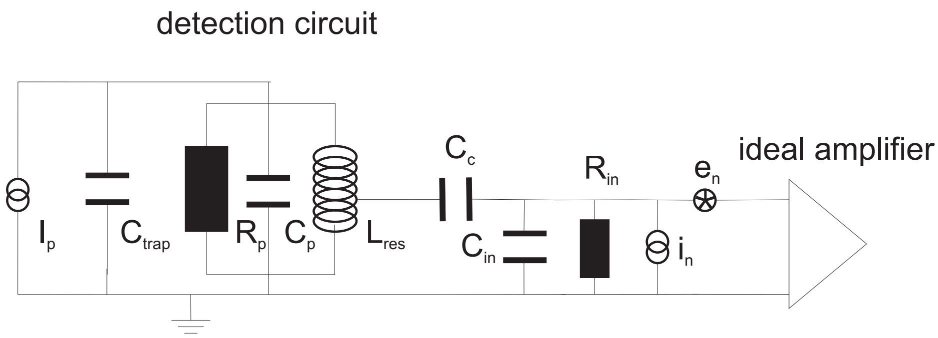

Figure 5.3: Schematic of the particle detection system [22].

The particle is modelled as a current source I_p in parallel to the resonator discussed before. The amplifier is coupled to the resonator by a coupling capacity C_c and its input is represented by parallel RC circuit with capacity C_{in} and resistance R_{in}. The noise components introduced by the amplifier are described by the current source i_n and the voltage source e_n. The amplifier is coupled to the resonator inductively and capacitively. The inductive coupling is realised by using a tap on the coil of the resonator resulting in an inductive coupling factor of

$$\kappa_l = \frac{N_1}{N_1 + N_2} \tag{5.25}$$

where N_1 and N_2 are the windings above and below the tap. The capacitive coupling is implemented by a capacitive coupling factor

$$\kappa_c = \frac{C_c}{C_c + C_{in}}. \tag{5.26}$$

Consequently the total coupling factor is given by

$$\kappa = \kappa_l \kappa_c. \tag{5.27}$$

Due to the coupling of the amplifier to the resonator the effective resistance of the whole detection system has to be modified

$$R_{sys} = \left(\frac{1}{R_{eff}} + \frac{\kappa^2}{R_{in}}\right)^{-1} = \frac{R_{eff}R_{in}/\kappa^2}{R_{eff} + R_{in}/\kappa^2}. \tag{5.28}$$

Unfortunately the effective resistance of the whole detection system R_{sys} can not be calculated and has to be measured. This can be easily done by fitting the frequency dependent transfer function $R_{sys}(\omega)$ to get the resonance frequency ω_0. Furthermore the Q-factor has to be measured. Finally R_{sys} is given by

$$R_{sys} = \omega_0 LQ \tag{5.29}$$

where L still is the inductivity of the inductor introduced in subsubsection 5.1.1. Finally the gain due to the amplifier has to be considered. Since the gain factor has to be measured anyway it is usually absorbed into R_{sys}. In the following always the full resistance has to be considered.

5.1.5. Signal to Noise Ratio SNR

To evaluate the signal to noise ratio SNR in the experiment it is important to distinguish between a dip and peak detection.

Peak Detection

Using the peak detection method the resulting signal of the particle is measured against the noise of the system. A typical peak spectrum is shown in Figure 5.4.

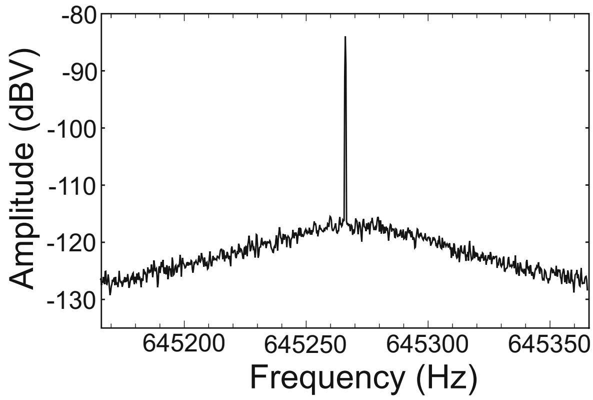

Figure 5.4: Peak measurement spectrum [32].

According to subsubsection 5.1.4 the signal at the amplifier input is given by

$$\begin{aligned} U_{sys} &= R_{sys} I_{sys} \quad \text{with} \quad I_{sys} = \kappa I_p \\ &= \frac{R_{eff} R_{in}/\kappa^2}{R_{eff} + R_{in}/\kappa^2} \kappa I_p \\ &= \kappa I_p R_{eff} \frac{1}{1 + \frac{R_{eff}\kappa^2}{R_{in}}}. \end{aligned} \tag{5.30}$$

The total noise e_{tot} at the input of the amplifier is composed of the thermal noise of the detection system $e_{th} = \sqrt{4k_B T R_{sys}}$, the voltage noise e_n and the current noise i_n. For typical dimensions in the experiment $i_n \ll e_{th}$ can be neglected [22]:

$$e_{tot}^2 = e_n^2 + 4k_B T R_{sys}. \tag{5.31}$$

Thus the signal to noise ratio SNR reads

$$SNR = \sqrt{\frac{1}{\left(1 + \frac{R_{eff}\kappa^2}{R_{in}}\right)^2} \frac{(\kappa I_p R_{eff})^2}{e_n^2 + 4k_B T R_{sys}}}. \tag{5.32}$$

Adjusting the coupling factor κ the signal to noise ratio can be maximised. The optimal coupling factor can be calculated to

$$\kappa_{opt} \approx \left(\frac{e_n^2}{4k_B T R_{eff}^2 / R_{in}}\right)^{\frac{1}{4}} \tag{5.33}$$

which results in an optimised signal to noise ratio

$$SNR = I_p \sqrt{\frac{R_{eff}}{4k_BT\left(1+\frac{e_n}{k_BTR_{in}}\right)}}. \tag{5.34}$$

Hence the SNR depends on the amplitude of the particle but the sensitivity is given by the factor $\sqrt{\frac{R_{eff}}{4k_BT\left(1+\frac{e_n}{k_BTR_{in}}\right)}}$. To obtain a high SNR and therefore a high precision detector it is necessary to

- optimise the detection system to get a high R_{eff}.
- use a high input resistance R_{in} at the input of the amplifier with an relative low voltage noise e_n.
- operate the system at cryogenic temperatures to reduce the impact of thermal noise.

Dip Detection

In contrast to the peak detection using the dip detection the signal to noise ratio SNR is given by the ratio of the peak of the Lorentz spectrum combined with other noise sources and the input noise e_n of the amplifier. Neglecting the input current noise $i_n \ll e_{th}$ and the voltage noise $e_n \ll e_{th}$ in the numerator of the SNR the reads

$$\begin{aligned} SNR &= \sqrt{\frac{4k_BTR_{sys}}{e_n^2}} \\ &= \sqrt{\frac{4k_BT\frac{R_{eff}R_{in}/\kappa^2}{R_{eff}+R_{in}/\kappa^2}}{e_n^2}}. \end{aligned} \tag{5.35}$$

Using a small coupling constant κ the resistance of the system R_{sys} increases but at the same time the signal strength decreases according to (5.30).

Typical signals for dip detection for small and large detuning of the axial frequency with respect to the resonator resonance frequency are shown in Figure 5.5.

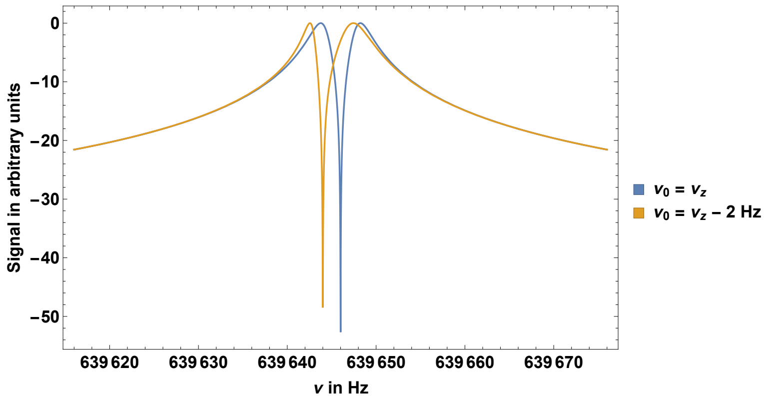

(a) Signal for ν_0 close to ν_z

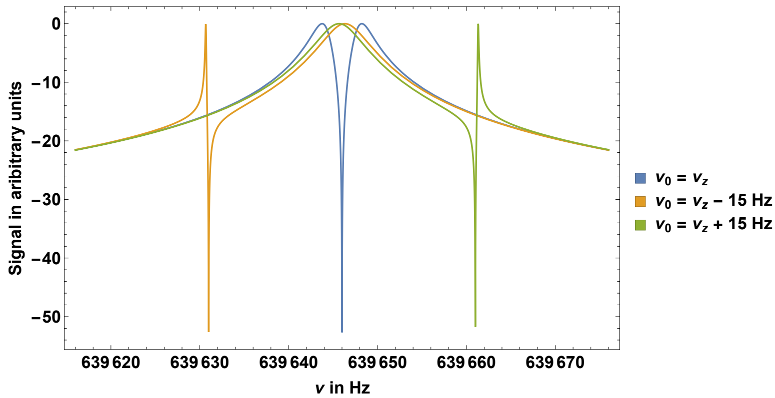

(b) Signal for ν_0 far detuned from ν_z

Figure 5.5: Typical signals for small and large detuning of the axial frequency with respect to the resonator resonance frequency.
$\nu_z = 639\,646\,\mathrm{Hz}$, $\Delta\nu_z = 5\,\mathrm{Hz}$, $\Delta\nu_0 = 25\,\mathrm{Hz}$

Note: To be consistent with other literature it is convenient to redefine $R_p(\omega)$ as the full resistance which has to be measured anyway in the experiment.

5.2. Sideband Coupling

The sideband coupling technique is used for example to determine the radial eigenfrequencies by coupling them to the axial motion and cooling the radial modes. In this section the main idea is presented where a detailed discussion can be found in [33, 34].

Two modes x_j and x_k with frequencies ω_j and ω_k respectively can be coupled by applying a rf-drive

$$\vec{E}(x_j, x_k) = \mathrm{Re}\left(E_0 e^{i\omega_{rf}t}\left(x_j \vec{e}_k + x_k \vec{e}_j\right)\right) \tag{5.36}$$

with amplitude E_0 and frequency ω_{rf}. This rf-drive couples the modes at the sum and difference frequencies $\omega_{rf} = \omega_j \pm \omega_k$. This additional driving field leads to modified equations of motions for the modes

$$\ddot{x}_j + \omega_j^2 x_j = \frac{qE_0}{m} e^{i\omega_{rf}t} x_k \tag{5.37}$$

$$\ddot{x}_k + \omega_k^2 x_k = \frac{qE_0}{m} e^{i\omega_{rf}t} x_j. \tag{5.38}$$

This system of coupled differential equations can be solved by transforming it to a system where the dynamical matrix has only non-diagonal terms and complex eigenvalues which are equivalent to a oscillating system. The transformation is given by

$$x_j \mapsto \frac{X_j(t)}{\sqrt{\pi m \omega_j}} e^{i\omega_j t} \tag{5.39}$$

$$x_k \mapsto \frac{X_k(t)}{\sqrt{\pi m \omega_k}} e^{i\omega_k t} \tag{5.40}$$

and focuses on the energy transfer of the modes. The energy transfer rate is given by the driving strength and can by expressed in terms of the so called 'Rabi' frequency

$$\Omega_0 = \frac{qE_0}{2m\sqrt{\omega_j \omega_k}}. \tag{5.41}$$

Obviously the energy transfer increases with higher amplitude E_0 of the applied driving field. In the following the sideband coupling is described for the example of coupling the axial and magnetron motion. If the axial amplitude vanishes initially and a resonant rf-drive, i.e. $\omega_{rf} = \omega_z + \omega_-$, is applied, the energy transfer between the modes can be expressed as oscillating amplitudes of the modes

$$z(t) = z_0 \sin\left(\frac{\Omega_0}{2} t\right) \sin\left(\omega_z t + \phi_z\right) \tag{5.42}$$

$$\rho_-(t) = \rho_{-,0} \cos\left(\frac{\Omega_0}{2} t\right) \sin\left(\omega_- t + \phi_-\right) \tag{5.43}$$

where ϕ_z and ϕ_- are arbitrary phases. The amplitudes z_0 and $\rho_{-,0}$ are modulated with $\frac{\Omega_0}{2}$. A Fourier transformation of (5.42) reveals modified eigenfrequencies

$$\omega_{l,r} = \omega_z \mp \frac{\Omega_0}{2}. \tag{5.44}$$

Consequently, applying a rf-drive results in a double dip spectrum of the axial frequency, instead of the single dip spectrum discussed before. This double dip is shown in Figure 5.6. For resonant coupling the distance between the two dips equals the resonant Rabi frequency Ω_0. If a non-resonant rf-drive is applied, i.e. $\omega_{rf} = \omega_z + \omega_- + \delta$ with $\delta \neq 0$, the system oscillates with the so called modified or reduced Rabi frequency $\Omega = \sqrt{\Omega_0^2 + \delta^2}$ and the energy is not transferred completely between the two modes. The resulting modified eigenfrequencies can be calculated [33] to be

$$\omega_{l,r} = \omega_z - \frac{1}{2}(\delta \pm \Omega). \tag{5.45}$$

Finally the magnetron frequency can be obtained via

$$\omega_l + \omega_r = 2\omega_z - \delta = \omega_z + \omega_{rf} - \omega_-. \tag{5.46}$$

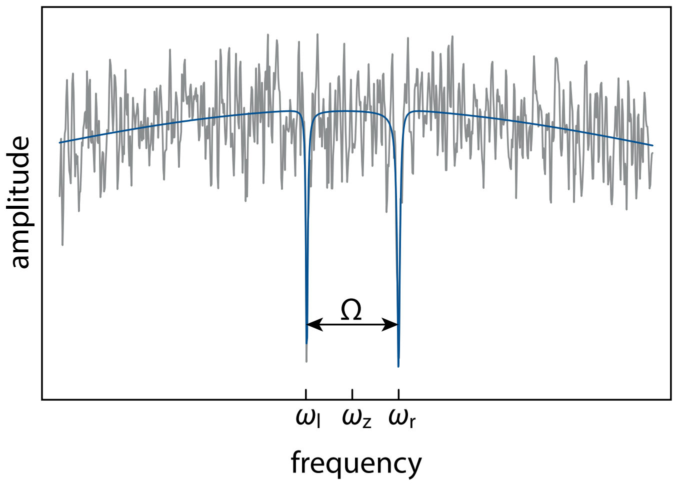

Figure 5.6: Double dip spectrum [20].

The same calculation can be done for the modified cyclotron frequency ω_+. If a rf-drive with frequency $\omega_{rf} = \omega_+ - \omega_z + \delta$ is applied, the modified cyclotron frequency can be calculated according to

$$\omega_l + \omega_r = 2\omega_z - \delta = \omega_z - \omega_{rf} + \omega_+. \tag{5.47}$$

In summary, using the technique of sideband coupling the radial frequencies can be measured indirectly by coupling them to the axial motion.

5.3. Detection of the Larmor Frequency

In contrast to the three eigenmotions $\omega_\pm$ and ω_z of the particle in the Penning trap, the spin procession frequency or Larmor frequency ω_L is not accompanied by an image current induced by the particle in the trap electrodes. Thus the image current detection described in subsection 5.1 can not be used for the Larmor frquenecy ω_L itself. Instead, the spin-flip probability p_{SF} to change the spin state from up to down or vice versa as a function of the excitation frequency ω_{rf} is determined. Fitting the spin flip probability $p_{SF}(\omega_{rf})$ the Larmor frequency ω_L can be extracted.

5.3.1. Continuous Stern-Gerlach Effect

To measure the spin state non-destructively the continuous Stern-Gerlach effect [35] is used. The basic idea is to couple the spin magnetic moment $\vec{\mu}_s$ to the axial motion. This can be achieved by adding a strong inhomogeneous magnetic field, called magnetic bottle, which is shown in Figure 5.7. The inhomogeneous magnetic field is implemented by ferromagnetic ring electrode at the centre of the trap which produces the quadratic magnetic field

$$\vec{B}(z,\rho) = B_0\vec{e}_z + B_2\left(\left(z^2 - \frac{\rho^2}{2}\right)\vec{e}_z - \rho z\vec{e}_\rho\right) \tag{5.48}$$

with quadratic component B_2 additionally to the homogeneous field B_0 as it was described in section 2.

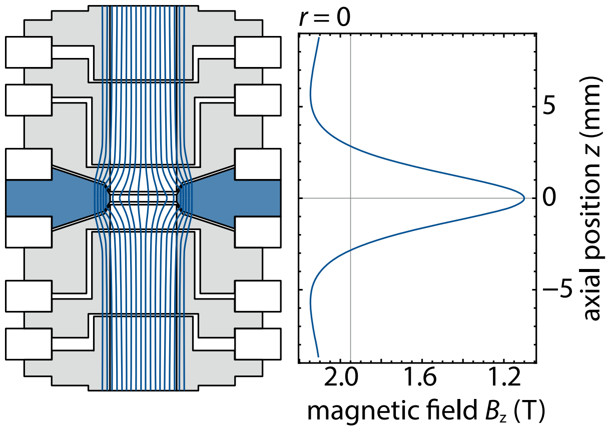

Figure 5.7: Schematic of the particle detection system [20].

Hence the equation of motion for the axial motion has to be modified by adding the magnetic potential $\phi_{mag} = -\vec{\mu}_s\vec{B}$ with the magnetic moment $\vec{\mu}_s = g\frac{q}{2m}\vec{S}$, the axial component of the spin $S_z = \hbar m_s$ and the spin quantum number for the (anti-)proton $m_s = \pm\frac{1}{2}$. Therefore the magnetic potential is given by

$$\phi_{mag} = \pm g\frac{q}{2m}\frac{\hbar}{2}B \tag{5.49}$$

where the energy difference $\Delta\phi_{mag} = g\frac{q\hbar}{2m}B$ can be expressed in terms of $\Delta\phi_{mag} = \hbar\omega_L$ where ω_L denotes the Larmor frequency

$$\omega_L = g\frac{q}{2m}B. \tag{5.50}$$

The additional term in the magnetic potential shifts the energy levels for spin-up and spin-down as shown in Figure 5.8.

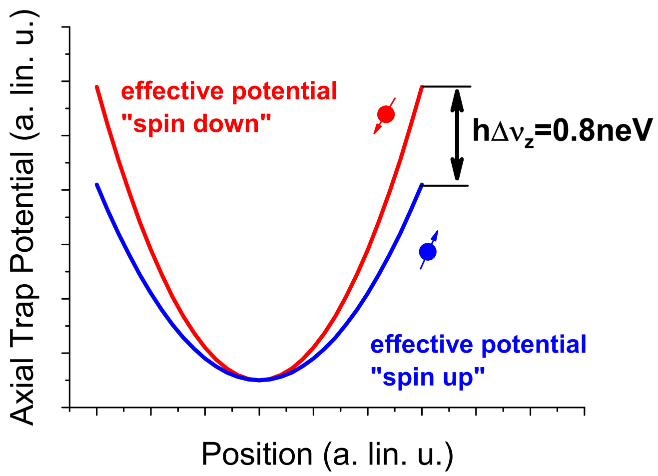

Figure 5.8: Magnetic Potential for spin-up and spin-down state of the spin of the particle [22].

The magnetic potential gives rise to an additional force of $\vec{F}_{mag} = -\vec{\nabla}\phi_{mag} = \vec{\nabla}\left(\vec{\mu}_s\vec{B}\right)$. Thus the equation of motion reads

$$\begin{aligned} m\ddot{z} = F(z) &= -\frac{\partial\phi_{el}(z)}{\partial z} - \frac{\partial\phi_{mag}(z)}{\partial z} \\ &= -2C_2qV_rz + \frac{\partial}{\partial z}\left(g\frac{q}{2m}\vec{S}\vec{B}\right) \\ &= -2C_2qV_rz + \frac{\partial}{\partial z}\left(g\frac{q}{2m}\left(B_0 + B_2z^2\right)S_z\right) \\ &= -2C_2qV_rz + g\frac{q}{m}B_2zS_z \\ &= -2C_2qV_rz + g\frac{q\hbar}{m}B_2zm_s \\ &= -2C_2qV_rz \pm g\frac{q\hbar}{2m}B_2z \end{aligned} \tag{5.51}$$

where the upper and lower sign in the second term always denote the spin up and down state respectively. The axial equation of motion still describes a harmonic oscillator but now with a shifted axial frequency

$$\begin{aligned} \omega_{z,SF} &= \sqrt{\frac{2C_2qV_r \mp g\frac{q\hbar}{2m}B_2}{m}} \\ &= \omega_z\sqrt{1 \mp g\frac{q\hbar}{2m^2\omega_z^2}B_2} \end{aligned} \tag{5.52}$$

where ω_z is the axial frequency without the magnetic bottle. Since the correction term is small compared to ω_z Taylor expansion to first order can be used which yields

$$\begin{aligned}\omega_{z,SF} &= \omega_z \left(1 \mp g \frac{q\hbar}{4m^2\omega_z^2} B_2\right) \\ &= \omega_z \mp \frac{\Delta\omega_{z,SF}}{2}\end{aligned} \tag{5.53}$$

with the frequency difference between spin up and down state

$$\Delta\omega_{z,SF} = g \frac{q\hbar}{2m^2\omega_z} B_2. \tag{5.54}$$

This technique was introduced by Dehmelt et. al. [36] and successfully applied to electrons and positrons. The challenge to adapt this method to protons or antiprotons is the fact that the (anti-)proton mass is much larger than the mass of the electron or positron. Thus the frequency difference is much smaller according to (5.54).

5.3.2. Double Trap Scheme

As shown in subsubsection 5.3.1 the additional magnetic bottle is essential to determine the spin state of the particle. Unfortunately the strong magnetic field inhomogenity introduced by B_2 gives rise to frequency shifts as discussed before such that measuring the unperturbed cyclotron frequency ω_c would lead to significant systematic uncertainties. This problem is solved by using the so called double trap scheme where the spin detection and high-precision frequency measurements are spatially separated. It was first introduced by Haeffner in 2003 [37]. The double trap scheme uses two traps, the analysis trap (AT) to determine the spin state of the particle and the precision trap (PT) to measure the free cyclotron frequency ω_c and the Larmor frequency ω_L. The schematic procedure is shown in Figure 5.9.

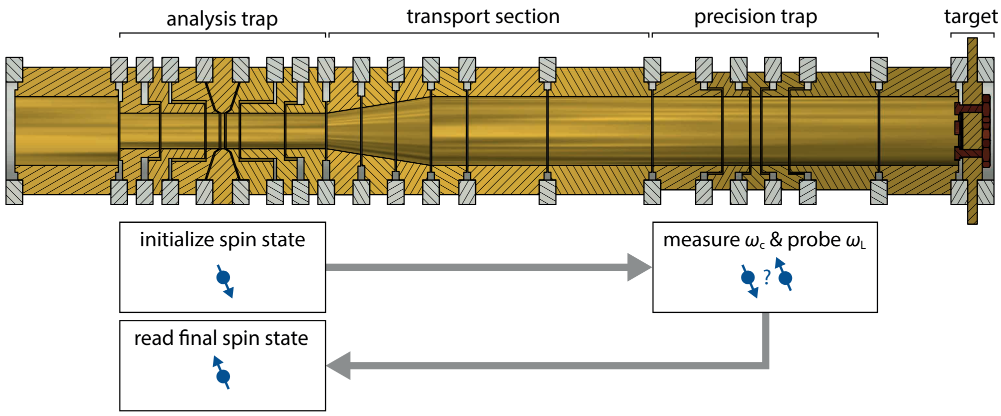

Figure 5.9: Double trap scheme [20].

First the spin state is identified in the AT. Then the particle is transported to the PT where the free cyclotron frequency ω_c is measured while simultaneously a probing frequency ω_{rf} is applied to perform a spin flip. Afterwards the particle is moved back to AT to read out the final spin state. This gives the information whether a spin flip occurred in the PT. After repeating this scheme for many measurements the spin flip probability $p_{SF}(\omega_{rf})$ for the tested frequency ω_{rf} can be determined. Scanning the applied probing frequency ω_{rf} to perform a spin flip the Larmor resonance frequency can be obtained.

6. Temperature Evaluation

Considering precision measurements it is of main importance to characterise and analyse the systematics. To achieve a certain precision goal it is necessary to ensure that the corresponding systematics are smaller that the precision goal. Regarding both measurements, i.e. charge to mass ratio q/m and g-factor, one of the most problematic systematics is the axial temperature which contributes to the modified cyclotron frequency shift as follows

$$\Delta\nu_+(T_z) = \frac{1}{4\pi^2 m\nu_z^2}\frac{B_2}{B_0}k_B T_z. \tag{6.1}$$

Compared to the systematics of the axial frequency $\left(10^{-7}\right)$, B_0-value $\left(10^{-9}\right)$ and B_2-value $\left(10^{-3}\right)$ the systematics for the axial temperature is rather large (1) [22, 32]. Therefore it is of great importance to reduce the systematics for the axial temperature by analysing it more precisely. A way to determine the axial frequency is presented in this section.

6.1. Theoretical Description

The line shape of the particle in the detection system was derived in section 5 and according to (5.20) reads

$$\chi(\nu) = R_p \frac{\left(\nu^2 - \nu_z^2\right)^2}{\left(\nu^2 - \nu_z^2\right)^2 + \left(\frac{1}{\nu\Delta\nu_0}\left(\nu_0^2 - \nu^2\right) + \nu\Delta\nu_z\right)^2}. \tag{6.2}$$

Apparently the particles thermal state moves through a Boltzmann distribution

$$p(T) = \frac{1}{T_0}e^{-T/T_0} \tag{6.3}$$

with average temperature T_0. Taking this into account the thermal line shape is some kind of convolution of the Boltzmann distribution and the original line shape. In a more physical frame the thermal line shape is the original one weighted with the Boltzmann distribution

$$\chi_{\text{th}}(\nu) = \frac{1}{T_0}\int_0^\infty \mathrm{d}T\chi(\nu)e^{-T/T_0}. \tag{6.4}$$

Unfortunately, as described in section 3, the frequency shifts scale with the axial energy of the particle. Taking the first order frequency shift into account the unperturbed axial frequency ν_z is shifted as follows

$$\nu_z \mapsto \nu_z \left(1 + \frac{3C_4}{4C_2^2}\frac{E_z}{qV_r}\right). \tag{6.5}$$

According to the equipartition theorem the relation of the temperature and the average axial energy is given by $E_z = k_B T$ where k_B is the Boltzmann constant [38]. Therefore the thermal line shape reads

$$\chi_{\text{th}}(\nu, T_0) = \frac{1}{T_0}\int_0^\infty \mathrm{d}T \frac{R_p\left(\nu^2 - \nu_z^2\left(1 + \frac{3C_4}{4C_2^2}\frac{k_B T}{qV_r}\right)^2\right)^2}{\left(\nu^2 - \nu_z^2\left(1 + \frac{3C_4}{4C_2^2}\frac{k_B T}{qV_r}\right)^2\right)^2 + \left(\frac{1}{\nu\Delta\nu_0}\left(\nu_0^2 - \nu^2\right) + \nu\Delta\nu_z\right)^2} e^{-T/T_0}. \tag{6.6}$$

The signal on the FFT then reads

$$S = 10\log_{10}\left[A \cdot \chi_{\text{th}} + B\right] \tag{6.7}$$

where A and B are related to the resonator and amplifier noise, i.e. the noise floor, respectively. If the particle shorts the detection system at its resonance frequency ν_z, the signal reads $10\log_{10}[B] = \beta$ where β denotes the amplifier noise. Therefore the scaling factor B is given by

$$B = 10^{\frac{\beta}{10}}. \tag{6.8}$$

In contrast, for frequencies not equal to the axial frequency but still on the peak of the resonator the noise of the resonator dominates, i.e. the signal reads $10\log_{10}\left[A \cdot \chi_{\text{off-resonant}} + B\right] = \alpha$ where α denotes the resonator noise. Thus the scaling factor A is given by

$$A = \frac{10^{\frac{\alpha}{10}} - B}{\chi_{\text{off-resonant}}}. \tag{6.9}$$

To summarise, the movement of the thermal state of the particle leads to an asymmetry in the line shape. Beside the negative aspect of this phenomenon, it can be used to determine the average temperature T_0 of the system.

In the following two different approaches are discussed to extract the average temperature out of the asymmetric line shape.

6.2. Asymmetric Line Fitting - SNR

One way to determine the average temperature T_0 of the system is to consider the SNR as a function of the tuning ratio TR. Having a closer look at (6.6) it becomes clear that the SNR also changes with the average temperature T_0. For higher temperatures the slope of the $SNR(TR)$ curve should be higher than for lower temperatures. The advantage is that the data is not as noisy as for fitting the spectra directly which is further discussed in subsection 6.3.

Trying to fit the SNR as a function of the tuning ratio TR also has the advantage that it is sufficient to use the line shape on resonance with the resonator, i.e. $\nu = \nu_0$ which is given by (5.21)

$$\chi(\nu) = R_p \frac{\left(\nu^2 - \nu_z^2\right)^2}{\left(\nu^2 - \nu_z^2\right)^2 + \left(\nu \Delta\nu_z\right)^2} \tag{6.10}$$

since to determine the SNR the line shape of the resonator far away from the axial frequency does not contribute. On one hand this simplifies expression (6.6) to

$$\chi_{\text{th}}(\nu, T_0) = \frac{1}{T_0} \int_0^\infty \mathrm{d}T \frac{R_p \left(\nu^2 - \nu_z^2 \left(1 + \frac{3C_4}{4C_2^2} \frac{k_B T}{qV_r}\right)^2\right)^2}{\left(\nu^2 - \nu_z^2 \left(1 + \frac{3C_4}{4C_2^2} \frac{k_B T}{qV_r}\right)^2\right)^2 + \left(\nu \Delta\nu_z\right)^2} e^{-T/T_0} \tag{6.11}$$

and on the other hand it improves the computing time. Unfortunately there exists no closed analytic solution neither for (6.6) nor (6.11). Hence the integral has to be evaluated numerically and consequently the fitting routines of Mathematica can not be used. Therefore the SNR as a function of the tuning ratio TR has to be simulated for several average temperatures T_0 and afterwards the best fitting T_0 can be obtained by minimising the χ^2 value. However, those simulations take a lot of computing time since the numerical integral has to be evaluated for every TR and every bin of the FFT of the whole spectrum. Afterwards the SNR for each simulated spectrum can be extracted. This procedure has to be done for every single guess of the temperature T_0. Finally the optimal T_0 can be determined.

6.2.1. Characterisation of the Fitting Routine

First the fitting routine has to be developed and tested. For this purpose data sets for FFT spans of 25 Hz, 50 Hz and 100 Hz were recorded. While in the previous subsection the general idea of extracting the average temperature was discussed, now a detailed discussion of the fitting routine itself is given.

Before starting the measurement the quantities $\frac{\partial \nu_z}{\partial V_r}$ and $\frac{\partial \nu_z}{\partial TR}$ have to be measured for the LabVIEW routine. The measurement routine itself varies the tuning ratio TR and measures or fits several quantities. The variation of the TR causes a change in the coefficients C_j and thus modulates the strength of asymmetry introduced by the Boltzmann distributed motion of the thermal state of the particle. For the fitting routine significant quantities are the SNR, dip width $\Delta\nu_z$, ring voltage V_r, axial frequency ν_z, resonator and amplifier noise level. Since the LabVIEW routine scans several times through the tuning ratio interval the mean values and standard deviations for each TR have to be calculated. An example for those quantities is given in Figure 6.1.

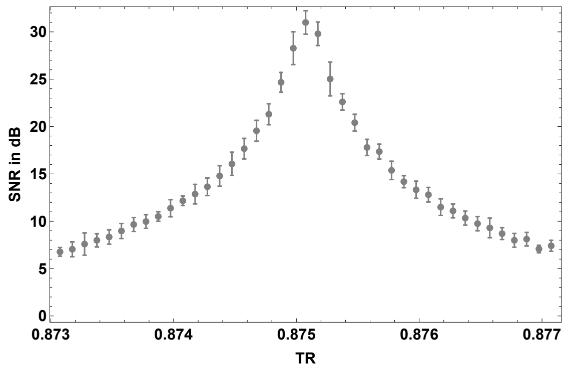

(a) SNR in dB

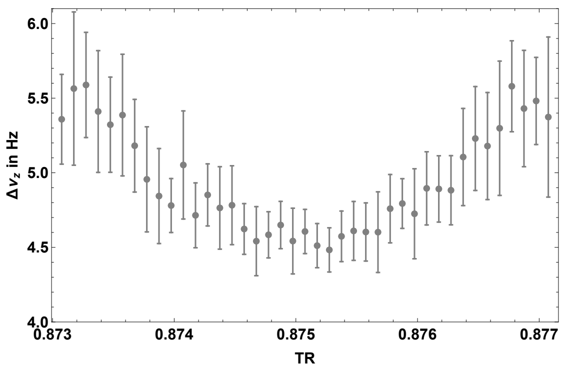

(b) Dip width $\Delta\nu_z$ in Hz

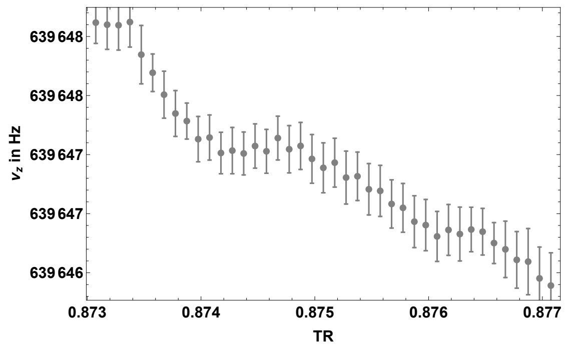

(c) Axial frequency ν_z in Hz

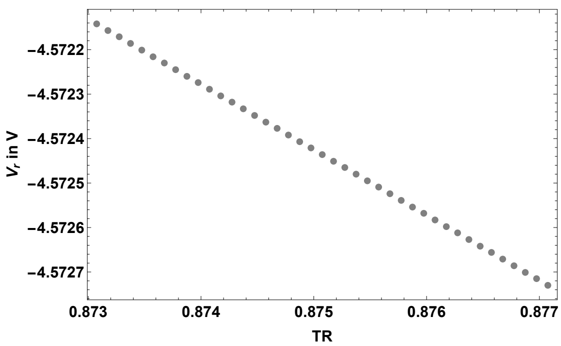

(d) Ring voltage V_r in Hz

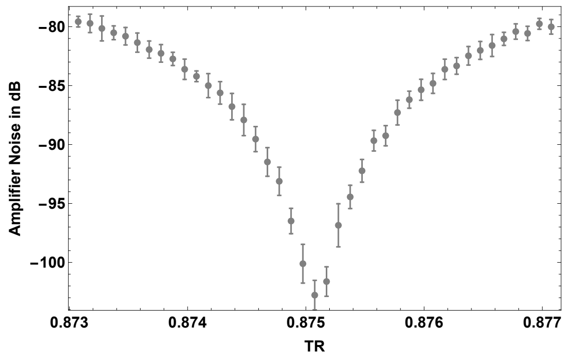

(e) Amplifier noise in dB

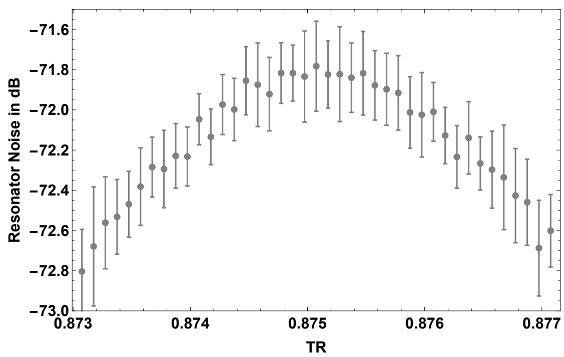

(f) Resonator noise in dB

Figure 6.1: Mean values for a FFT span of 25 Hz.

Afterwards the optimal tuning ratio TR_{opt} can be determined by taking the TR where the highest SNR is achieved. Furthermore the optimal dip width $\Delta\nu_{z,opt}$ is determined and according to section 5 the resistance R_p can be calculated as follows

$$\tau_z = \frac{1}{2\pi\Delta\nu_z} \tag{6.12}$$

$$R_p = \frac{m}{\tau_z}\left(\frac{D_z}{q}\right)^2 \tag{6.13}$$

where $\tau_z = \frac{1}{\gamma_z}$ denotes the damping time constant and the optimal values for the dip width has to be used. Also the quantities α and β, which denote the resonator and amplifier noise respectively, are determined for the optimal tuning ratio. Besides, the coefficients C_2 and C_4 have to be calculated. According to subsection 2.1 the second expansion coefficient can be directly calculated from the ring voltage and the axial frequency, i.e. $C_2 = \frac{2\pi^2 m\nu_z^2}{qV_r}$. As described in subsection 2.2 the coefficients $C_j = E_j + D_j \cdot TR$ can be factorised. Moreover, it is assumed that for the optimal tuning ratio no asymmetry is introduced. Therefore, considering TR_{opt} the coefficient C_4 has to vanish, i.e. $0 = C_4 = E_4 + D_4 \cdot TR_{opt}$. This can be used to define E_4 since D_4 is examined to be rather stable. Thus $E_4 = -D_4 \cdot TR_{opt}$ where D_4 is calculated from potential theory and consequently any coefficient $C_4 = E_4 + D_4 \cdot TR$ can be calculated. It is important to stress that the coefficients C_2 and C_4 have to be calculated for each tuning ratio TR individually. Subsequently the integral (6.11) can be evaluated numerically for each frequency of the spectrum for all tuning ratios. Then the SNR has to be calculated which can be done easily be taking the difference between the maximum and minimum of the calculated signal (6.7) since the line shape of the resonator was not considered in (6.11). This whole routine has to be repeated for several average temperatures T_0 of the system. An example is shown in Figure 6.2.

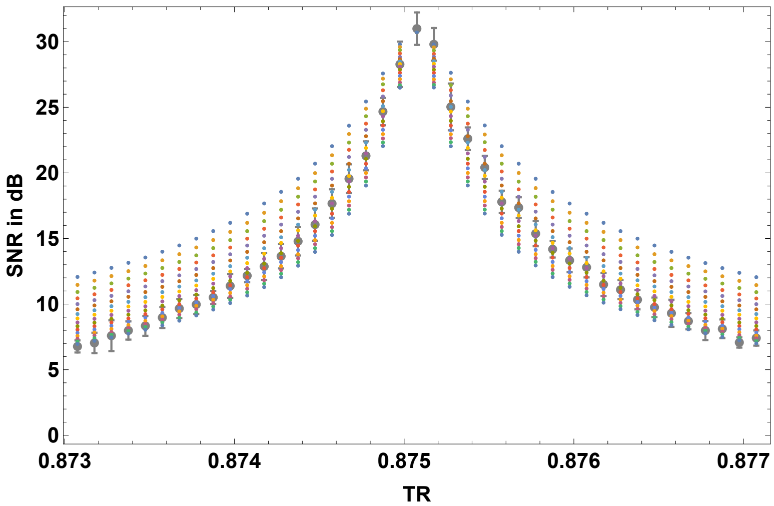

Figure 6.2: Comparison of measured data and simulations for different average temperatures T_0 at a FFT span of 25 Hz.

Afterwards the average temperature T_0 which fits the measured data best can be determined by minimising the χ^2 value which can be calculated as

$$\chi^2 = \sum_i \left(\frac{f_i - x_i}{\sigma_i} \right)^2 \tag{6.14}$$

where x_i denotes the measured data point, f_i denotes the simulated data point and σ_i denotes the measured standard deviation of data point x_i. To get a first estimate of the best fitting average temperature of the system simply T_0 from the simulated values can be determined where the minimal χ^2 value is obtained. In the region of the minimum $\chi^2(T_0)$ behaves as a quasi harmonic function [39,40] such that a simple second order polynomial fit can be used to determine the exact minimum. Furthermore the error of the determined $T_{0,opt}$ value can be calculated by adding 1 to the minimal χ^2 value and solving for the corresponding temperatures $T_{0,l}$ and $T_{0,r}$ [40, 41]. Since the data points were fitted with a quasi harmonic function the errors to the left and right, i.e. $|T_{0,opt} - T_{0,r}|$ and $|T_{0,opt} - T_{0,l}|$, are approximately the same $\Delta T_0 = |T_{0,opt} - T_{0,l}| \approx |T_{0,opt} - T_{0,r}|$. Finally the resulting average temperature of the system is given by $T_0 = T_{0,opt} \pm \Delta T_0$.

25 Hz FFT Span

In Figure 6.3, next to χ^2 as a function of the average temperature T_0, the fit of χ^2 in the region of the minimum is shown.

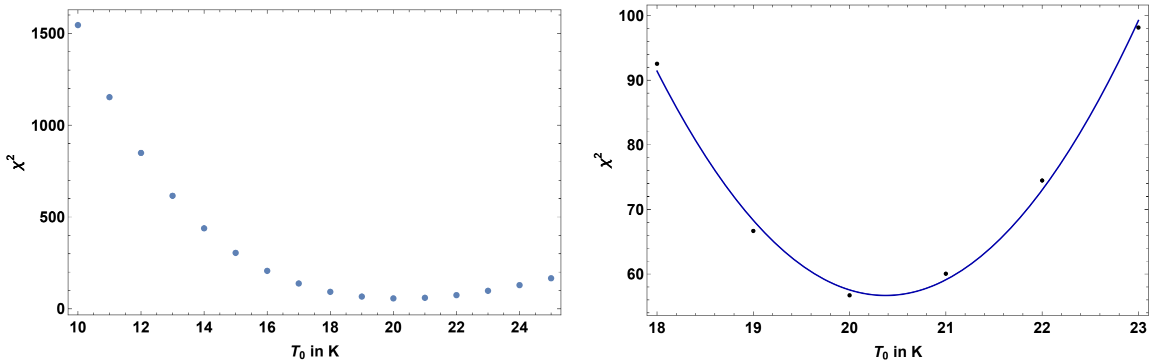

(a) All simulated temperatures

(b) Region of minimum (black: fit, blue: simulation)

Figure 6.3: $\chi^2(T_0)$ for a FFT span of 25 Hz.

Using only the simulations with stepwidth of the temperature $\mathrm{d}T_0 = 1\,\mathrm{K}$ and determining the minimum, the best fit is achieved for 20 K which is shown in Figure 6.4. Fitting the χ^2 curve in the minimum yields a best fitting temperature of $T_0 = (20.4 \pm 0.4)\,\mathrm{K}$.

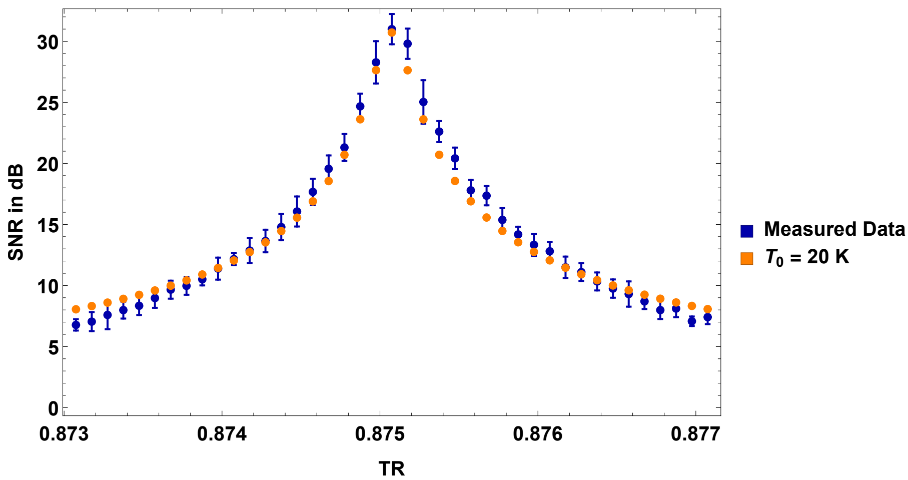

Figure 6.4: Simulated and measured $SNR(TR)$ for a FFT span of 25 Hz.

In Figure 6.4 it becomes clear, that the simulation fits the measured data close to the optimal tuning ratio TR_{opt} quite well whereas for much smaller or larger tuning ratios

TR the simulation deviates more than the scatter of the data, i.e. the standard deviation. It can be stated that close to TR_{opt} the simulation is systematically smaller than the measured data whereas far from TR_{opt} it behaves the opposite way. Therefore it is useful to have a look at the best fitting temperature if some outer tuning ratio points are dropped. According to the observation before the temperature T_0 should decrease with increasing number of dropped outer points since a lower slope corresponds to a lower temperature. However, instead of considering the χ^2-value it is more useful to consider the relative χ^2-value, i.e. χ^2-value divided by the number of data points, since the χ^2 value automatically decreases with decreasing number of points. The result is shown in Figure 6.5. As expected the best fitting temperature and relative χ^2-value decrease with increasing number of dropped outer points.

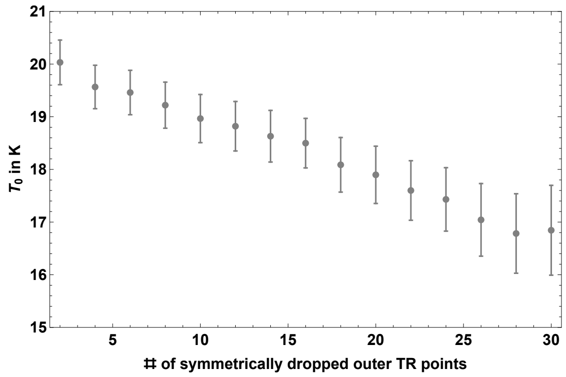

(a) Best fitting T_0

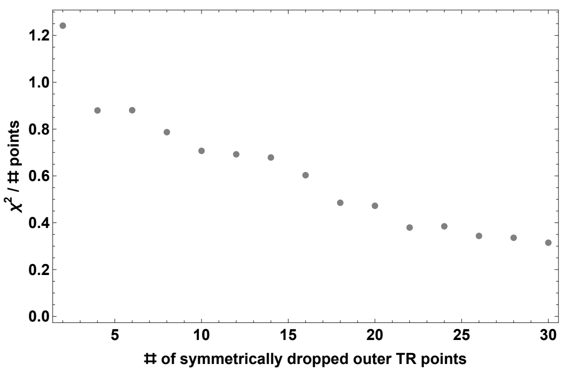

(b) Relative χ^2-value

Figure 6.5: Best fitting average temperature T_0 and corresponding relative χ^2-value after symmetrically dropping outer TR points at a FFT span of 25 Hz.

50 Hz FFT Span

In Figure 6.6, next to χ^2 as a function of the average temperature T_0, the fit of χ^2 in the region of the minimum is shown.

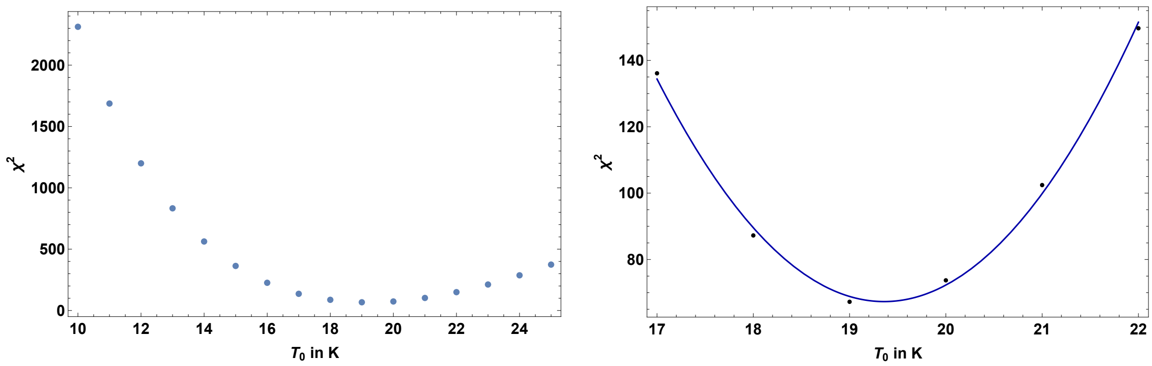

(a) All simulated temperatures

(b) Region of minimum
(black: fit, blue: simulation)

Figure 6.6: $\chi^2(T_0)$ for a FFT span of 50 Hz.

Using only the simulations with stepwidth of the temperature $\mathrm{d}T_0 = 1\,\mathrm{K}$ and determining the minimum, the best fit is achieved for 19 K which is shown in Figure 6.7. Fitting the χ^2 curve in the minimum yields a best temperature of $T_0 = (19.4 \pm 0.3)\,\mathrm{K}$.

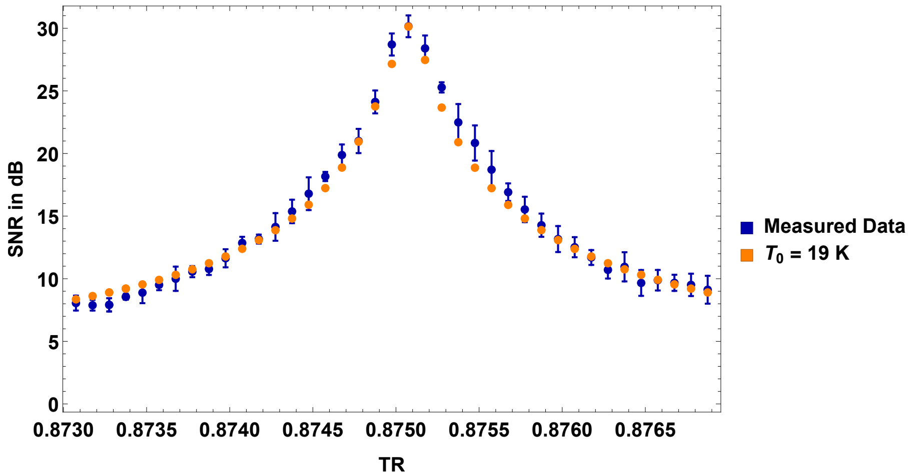

Figure 6.7: Simulated and measured $SNR(TR)$ for a FFT span of 50 Hz.

As for the 25 Hz FFT span it becomes clear, that the simulation fits the measured data close to the optimal tuning ratio TR_{opt} quite well whereas for much smaller or larger tuning ratios TR the simulation deviates more than the scatter of the data, i.e. the standard deviation. The result after dropping outer points is shown in Figure 6.8.As expected the best fitting temperature and relative χ^2-value decrease with increasing number of dropped outer points.

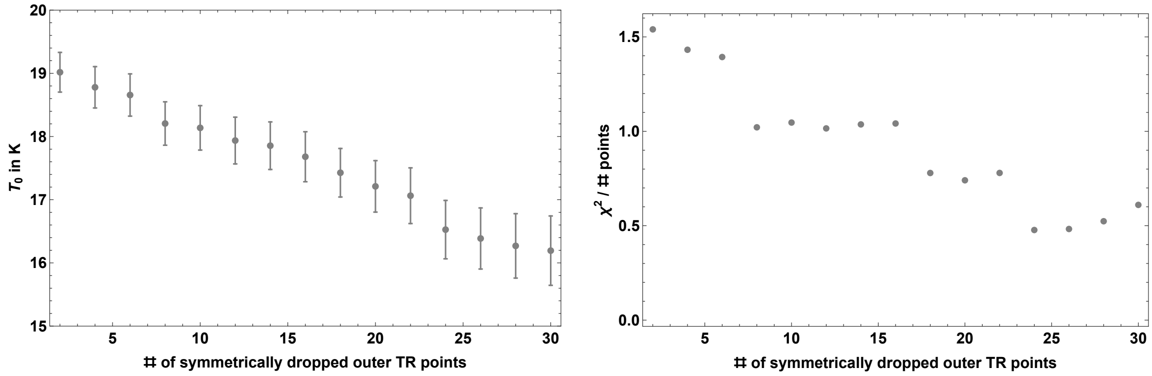

(a) Best fitting T_0

(b) Relative χ^2-value

Figure 6.8: Best fitting average temperature T_0 and corresponding relative χ^2-value after symmetrically dropping outer TR points at a FFT span of 50 Hz.

100 Hz FFT Span

In Figure 6.9, next to χ^2 as a function of the average temperature T_0, the fit of χ^2 in the region of the minimum is shown.

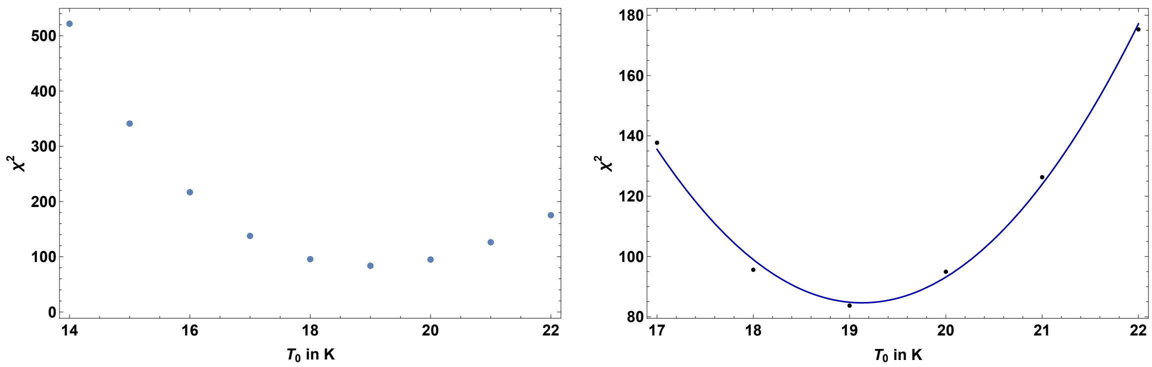

(a) All simulated temperatures

(b) (b) Region of minimum (black: fit, blue: simulation)

Figure 6.9: $\chi^2(T_0)$ for a FFT span of 100 Hz.

Using only the simulations with stepwidth of the temperature $\mathrm{d}T_0 = 1\,\mathrm{K}$ and determining the minimum, the best fit is achieved for 19 K which is shown in Figure 6.10. Fitting the χ^2 curve in the minimum yields a best temperature of $T_0 = (19.1 \pm 0.3)\,\mathrm{K}$.

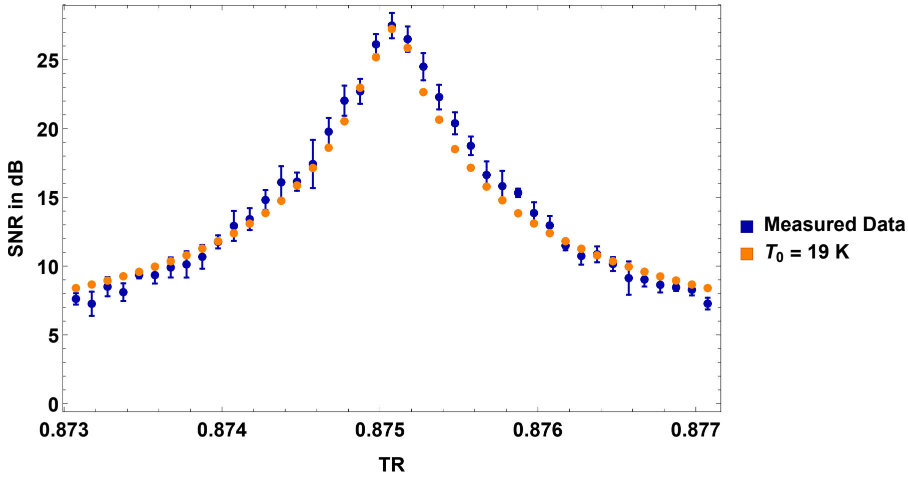

Figure 6.10: Simulated and measured $SNR(TR)$ for a FFT span of 100 Hz.

As for the 25 Hz and 50 Hz FFT span it becomes clear, that the simulation fits the measured data close to the optimal tuning ratio TR_{opt} quite well whereas for much smaller or larger tuning ratios TR the simulation deviates more than the scatter of the data, i.e. the standard deviation. The result after dropping outer points is shown in Figure 6.11. As expected the best fitting temperature and relative χ^2-value decrease with increasing number of dropped outer points.

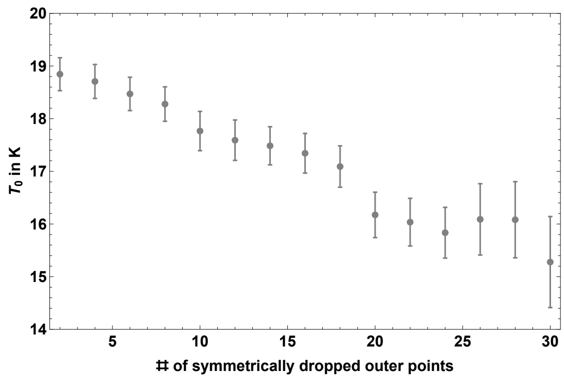

(a) Best fitting T_0

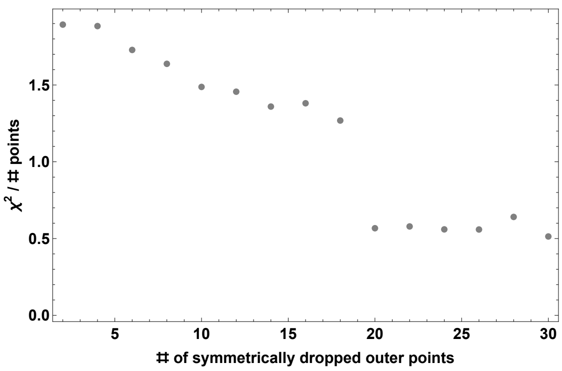

(b) Relative χ^2-value

Figure 6.11: Best fitting average temperature T_0 and corresponding relative χ^2-value after symmetrically dropping outer TR points at a FFT span of 100 Hz.

Impact of higher order coefficients C_j

As mentioned before, the simulations reproduce the measured data quite well for tuning ratios TR close to the optimal tuning ratio TR_{opt} whereas for large detuning the simulations deviate more from the measured data than the scatter of the data, i.e. the standard deviation. A possible explanation could be that for large detuning of the TR from the optimal tuning ratio TR_{opt} the impact of the higher order coefficients C_j becomes significantly large. Therefore the simulations additionally were done including the coefficients C_6, C_8 and C_{10} where they have been calculated from potential theory to get a first impression of the impact. An example is shown in Figure 6.12 for a FFT span of 25 Hz and an average temperature of 20 K.

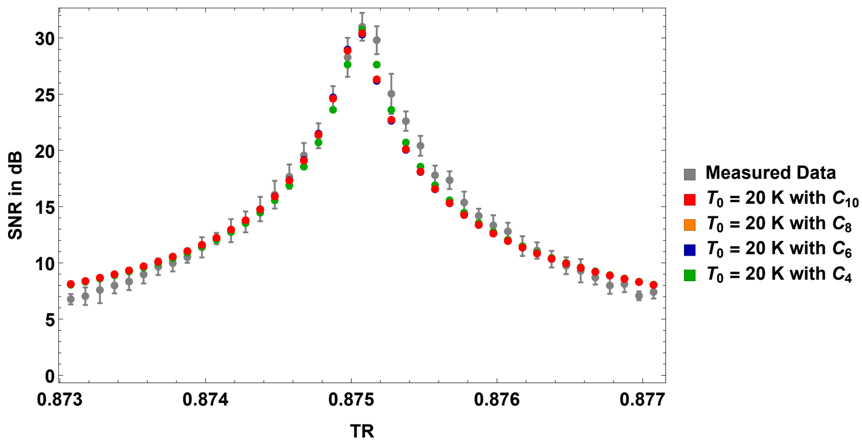

Figure 6.12: Comparison of simulations including different orders of coefficients C_j at a FFT span of 25 Hz.

Figure 6.12 shows that the difference between the simulations including different orders of C_j coefficients is negligible compared to the scatter of the measured data. However, it is noteworthy that the deviation between the simulations is higher close to the optimal tuning ratio TR_{opt} and decreases for larger detuning of the tuning ratio TR. Consequently they behave the opposite way than expected. Even after some additional cross-checks and tests I have not found an explanation for this behaviour. Nevertheless, including higher order coefficients the curve $SNR(TR)$ looks more asymmetric in the regime of the optimal tuning ratio TR_{opt} although the simulation including only C_4 fits the measured data better as the values in Table 6.1 confirm.

Maximum order of C_j coefficients included	χ^2 value
4	56.7063
6	73.8014
8	72.0468
10	72.0574

Table 6.1: Comparison of the χ^2-value for the simulations including different orders of C_j coefficients.

Since the differences are negligible anyway with respect to the standard deviation of the measured data in the following only C_4 is considered.

After the fitting routine was tested and improved, the temperature from several data sets can be evaluated.

Remarks

Regarding the χ^2-value and the uncertainty of the fitted temperature ΔT_0 it is important to keep in mind that with increasing overall χ^2-value often also the slope of $\chi^2(T_0)$ increases which leads to a lower uncertainty. Therefore it is useful always to consider the dimension of the χ^2-value additionally to the uncertainty ΔT_0.

Furthermore the routine could be improved by using a smaller stepwidth $\mathrm{d}T_0$ to obtain more precise results. Due to computation time and remaining time of the internship it was necessary to stay with a rather high stepwidth. Consequently in the future this routine could be optimised by reducing $\mathrm{d}T_0$.

Moreover, instead of assuming that C_4 vanishes for TR_{opt} the coefficient C_4 could be determined from burst measurements close the the TR scans. This could improve the fit.

6.2.2. Evaluating Feedback Data

Here tuning ratio TR scans for different feedback strengths are evaluated.

In total seven data sets with different dip widths $\Delta\nu_z$ were measured. As in subsubsection 6.2.1 for every data set the best fitting temperature is calculated using the χ^2-method and additionally the behaviour of the best fitting temperature after dropping outer points is considered. Afterwards the results are summarised.

It is also noteworthy that the measured data still is quite noisy such that the optimal tuning ratio TR_{opt} not always can be determined by simply taking the maximal SNR value but it has to be 'guessed' manually to obtain better results of the simulations.

Data Set 1:
The dip with of this data set reads $\Delta\nu_z = (1.8 \pm 0.2)\,\mathrm{Hz}$. The results are shown in Figure 6.13. Using only the simulations the best fitting temperature is $T_0 = 7\,\mathrm{K}$. Fitting the χ^2-curve in the region of the minimum it an average temperature of the system of $T_0 = (7.1 \pm 0.2)\,\mathrm{K}$ is obtained.

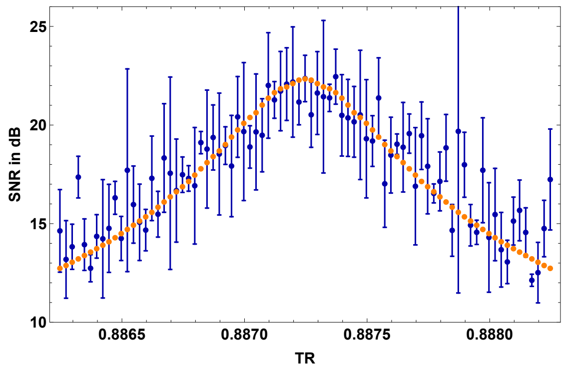

(a) $SNR(TR)$ in dB
(blue: measured data, orange: simulation)

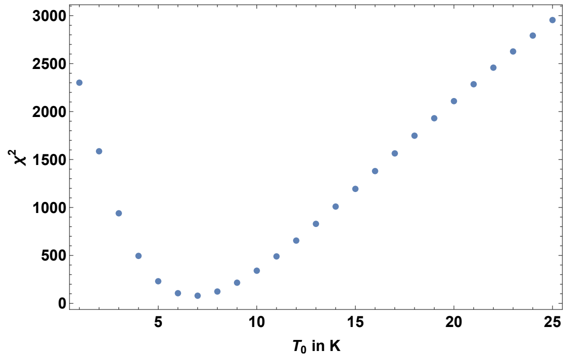

(b) $\chi^2(T_0)$

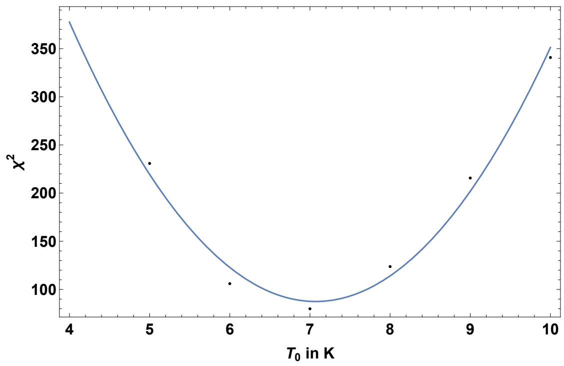

(c) $\chi^2(T_0)$ at minimum
(blue: simulation, black: fit)

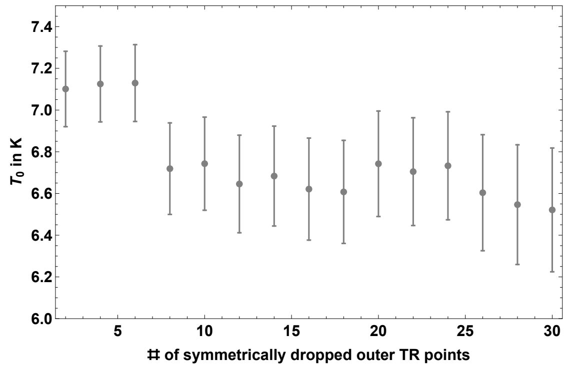

(d) T_0 in K for symmetrically dropped outer points

Figure 6.13: Results for first data set.

Data Set 2:
The dip with of this data set reads $\Delta\nu_z = (2.8 \pm 0.3)\,\text{Hz}$. The results are shown in Figure 6.14. Using only the simulations the best fitting temperature is $T_0 = 8\,\text{K}$. Fitting the χ^2-curve in the region of the minimum it an average temperature of the system of $T_0 = (8.7 \pm 0.3)\,\text{K}$ is obtained.

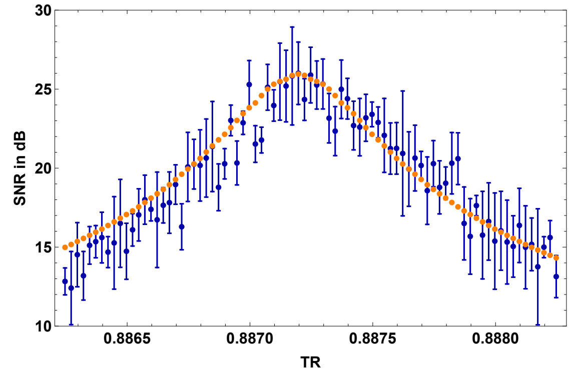

(a) $SNR(TR)$ in dB
(blue: measured data, orange: simulation)

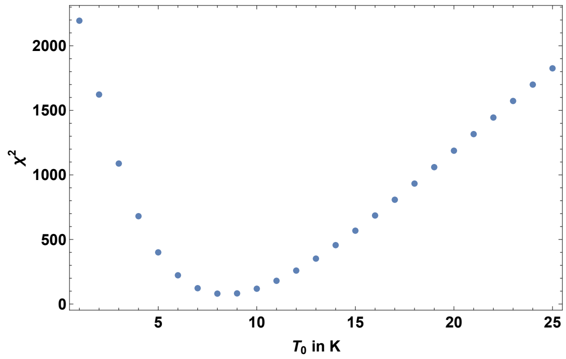

(b) $\chi^2(T_0)$

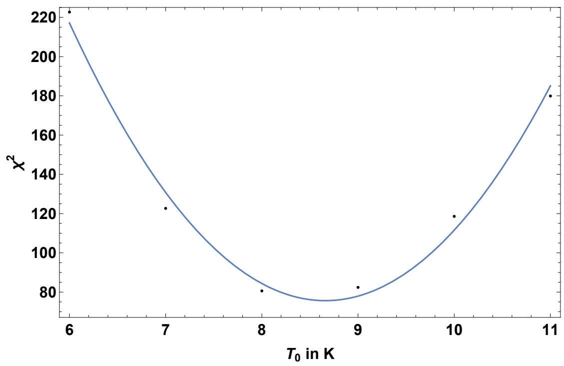

(c) $\chi^2(T_0)$ at minimum
(blue: simulation, black: fit)

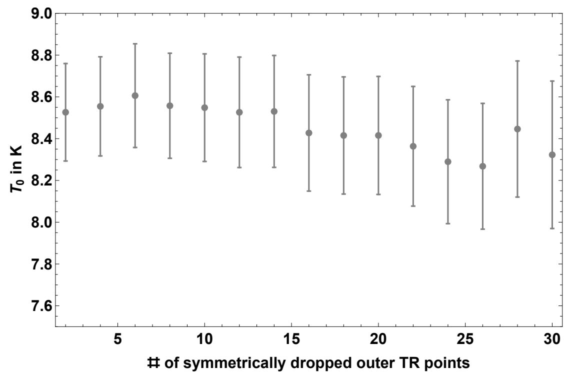

(d) T_0 in K for symmetrically dropped outer points

Figure 6.14: Results for second data set.

Data Set 3:

The dip with of this data set reads $\Delta\nu_z = (4.2 \pm 0.5)\,\text{Hz}$. The results are shown in Figure 6.15. Using only the simulations the best fitting temperature is $T_0 = 20\,\text{K}$. Fitting the χ^2-curve in the region of the minimum it an average temperature of the system of $T_0 = (20.3 \pm 0.5)\,\text{K}$ is obtained.

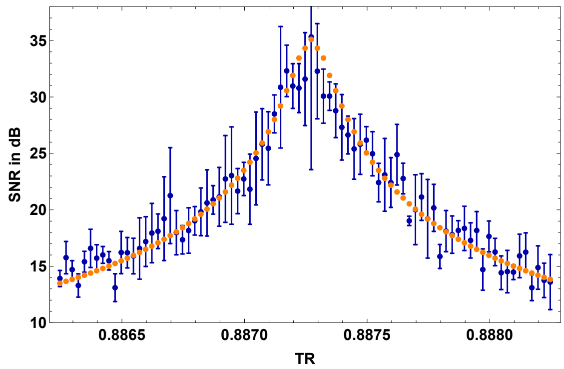

(a) $SNR(TR)$ in dB
(blue: measured data, orange: simulation)

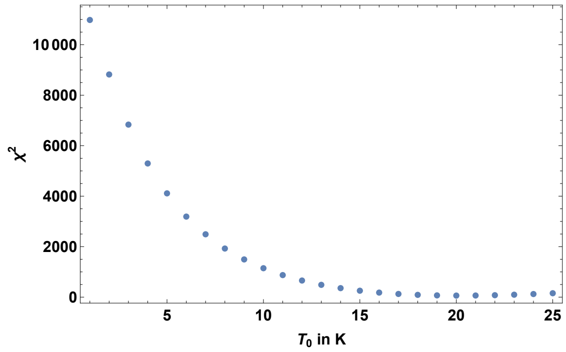

(b) $\chi^2(T_0)$

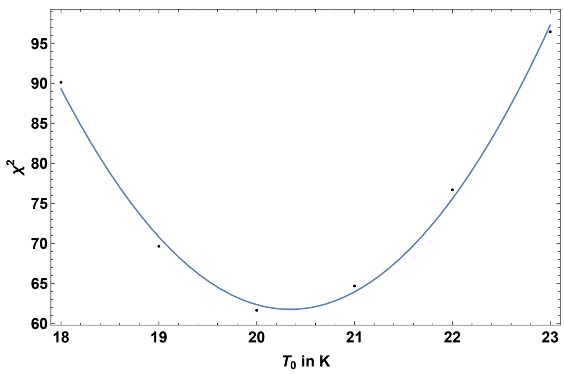

(c) $\chi^2(T_0)$ at minimum
(blue: simulation, black: fit)

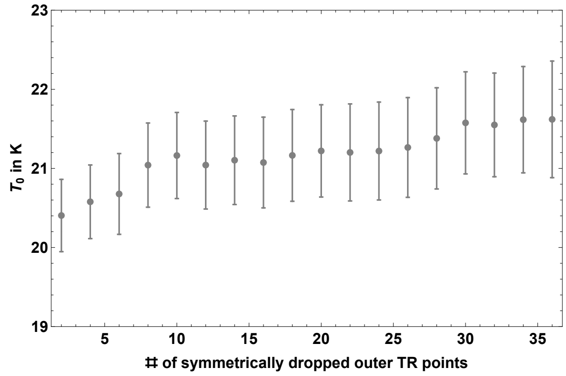

(d) T_0 in K for symmetrically dropped outer points

Figure 6.15: Results for third data set.

Data Set 4:
The dip with of this data set reads $\Delta\nu_z = (6.0 \pm 0.7)\,\text{Hz}$. The results are shown in Figure 6.16. Using only the simulations the best fitting temperature is $T_0 = 13\,\text{K}$. Fitting the χ^2-curve in the region of the minimum it an average temperature of the system of $T_0 = (12.6 \pm 0.4)\,\text{K}$ is obtained.

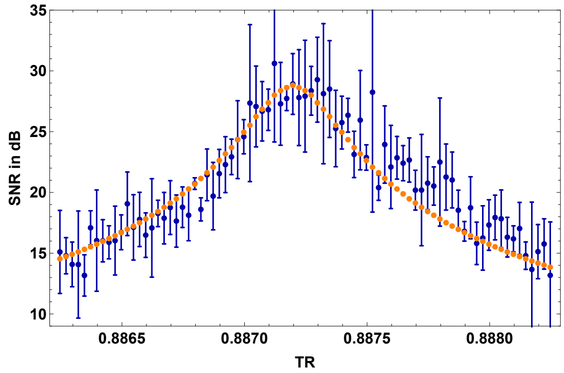

(a) $SNR(TR)$ in dB
(blue: measured data, orange: simulation)

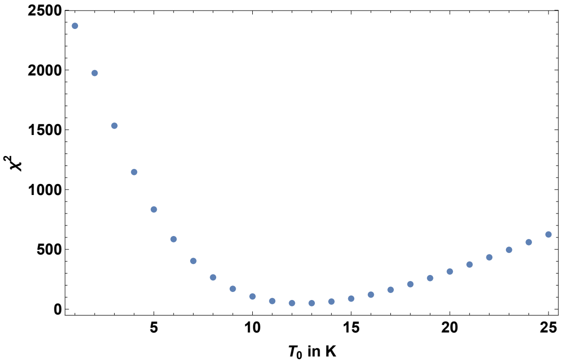

(b) $\chi^2(T_0)$

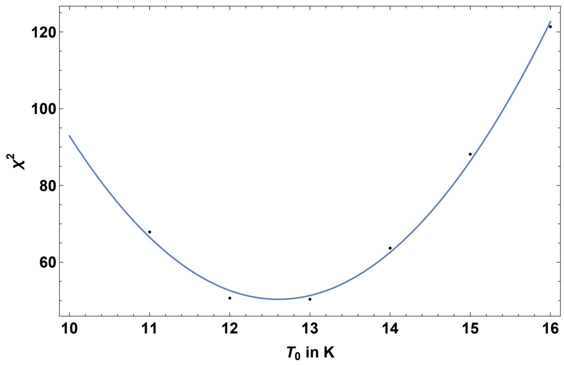

(c) $\chi^2(T_0)$ at minimum
(blue: simulation, black: fit)

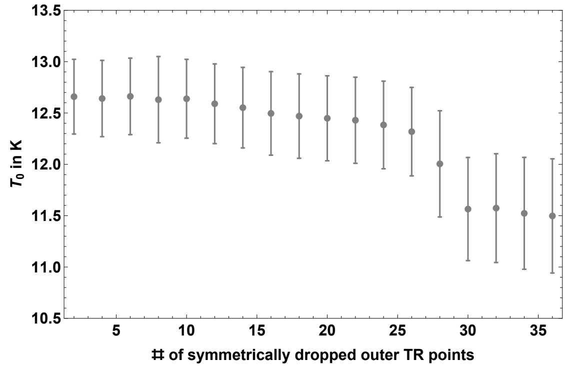

(d) T_0 in K for symmetrically dropped outer points

Figure 6.16: Results for fourth data set.

In the region of the best tuning ratio TR_{opt} the measured data is very noise such that it was a challenge to 'guess' a reasonable optimal tuning ratio TR_{opt} as can be seen in Figure 6.16. Therefore this results have to be considered carefully.

Data Set 5:
The dip with of this data set reads $\Delta\nu_z = (8.2 \pm 0.9)\,\text{Hz}$. The results are shown in Figure 6.17. Using only the simulations the best fitting temperature is $T_0 = 27\,\text{K}$. Fitting the χ^2-curve in the region of the minimum it an average temperature of the system of $T_0 = (27.2 \pm 0.6)\,\text{K}$ is obtained.

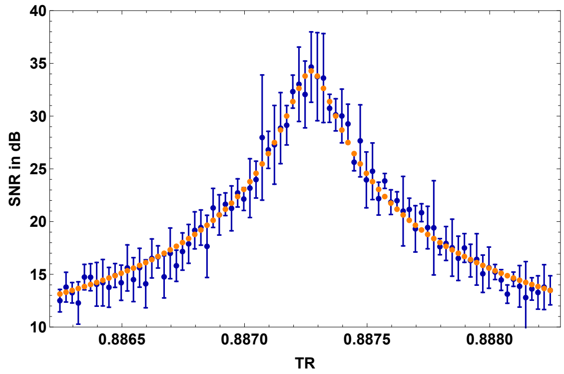

(a) $SNR(TR)$ in dB
(blue: measured data, orange: simulation)

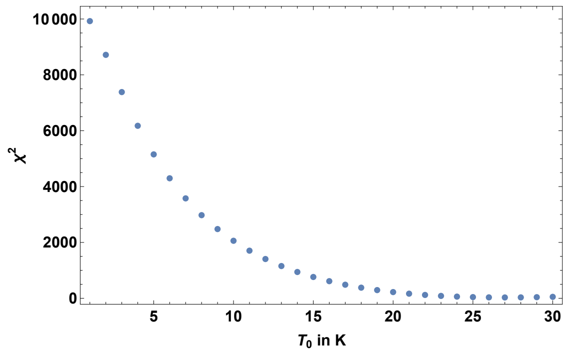

(b) $\chi^2(T_0)$

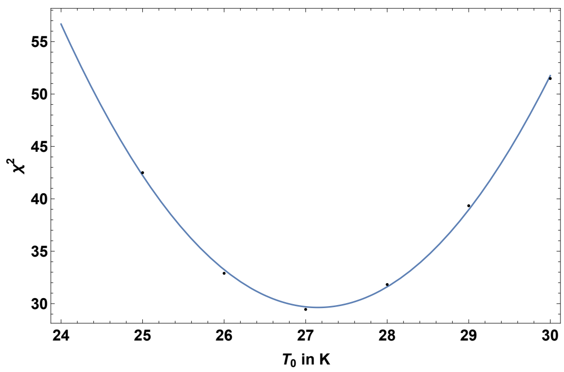

(c) $\chi^2(T_0)$ at minimum
(blue: simulation, black: fit)

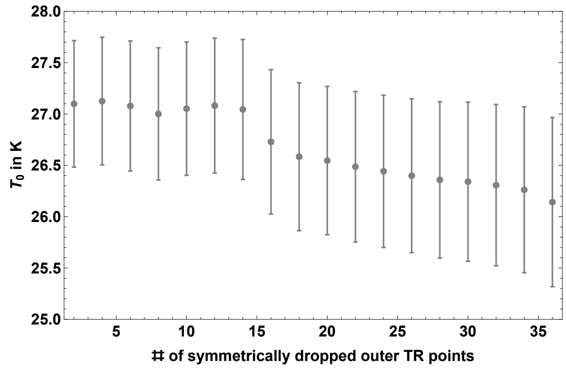

(d) T_0 in K for symmetrically dropped outer points

Figure 6.17: Results for fifth data set.

Data Set 6 & 7:
The dip width of those data sets was around $\Delta\nu_z = 1.2\,\mathrm{Hz}$ and there the LabVIEW fitting routine failed several times such that it was not possible to analyse the data reasonably.

Summary

A summary of the results is shown in Table 6.2 and plotted in Figure 6.18 where the feedback was turned off at $\Delta\nu_z = (4.2 \pm 0.5)\,\mathrm{Hz}$.

Dip width $\Delta\nu_z$ in Hz	Best fitting temperature T_0 in K	χ^2
1.8 ± 0.2	7.1 ± 0.2	87.50
2.8 ± 0.3	8.7 ± 0.3	75.64
4.2 ± 0.5	12.6 ± 0.4	50.35
6.0 ± 0.7	20.3 ± 0.5	61.80
8.2 ± 0.9	27.2 ± 0.6	29.63

Table 6.2: Best fitting temperature T_0 as a function of the dip width $\Delta\nu_z$ and corresponding χ^2-value.

As already discussed in subsubsection 6.2.1 the results show again that the uncertainty of the best fitting temperature T_0 increases with decreasing overall χ^2-value due to the decreasing slope of the $\chi^2(T_0)$-curve.

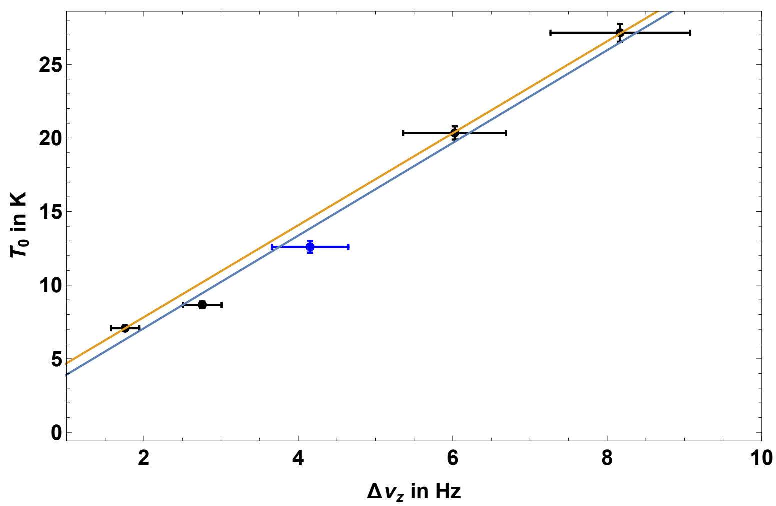

Figure 6.18: Best fitting temperature T_0 as a function of the dip width $\Delta\nu_z$. (black points: simulation, blue point: 'problematic' data set as mentioned before, blue line: fit considering all points, orange line: fit dropping blue point)

Considering all data points the resulting linear dependency reads

$$T_0 = (0.8 \pm 0.3)\,\mathrm{K} + (3 \pm 1)\,\mathrm{K}\,\frac{\Delta\nu_z}{\mathrm{Hz}} \tag{6.15}$$

whereas after dropping the blue point at $\Delta\nu_z = (4.2 \pm 0.5)\,\mathrm{Hz}$

$$T_0 = (1.57 \pm 0.02)\,\mathrm{K} + (3.12 \pm 0.06)\,\mathrm{K}\,\frac{\Delta\nu_z}{\mathrm{Hz}} \tag{6.16}$$

is obtained.

Feedback Gain

In [42] D'Urso derives that for a real feedback amplifier the effective temperature T_e as a function of the gain g is given by

$$T_e = T\left[1 - g + \frac{g^2}{1-g}\frac{T_g}{T}\right] \tag{6.17}$$

where T_g is a feedback 'noise temperature' and T denotes the resistor temperature.
Using

$$R_{p,eff} = R_{p,0}\,(1-g) \tag{6.18}$$

where $R_{p,0}$ is the resistance without feedback ($g = 0$) and

$$R_{p,eff} = 2\pi\Delta\nu_z m\left(\frac{D_z}{q}\right)^2 \tag{6.19}$$

and considering that the gain was turned of at $\Delta\nu_z = 1.2\,\mathrm{Hz}$ the gain for each dip width can be calculated. Consequently the resulting data can be fitted according to (6.17) which is shown in Figure 6.19. The obtained fitting parameters are given by

$$T_g = (1.2 \pm 0.9)\,\mathrm{K} \tag{6.20}$$

$$T = (14.1 \pm 0.4)\,\mathrm{K}. \tag{6.21}$$

Unfortunately as can be seen the fit is very good. Therefore in the future it is important to take more data points especially for $g > 0.5$.

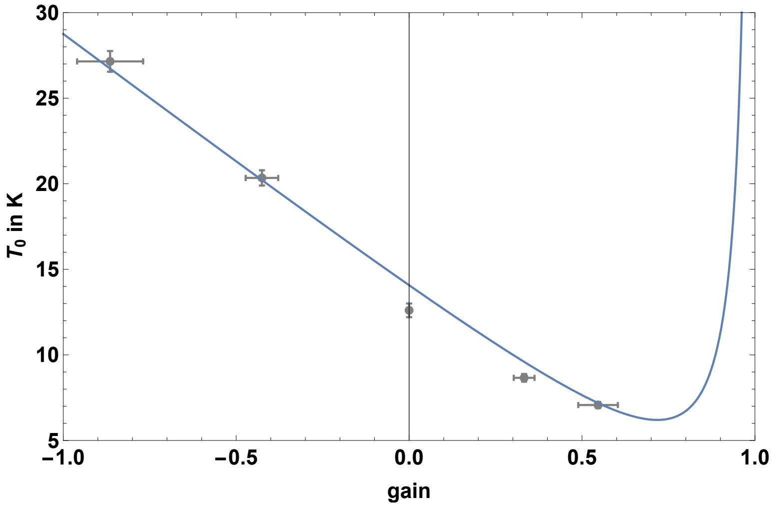

Figure 6.19: T_0 as a function of the gain g.
(gray points: measured and simulated data, blue line: fit according to (6.17))

6.2.3. Axial Temperature of H^- and $\bar{p}$

To compare the charge to mass ratio q/m and the g-factor of the proton and antiproton the corresponding quantities are measure for an antiproton $\bar{p}$ and H^--ion since the correction regarding proton and H^--ion are known precise enough. Switching from antiprotons to H^--ions some adjustments of the experimental setups have to be done. To compare the results afterwards it is important to make sure that the condition were the same, for example that the axial temperature was the same for both measurements. In this section the axial temperature is determined for a $\bar{p}$ and H^- measurement in early 2018.

Hydrogen Ion H^-

The dip with of this data set reads $\Delta\nu_z = (2.5 \pm 0.1)\,\mathrm{Hz}$. The results are shown in Figure 6.20. Using only the simulations the best fitting temperature is $T_0 = 6.5\,\mathrm{K}$. Fitting the χ^2-curve in the region of the minimum it an average temperature of the system of $T_0 = (6.8 \pm 0.4)\,\mathrm{K}$ is obtained.

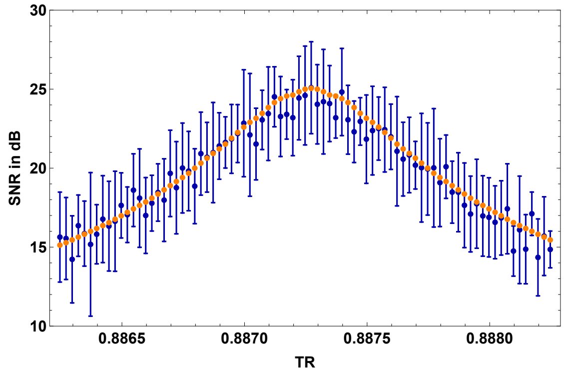

(a) $SNR(TR)$ in dB
(blue: measured data, orange: simulation)

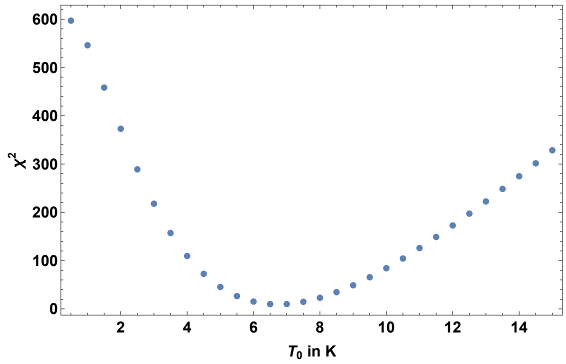

(b) $\chi^2(T_0)$

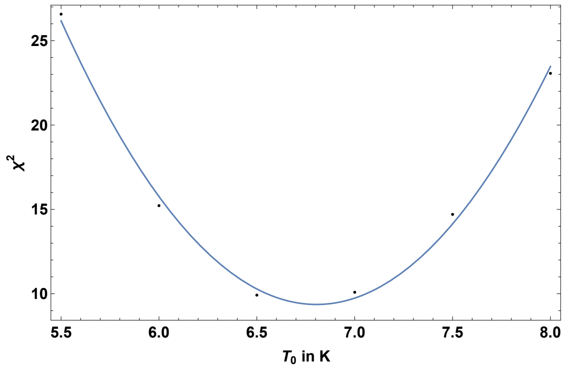

(c) $\chi^2(T_0)$ at minimum
(blue: simulation, black: fit)

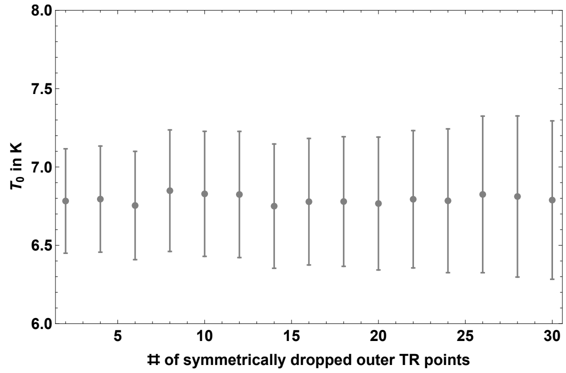

(d) T_0 in K for symmetrically dropped outer points

Figure 6.20: Results for the hydrogen ion H^- data set.

Antiproton $\bar{p}$

The dip with of this data set reads $\Delta\nu_z = (2.34 \pm 0.08)\,\text{Hz}$. The results are shown in Figure 6.21. Using only the simulations the best fitting temperature is $T_0 = 6.5\,\text{K}$. Fitting the χ^2-curve in the region of the minimum it an average temperature of the system of $T_0 = (6.8 \pm 0.4)\,\text{K}$ is obtained.

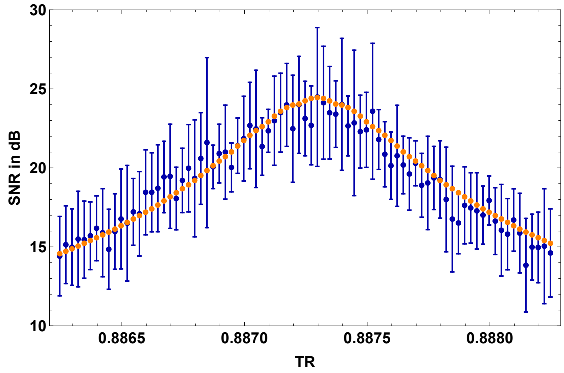

(a) $SNR(TR)$ in dB
(blue: measured data, orange: simulation)

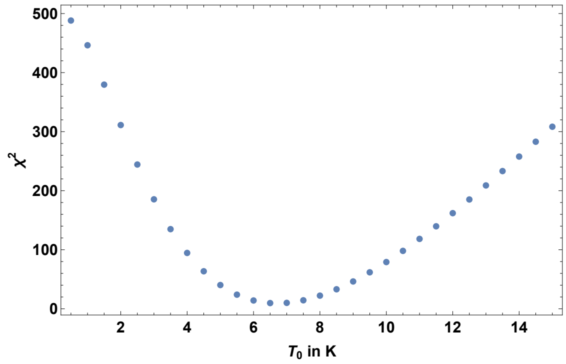

(b) $\chi^2(T_0)$

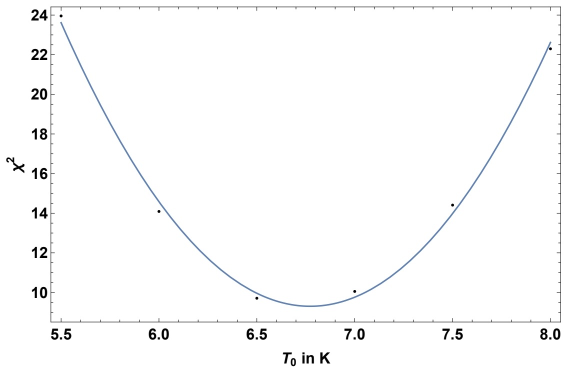

(c) $\chi^2(T_0)$ at minimum
(blue: simulation, black: fit)

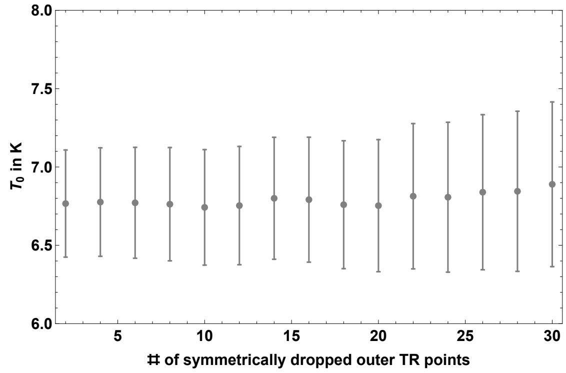

(d) T_0 in K for symmetrically dropped outer points

Figure 6.21: Results for the antiproton $\bar{p}$ data set.

The results show that the axial temperatures for the H^- and $\bar{p}$ measurement were identical within the uncertainties.
Furthermore this result corresponds to an improvement of the systematics for the axial frequency of a factor of approximately 2.5.

6.3. Asymmetric Line Fitting - Single Spectra

Instead of fitting the SNR as a function of the tuning ratio TR, in this approach the spectra are fitted directly. Therefore the full line shape (6.6) has to be considered. The procedure is similar as before. Since the integral still has to be evaluated numerically the line shape has to be simulated for several average temperatures T_0 and the best fitting T_0 can be obtained afterwards using the χ^2-method as described in subsubsection 6.2.1. The only difference is that for single spectra there exists no standard deviation σ_i such that the χ^2-value has to be modified as $\chi^2 = \sum_i (f_i - x_i)^2$. To develop and characterise the fitting routine the data set for 25 Hz from subsubsection 6.2.1 was used.

For the highest SNR, i.e. the optimal tuning ratio TR_{opt}, it is quite simple to fit the spectrum since it is assumed that C_4 vanishes for TR_{opt}. Hence the integral does not have to be evaluated. The result is shown in Figure 6.22.

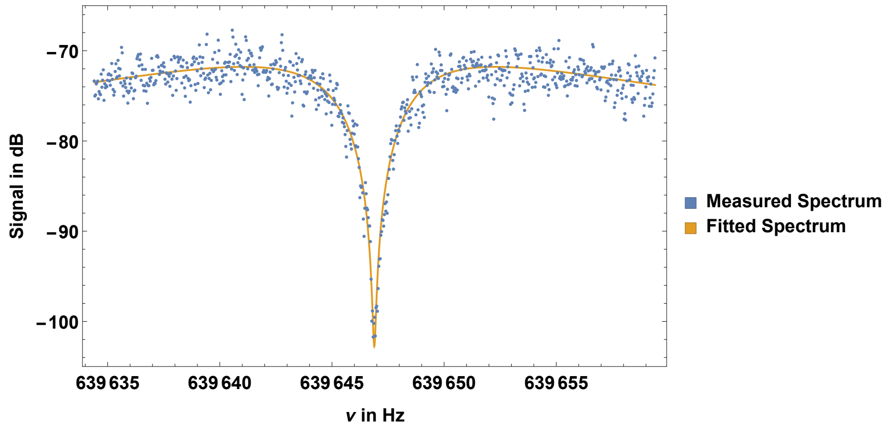

Figure 6.22: Comparison of simulation and measured data for TR_{opt} at a FFT span of 25 Hz.

For a detuning of the tuning ratio TR with respect to TR_{opt} it becomes much more difficult since the integral has to be evaluated numerically. Another problem is the large noise on the spectra. Nevertheless the fitting routine as before can be used to determine the temperature. The resulting temperatures as a function of the tuning ratio from the simulation are shown in Figure 6.23 whereas in Figure 6.24 several examples of the simulation compared to the measured data are given.

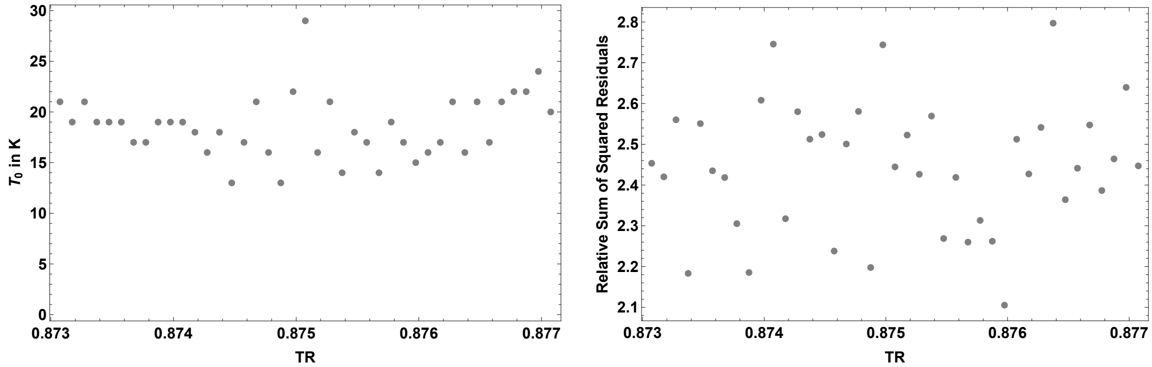

(a) $T_0(TR)$ from simulation (b) Relative sum of squared residuals

Figure 6.23: Results for fitting single spectra at a FFT span of 25 Hz.

The resulting averaged temperature reads $T_0 = (18 \pm 3)\,\mathrm{K}$. Obviously the obtained uncertainty of the temperature is much larger than with the $SNR(TR)$ fitting method for this data set in subsubsection 6.2.1.

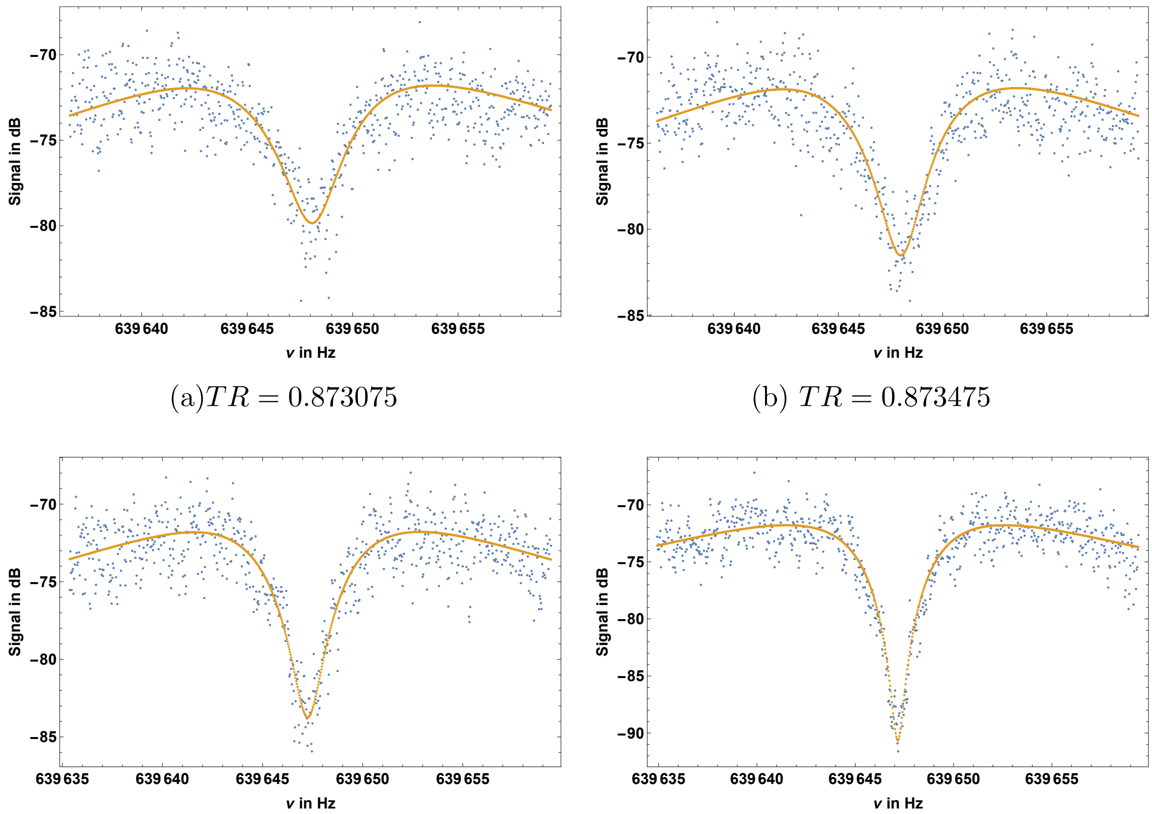

(a)$TR = 0.873075$ (b) $TR = 0.873475$

(c) $TR = 0.873975$ (d) $TR = 0.874475$

Figure 6.24: Comparison of measured and simulated averaged spectra for several tuning ratios $TR < TR_{opt}$ where $TR_{opt} = 0.875075$ for single spectra. (blue: measured data, orange: simulation)

To preserve better results it is useful to average over many spectra measured at the same tuning ratio TR to reduce the noise.

6.4. Asymmetric Line Fitting - Averaged Spectra

Instead of using single spectra all spectra for a certain tuning ratio TR can be averaged. This reduces the noise significantly. Afterwards the temperature of the system can be determined using the χ^2-method described in subsubsection 6.2.1 can be used. The resulting temperatures without and with fitting the χ^2-curve in the region of the minimum are shown in Figure 6.25 whereas in Figure 6.26 several examples of the simulation compared to the measured data are given.

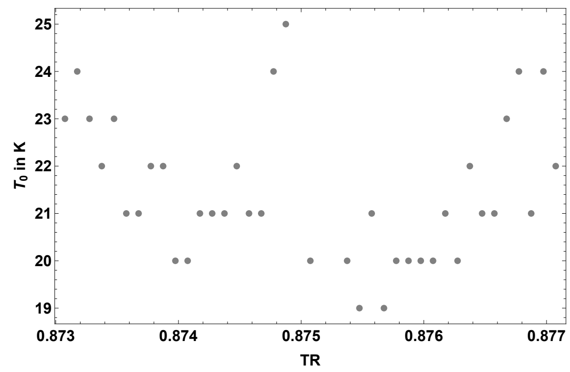

(a) Without fitting

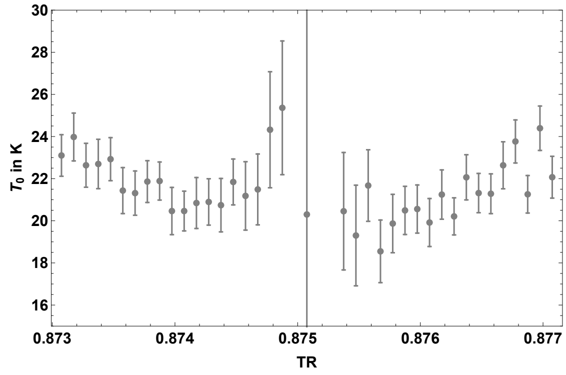

(b) After fitting

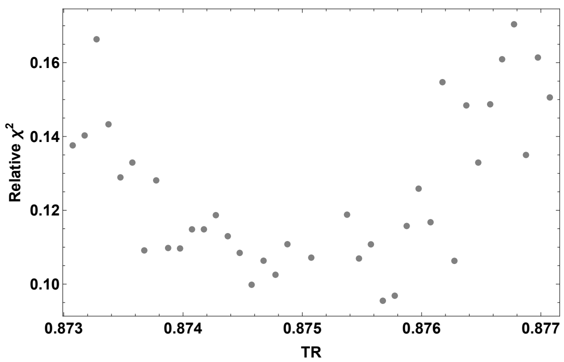

(c) Relative χ^2-value

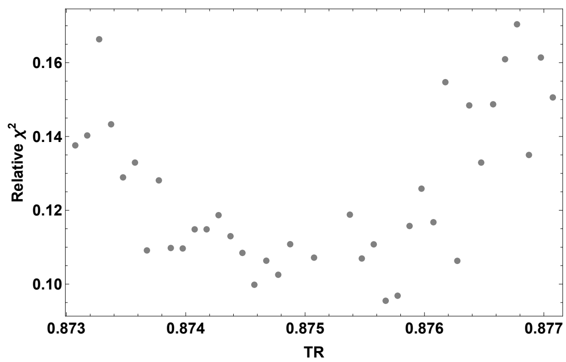

(d)

Figure 6.25: Temperatures T_0 as a function of the tuning ratio at a FFT span of 25 Hz.

The resulting averaged temperature reads $T_0 = (21.6 \pm 1.5)\,\mathrm{K}$. Obviously using averaged spectra the fitting routine provides much better results with respect to the the $SNR(TR)$ fitting but still with an uncertainty much larger than for the $SNR(TR)$ fits.

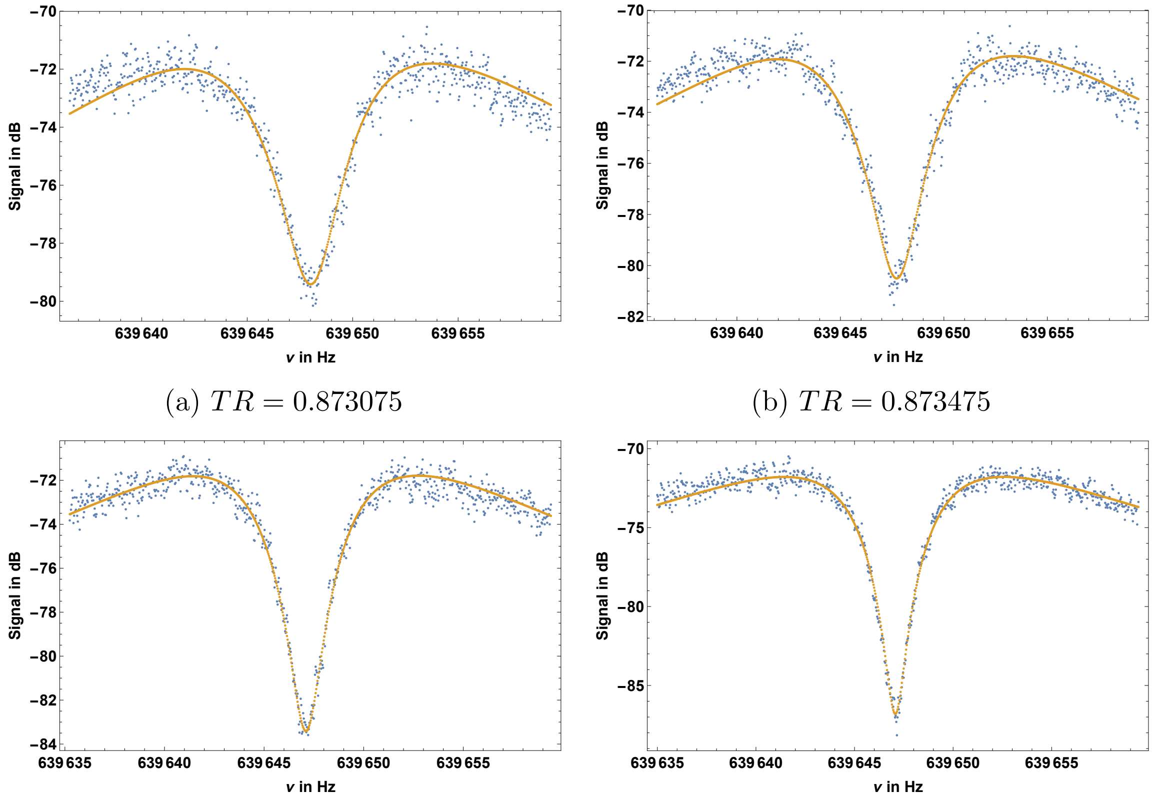

(a) $TR = 0.873075$

(b) $TR = 0.873475$

(c) $TR = 0.873975$

(d) $TR = 0.874475$

Figure 6.26: Comparison of measured and simulated averaged spectra for several tuning ratios $TR < TR_{opt}$ where $TR_{opt} = 0.875075$ for averaged spectra. (blue: measured data, orange: simulation)

It is noteworthy that the fit gets worse for larger detuning of the tuning ratio TR with respect to the optimal tuning ratio TR_{opt} as already mentioned for the $SNR(TR)$ fit method.

7. Phase Sensitive Methods

S. Stahl [43] introduced a new measurement technique to determine the g factor of a bound electron. Instead of measuring the frequency of a particle in the Penning trap directly, the phase sensitive detection is based on the determination of the phase. Typically such a measurement is on the order of one magnitude faster [20].

7.1. Measurement Technique

The phase sensitive method is based on the fact that the phase of particle evolves with a different velocity compared to a local oscillator if the frequency of the oscillator does not match the resonance frequency of the particle exactly. This can be used to determine the Larmor frequency ν_L since a spin flip of a particle leads to frequency change as described in subsection 5.3. The basic principle of the phase sensitive method is shown in Figure 7.1.

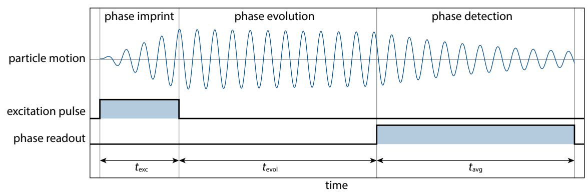

Figure 7.1: Principle of phase method measurements [20].

First an excitation with well defined but unknown frequency ν_{rf} close to the expected axial frequency $\nu_{rf} \approx \nu_z$ is performed. This imprints the well defined but unknown phase of the local oscillator to the axial particle motion. After the excitation the particle is decoupled from the local oscillator. During the following free evolution time t_{evo} the phase of the particle evolves freely with the axial resonance frequency ν_z. Afterwards the particle is re-coupled to the local oscillator and the phase information is read out with an FFT. Finally the particle is cooled down to the initial energy value and the next measurement starts.

In case of a spin flip the Larmor frequency can be determined as follows:
The relative phase of the particle in the initial state is measured

$$\Delta\phi_1(^\circ) = 360\,(\nu_{rf} - \nu_z) \cdot t_{evo}. \tag{7.1}$$

Then a spin flip is performed which leads to a change of the axial frequency $\Delta\nu_z$. Thus the repeated measurement of the relative phase gives

$$\Delta\phi_2(^\circ) = 360\left(\nu_{rf} - (\nu_z + \Delta\nu_z)\right) \cdot t_{evo}. \tag{7.2}$$

Now the difference of the relative phase differences can be evaluated

$$\begin{aligned} \Delta\phi(^\circ) &= \Delta\phi_1(^\circ) - \Delta\phi_2(^\circ) \\ &= 360\Delta\nu_z \cdot t_{evo}. \end{aligned} \tag{7.3}$$

Thus the frequency difference

$$\Delta\nu_z = \frac{\Delta\phi(^\circ)}{360} \cdot \frac{1}{t_{evo}} \tag{7.4}$$

can be extracted. A schematic sketch of this principle is shown in Figure 7.2.

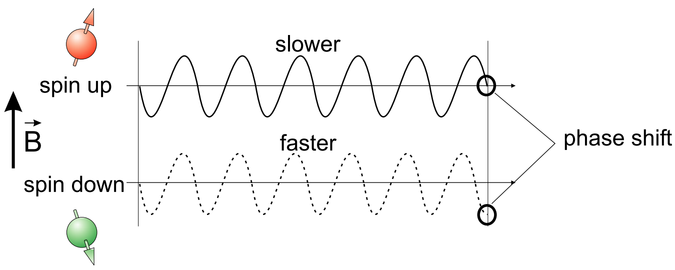

Figure 7.2: Principle of frequency differences and corresponding phase shifts [43].

The relation between frequency resolution and phase resolution is given by

$$\sigma\left(\Delta\nu_z\right) = \frac{1}{T}\frac{\sigma\left(\Delta\phi(^\circ)\right)}{360} \tag{7.5}$$

where $\sigma\left(\Delta\nu_z\right)$ is the frequency resolution, $\sigma\left(\Delta\phi(^\circ)\right)$ is the phase resolution, i.e. the phase scatter or uncertainty (standard deviation) in the phase determination, and T denotes the measuring time [43]. Therefore, to obtain a high frequency resolution it is important to reduce the phase scatter in the phase determination. Basic measurements on the phase scatter are discussed in subsection 7.4.

In conclusion, the phase sensitive method gives an advantage of a factor $\frac{\sigma(\Delta\phi(^\circ))}{360}$ compared to the Fourier limit. Actually, the Fourier limit is the worst case which can occur.

7.2. Contribution of the Averaging Time τ_{avg} of the FFT to the SNR

Next to experimental parameters also the averaging time τ_{avg} of the FFT has an impact on the SNR.

Using the peak detection the particle is excited and then cools down due to the interaction with the detector. Therefore the signal decreases exponentially since the particle decays. Hence the averaging time τ_{avg} of the FFT has a large impact on the SNR. During the averaging times τ_{avg} the particle already decays such that the SNR decreases. Thus for large τ_{avg} only noise is measured whereas for short τ_{avg} white noise still limits the stability. To determine the optimal averaging time τ_{avg} the dependency is examined in this section.

In section 5 the image current induced by the motion of the particle in the penning trap was derived

$$I_p = \frac{q}{D_z}\dot{z} = \frac{q}{D_z}\omega_z z. \tag{7.6}$$

To express the image current in terms of the energy of the particle the energy of a harmonic oscillator $E_z = \frac{1}{2}m\omega_z^2 z^2$ can be considered which leads to

$$I_p = \frac{q}{D_z}\sqrt{\frac{2E_z}{m}}. \tag{7.7}$$

As the amplitude is the quantity of interest it is conventional to use the effective value

$$I_{eff} = \frac{q}{D_z}\sqrt{\frac{E_z}{m}} \tag{7.8}$$

where for an (approximately) harmonic motion the crest factor of $\frac{1}{\sqrt{2}}$ has to be included. Now the decay of the particle due to interaction with the detection system can be taken into account. The energy E_z of the particle after the time t is given by

$$E_z(t) = E_0 e^{-\frac{t}{\tau_z}} \tag{7.9}$$

where E_0 is the initial energy of the particle after excitation and $\tau_z = \frac{1}{\gamma_z} = \frac{m}{R_{sys}}\left(\frac{q}{D_z}\right)^2$ is the cooling time constant with the effective resistance of the detection system on resonance $R_{sys} = \omega_0 QL$. Therefore the effective induced image voltage reads

$$U_{eff} = R_{sys} \frac{q}{D_z} \sqrt{\frac{E_0}{m}} e^{-\frac{t}{2\tau_z}} . \tag{7.10}$$

To obtain the measured signal U_{eff} has to be averaged over the averaging time $\tau_{avg} = \frac{1}{BW}$ of the FFT, where BW is the resolution bandwidth per bin:

$$\begin{aligned} \overline{U}_{eff} &= R_{sys} \frac{q}{D_z} \sqrt{\frac{E_0}{m}} \frac{1}{\tau_{avg}} \int_0^{\tau_{avg}} e^{-\frac{t}{2\tau_z}} \mathrm{d}t \\ &= R_{sys} \frac{q}{D_z} \sqrt{\frac{E_0}{m}} \frac{1}{\tau_{avg}} \left[-2\tau_z e^{-\frac{t}{2\tau_z}} \right]_0^{\tau_{avg}} \\ &= R_{sys} \frac{q}{D_z} \sqrt{\frac{E_0}{m}} \frac{2\tau_z}{\tau_{avg}} \left(1 - e^{-\frac{\tau_{avg}}{2\tau_z}} \right) . \end{aligned} \tag{7.11}$$

Similar to subsubsection 5.1.3 the SNR can be calculated taking the input amplifier noise into account which is given by

$$e_n = \sqrt{4k_B T R_{in} \Delta\nu} \Big|_{\Delta\nu = \frac{1}{\tau_{avg}}} \tag{7.12}$$

where R_{in} is the input resistance of the amplifier in therefore according to subsubsection 5.1.4 is given by $R_{in} = R_{sys}$. Consequently the SNR reads

$$\begin{aligned} SNR &= \sqrt{\frac{\bar{U}_{eff}^2 + e_n^2}{e_n^2}} \\ &= \sqrt{\frac{\left[R_{sys} \frac{q}{D_z} \sqrt{\frac{E_0}{m}} \frac{2\tau_z}{\tau_{avg}} \left(1 - e^{-\frac{\tau_{avg}}{2\tau_z}} \right) \right]^2 + \frac{4k_B T R_{sys}}{\tau_{avg}}}{\frac{4k_B T R_{sys}}{\tau_{avg}}}} \\ &= \sqrt{\frac{\left[R_{sys} \frac{q}{D_z} 2\tau_z \left(1 - e^{-\frac{\tau_{avg}}{2\tau_z}} \right) \right]^2 \frac{E_0}{m\tau_{avg}} + 4k_B T R_{sys}}{4k_B T R_{sys}}} . \end{aligned} \tag{7.13}$$

An example for the SNR as a function of the averaging time τ_{avg} is shown in Figure 7.3. Consequently the achieved SNR can be significantly improved by choosing the averaging time τ_{avg} correctly.

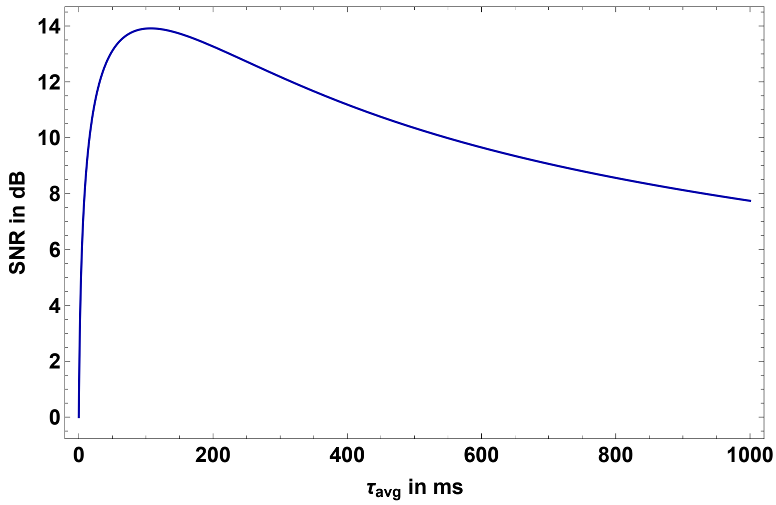

Figure 7.3: SNR as a function of the averaging time τ_{avg} of the FFT.
$\omega_0 = 2\pi\, 645\,261\,\mathrm{Hz}$, $Q = 20000$, $L = 2\,\mathrm{mH}$, $D_z = 0.0103\,\mathrm{m}$, $T = 10\,\mathrm{K}$,
$R_{sys} = \omega_0 L Q$, $\tau_z = \frac{m}{R_{sys}} \left(\frac{D_z}{q}\right)^2$, $E_0 = 0.1\,\mathrm{eV}$

7.3. Relativistic Shift

In the previous sections the particle in the Penning trap was considered non-relativistic since the velocity is much smaller than the speed of light. Nevertheless a small relativistic frequency shift occurs. The axial non-relativistic frequency ω_z was derived in section 2

$$\omega_z = \sqrt{\frac{2qV_rC_2}{m}}. \tag{7.14}$$

To discuss the relativistic frequency shift the mass m has to be replaced by the relativistic mass γm where

$$\gamma = \frac{1}{\sqrt{1 - \left(\frac{v}{c}\right)^2}} \tag{7.15}$$

is the Lorentz factor. Furthermore the relativistic relation for the kinetic energy

$$E_{kin} = \gamma mc^2 - mc^2 \tag{7.16}$$

can be used to express the relativistic mass as

$$\gamma m = \frac{E_{kin}}{c^2} + m. \tag{7.17}$$

Using those relations for the axial kinetic energy the relativistic axial frequency reads

$$
\begin{aligned}
\omega_{z,rel} &= \sqrt{\frac{2qV_rC_2}{\gamma m}} \\
&= \sqrt{\frac{2qV_rC_2}{\frac{E_{kin}}{c^2}+m}} \\
&= \sqrt{\frac{2qV_rC_2}{m}}\frac{1}{\sqrt{1+\frac{E_z}{mc^2}}} \\
&\approx \omega_z\left(1-\frac{E_z}{2mc^2}\right) \\
&= \omega_z + \Delta\omega_{z,rel}
\end{aligned} \tag{7.18}
$$

where the Taylor expansion to first order $\frac{1}{\sqrt{1+x}} \approx 1 - \frac{x}{2}$ for $x \ll 1$ was used and the relativistic frequency shift

$$\frac{\Delta\omega_{z,rel}}{\omega_z} = -\frac{E_z}{2mc^2} \tag{7.19}$$

was introduced. The frequency shift due to relativistic effects is shown in Figure 7.4. The relative frequency shifts are on the order of 10^{-9} such that for typical axial frequencies this corresponds to shifts on the order of mHz. Therefore the impact of relativistic effects can be neglected.

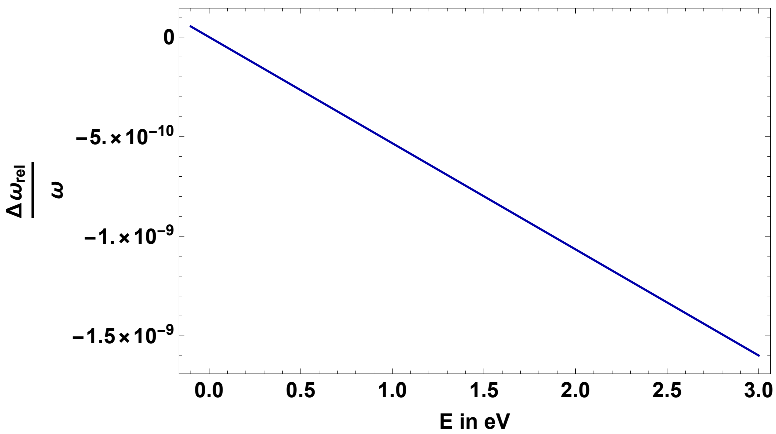

Figure 7.4: Relative relativistic frequency shift as a function of the axial energy.

7.4. Basic Measurements of Phase Scatter

Before implementing phase methods in the experiment, it is useful to have a first glance at the phase scatter that can be achieved for a given SNR. Furthermore the impact of different FFT spans and resolutions can be examined.

The setup for this kind of measurements is given by a clock, two signal generators and a FFT (here SR1 was used). The clock provides a 10 MHz reference for all other instruments such that they are synchronised. One signal generator generates a harmonic signal with a given frequency and defined but unknown phase. The second signal generator introduces white noise to reduce the signal strength and make sure that the noise and signal are uncorrelated. Finally the FFT reads out the phase of the signal.

The measurement routine was implemented in LabVIEW and can be reduced to the following steps:

1. Generate a signal with random but known phase ϕ_1.
2. Wait for a free evolution time $t_{evo} = 1\,\mathrm{s}$.
3. Measure the phase ϕ_2 and the SNR of the signal.

Afterwards the phase difference $\Delta\phi = \phi_2 - \phi_1$ can be calculated. But for further measurements more important the scatter of the phase σ_ϕ, i.e. the standard deviation, can be obtained. Additionally the error of the scatter, which is given by $\frac{\sigma_\phi}{\sqrt{2(N-1)}}$ where N denotes the number of measurements, is calculated.
This is done several times for different signal amplitudes to get a relation between the SNR and the phase scatter σ_ϕ with corresponding error. The result for an example is shown in Figure 7.5.

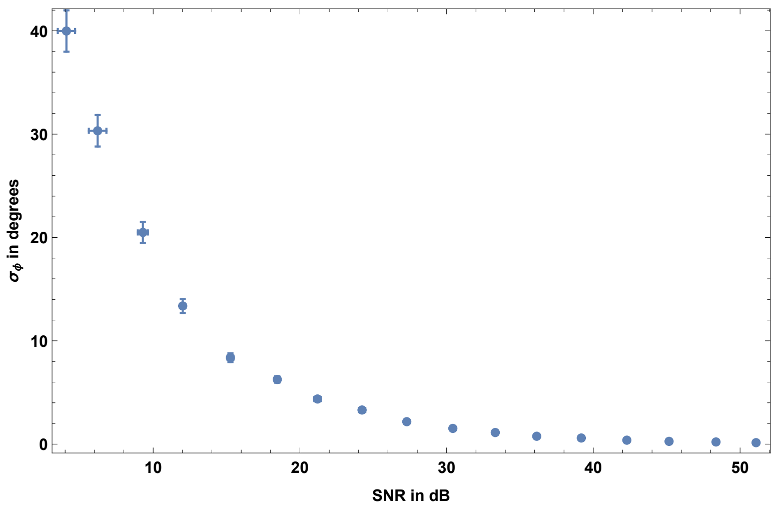

Figure 7.5: Phase scatter σ_ϕ as a function of the SNR for a signal frequency of $\nu = 20\,\text{kHz}$ and $n = 200$ points per SNR.

Vary the Resolution

The resolution of the FFT is the number of frequency bins used. The results for different resolutions are shown in Figure 7.6.

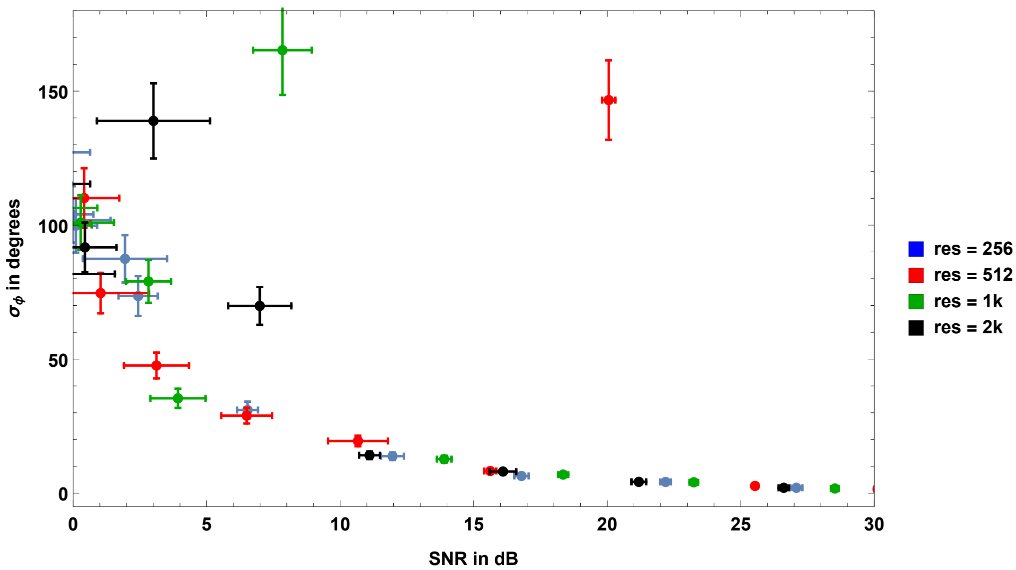

Figure 7.6: Phase scatter σ_ϕ as a function of the SNR for several FFT resolutions for a signal frequency of $\nu = 20\,\text{kHz}$ and $n = 50$ points per SNR.

Vary the Span

The span of the FFT is the difference between the maximal and minimal frequency of the frequency window. The results for different spans are shown in Figure 7.7.

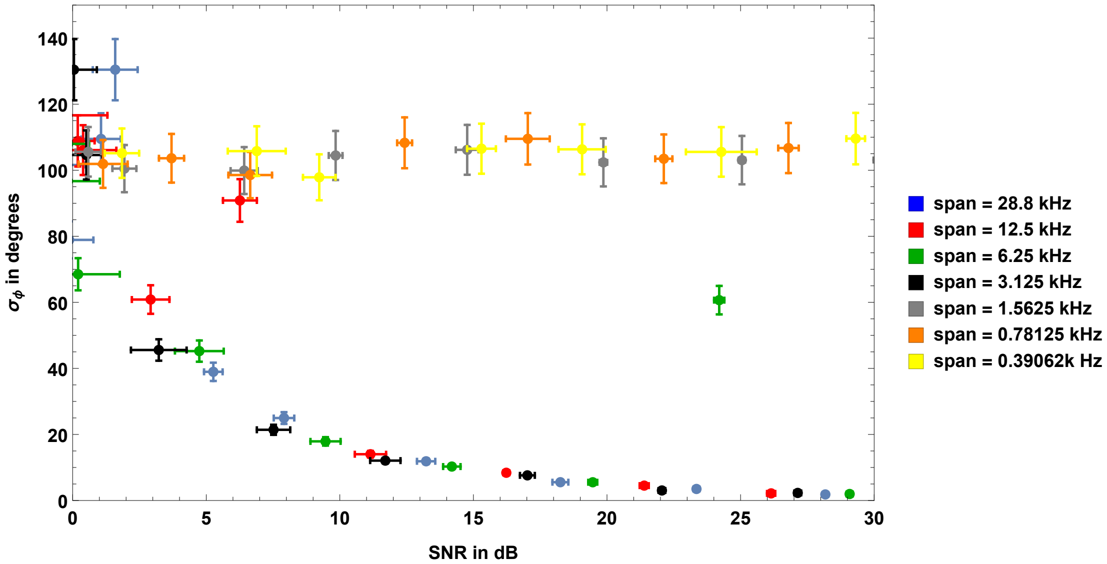

Figure 7.7: Phase scatter σ_ϕ as a function of the SNR for several FFT spans for a signal frequency of $\nu = 20\,\text{kHz}$ and $n = 200$ points per SNR.

Note: Obviously for some measurements the phase scatter σ_ϕ does not decrease with increasing SNR but stays on a rather high level of more than 100°. This scatter is equal to measuring random phases. Honestly I did not understand this unexpected behaviour.

In conclusion the phase scatter σ_ϕ decreases with increasing SNR as expected, without showing significant differences between the different resolutions and spans (with respect to those where not only random phases were measured).

Those results can be used as a benchmark for further measurements, to estimate the necessary SNR to achieve a certain phase scatter σ_ϕ.

Appendix

A. Expansion Coefficients C_j

The complete solution of the Laplace equation with Dirichlet boundary conditions for a trap with p electrodes reads

$$\begin{aligned}\phi(\rho, z) =& \frac{2}{\Lambda}\sum_{n=1}^{\infty}\left[\frac{V_1\cos(k_n z_0) - V_p\cos(k_n\Lambda)}{k_n} + \sum_{i=2}^{p}\frac{V_i - V_{i-1}}{k_n^2 d}\left(\sin(k_n z_{2i}) - \sin(k_n z_{2i-1})\right)\right] \\ &\times \frac{I_0(k_n\rho)}{I_0(k_n a)}\sin\left(k_n\left(z + z_c\right)\right).\end{aligned} \tag{A.1}$$

where $k_n = \frac{n\pi}{\Lambda}$ and z_c denotes the centre of the ring electrode such that the origin already was shifted to z_c. As stated in subsection 2.2 the potential can be expanded at $\rho = 0$ to obtain a better understanding of the potential in axial direction:

$$\phi(0, z) = V_r\sum_{j=0}^{\infty} C_j z^j. \tag{A.2}$$

The coefficients C_j are given by the Taylor expansion coefficients divided by ring electrode voltage V_r

$$C_j = \frac{1}{V_r j!}\frac{\partial^j\phi(0, z)}{\partial z^j}\bigg|_{z=0}. \tag{A.3}$$

The aim of this section is to derive a closed formula for the C_j coefficients. For this purpose it is necessary to calculate the derivatives of $\phi(0, z)$ and to evaluate them at $z = 0$. To shorten the formulas, define the coefficient

$$\begin{aligned}B_n =& \frac{2}{\Lambda}\left[\frac{V_1\cos(k_n z_0) - V_p\cos(k_n\Lambda)}{k_n} + \sum_{i=2}^{p}\frac{V_i - V_{i-1}}{k_n^2 d}\left(\sin(k_n z_{2i}) - \sin(k_n z_{2i-1})\right)\right] \\ &\times \frac{1}{I_0(k_n a)}\end{aligned} \tag{A.4}$$

such that the potential at the radial centre of the trap reads

$$\phi(0, z) = \sum_{n=1}^{\infty} B_n \sin\left(k_n\left(z + z_c\right)\right). \tag{A.5}$$

- j=0:

$$\phi(0,z)\big|_{z=0} = \phi(0,0) = \sum_n B_n \sin(k_n z_c) \tag{A.6}$$

- j=1:

$$\begin{aligned}\frac{\partial\phi(0,z)}{\partial z} &= \sum_n B_n k_n \cos(k_n(z+z_c)) \\ \Rightarrow \frac{\partial\phi(0,z)}{\partial z}\bigg|_{z=0} &= \sum_n B_n k_n \cos(k_n z_c)\end{aligned} \tag{A.7}$$

- j=2:

$$\begin{aligned}\frac{\partial^2\phi(0,z)}{\partial z^2} &= -\sum_n B_n k_n^2 \sin(k_n(z+z_c)) \\ \Rightarrow \frac{\partial^2\phi(0,z)}{\partial z^2}\bigg|_{z=0} &= -\sum_n B_n k_n^2 \sin(k_n z_c)\end{aligned} \tag{A.8}$$

- j=3:

$$\begin{aligned}\frac{\partial^3\phi(0,z)}{\partial z^3} &= -\sum_n B_n k_n^3 \cos(k_n(z+z_c)) \\ \Rightarrow \frac{\partial^3\phi(0,z)}{\partial z^3}\bigg|_{z=0} &= -\sum_n B_n k_n^3 \cos(k_n z_c)\end{aligned} \tag{A.9}$$

- j=4:

$$\begin{aligned}\frac{\partial^4\phi(0,z)}{\partial z^4} &= \sum_n B_n k_n^4 \sin(k_n(z+z_c)) \\ \Rightarrow \frac{\partial^4\phi(0,z)}{\partial z^4}\bigg|_{z=0} &= \sum_n B_n k_n^4 \sin(k_n z_c)\end{aligned} \tag{A.10}$$

Now the idea is to express the change of the sign and sin and cos as shifts of sin. Remembering the relations between sin and cos or using

$$\sin(x+y) = \sin(x)\cos(y) + \sin(y)\cos(x) \tag{A.11}$$

it is easy to see that

$$\begin{aligned}
\sin\left(x+\frac{\pi}{2}\right) &= \cos(x)\\
\sin\left(x+\pi\right) &= -\sin(x)\\
\sin\left(x+\frac{3\pi}{2}\right) &= -\cos(x)\\
\sin\left(x+2\pi\right) &= \sin(x).
\end{aligned} \tag{A.12}$$

Thus a closed formula for the expansion coefficients is given by

$$\begin{aligned}
C_j =& \frac{1}{V_r j!}\sum_n B_n \left(\frac{n\pi}{\Lambda}\right)^j \sin\left(\pi\left(\frac{n z_c}{\Lambda}+\frac{j}{2}\right)\right)\\
=& \frac{2}{j! V_r \Lambda}\sum_{n=1}^{\infty}\left[\frac{V_1\cos(k_n z_0)-V_p\cos(k_n\Lambda)}{k_n}+\sum_{i=2}^{p}\frac{V_i-V_{i-1}}{k_n^2 d}\left(\sin(k_n z_{2i})-\sin(k_n z_{2i-1})\right)\right]\\
&\times\frac{(n\pi/\Lambda)^j}{I_0(k_n a)}\sin\left(\pi\left(\frac{n z_c}{\Lambda}+\frac{j}{2}\right)\right).
\end{aligned} \tag{A.13}$$

In the case of a 5-pole trap the argument of the last sin simplifies to $\frac{\Lambda}{2}(n+j)$ since $z_c = \frac{\pi}{2}$ for any symmetric trap.

List of Figures

List of Tables

References

[1] Maxwell, J. C.: *A dynamical theory of the electromagnetic field.* Philosophical Transactions of the Royal Society of London, 155:459–512, jan 1865.

[2] Fermi, E.: *Versuch einer Theorie der ?-Strahlen. I.* Zeitschrift fr Physik, 88(3-4):161–177, mar 1934.

[3] Glashow, Sheldon L.: *Partial-symmetries of weak interactions.* Nuclear Physics, 22(4):579–588, feb 1961.

[4] Salam, A.: *Weak and electromagnetic interactions.* Conf. Proc. C680519, pages 367–377, 1968.

[5] Weinberg, Steven: *A Model of Leptons.* Physical Review Letters, 19(21):1264–1266, nov 1967.

[6] Brian R. Martin, Graham Shaw: *Particle Physics.* Wiley John + Sons, 2017.

[7] Griffiths, David: *Introduction to Elementary Particles.* Wiley VCH Verlag GmbH, 2008.

[8] Hasert, F.J., S. Kabe, W. Krenz, J. Von Krogh, D. Lanske, J. Morfin, K. Schultze, H. Weerts, G. Bertrand-Coremans, J. Sacton, W. Van Doninck, P. Vilain, R. Baldi, U. Camerini, D.C. Cundy, I. Danilchenko, W.F. Fry, D. Haidt, S. Natali, P. Musset, B. Osculati, R. Palmer, J.B.M. Pattison, D.H. Perkins, A. Pullia, A. Rousset, W. Venus, H. Wachsmuth, V. Brisson, B. Degrange, M. Haguenauer, L. Kluberg, U. Nguyen-Khac, P. Petiau, E. Bellotti, S. Bonetti, D. Cavalli, C. Conta, E. Fiorini, M. Rollier, B. Aubert, D. Blum, L.M. Chounet, P. Heusse, A. Lagarrigue, A.M. Lutz, A. Orkin-Lecourtois, J.P. Vialle, F.W. Bullock, M.J. Esten, T.W. Jones, J. McKenzie, A.G. Michette, G. Myatt and W.G. Scott: *Observation of neutrino-like interactions without muon or electron in the Gargamelle neutrino experiment.* Nuclear Physics B, 73(1):1–22, apr 1974.

[9] Mohapatra, Rabindra N. and Goran Senjanović: *Neutrino Mass and Spontaneous Parity Nonconservation.* Physical Review Letters, 44(14):912–915, apr 1980.

[10] LÜDERS, G.: *On the equivalence of invariance under time reversal and under particle-anti-particle con- jugation for relativistic eld theories.* Kong. Dan. Vid. Sel. Mat. Fys. Med. 28, page 1 – 17, 1954.

[11] PENNING, F.M.: *Die glimmentladung bei niedrigem druck zwischen koaxialen zylindern in einem axialen magnetfeld.* Physica, 3(9):873–894, nov 1936.

[12] PIERCE, J.R.: *Theory and Design of Electron Beams.* 1949.

[13] DEHMELT, HANS: *Experiments with an Isolated Subatomic Particle at Rest.* Nobel Lecture, 29(7):734–738, jul 1989.

[14] DYCK, ROBERT S. VAN, PAUL B. SCHWINBERG and HANS G. DEHMELT: *Electron magnetic moment from geonium spectra: Early experiments and background concepts.* Physical Review D, 34(3):722–736, aug 1986.

[15] DYCK, ROBERT S. VAN, PAUL B. SCHWINBERG and HANS G. DEHMELT: *New high-precision comparison of electron and positrongfactors.* Physical Review Letters, 59(1):26–29, jul 1987.

[16] MAJORITY, FIELD MARSHALL JAMES HARRINGTON HIS: *PhD Thesis (publishment pending).* PhD thesis, University of Heidelberg, 2019.

[17] EARNSHAW, S.: *On the nature of the molecular forces which regulate the constitution of the luminiferous ether.* Trans. Camb. Phil. Soc. 7, 97, 1842.

[18] VOGEL, MANUEL: *Particle Confinement in Penning Traps.* Springer International Publishing, 2018.

[19] BROWN, LOWELL S. and GERALD GABRIELSE: *Precision spectroscopy of a charged particle in an imperfect Penning trap.* Physical Review A, 25(4):2423–2425, apr 1982.

[20] SCHNEIDER, G.: *300 ppt Measurement of the Proton g-Factor*. PhD thesis, Johannes Gutenberg-University in Mainz, 2017.

[21] GABRIELSE, G., L. HAARSMA and S.L. ROLSTON: *Open-endcap Penning traps for high precision experiments.* International Journal of Mass Spectrometry and Ion Processes, 88(2-3):319–332, apr 1989.

[22] ULMER, S.: *First Observation of Spin Flips with a Single Proton Stored in a Cryogenic Penning Trap.* PhD thesis, University of Heidelberg, 2011.

[23] THOMPSON, J. K.: *Two-Ion Control and Polarization Forces for Precise Mass Comparisons.* PhD thesis, Massachusetts Institut of Technology, 2003.

[24] KETTER, JOCHEN, TOMMI ERONEN, MARTIN HÖCKER, SEBASTIAN STREUBEL and KLAUS BLAUM: *First-order perturbative calculation of the frequency-shifts caused by static cylindrically-symmetric electric and magnetic imperfections of a Penning trap.* International Journal of Mass Spectrometry, 358:1–16, jan 2014.

[25] KUYPERS, FRIEDHELM: *Klassische Mechanik.* Wiley VCH Verlag GmbH, 2016.

[26] NAGAHAMA, H., G. SCHNEIDER, A. MOOSER, C. SMORRA, S. SELLNER, J. HARRINGTON, T. HIGUCHI, M. BORCHERT, T. TANAKA, M. BESIRLI, K. BLAUM, Y. MATSUDA, C. OSPELKAUS, W. QUINT, J. WALZ, Y. YAMAZAKI and S. ULMER: *Highly sensitive superconducting circuits at ∼700 kHz with tunable quality factors for image-current detection of single trapped antiprotons.* Review of Scientific Instruments, 87(11):113305, nov 2016.

[27] NAGAHAMA, H.: *High-Precision Measurements of the Fundamental Properties of the Antiproton.* PhD thesis, University of Tokyo.

[28] DEHMELT, H. G. and F. L. WALLS: *"Bolometric" Technique for the rf Spectroscopy of Stored Ions.* Physical Review Letters, 21(3):127–131, jul 1968.

[29] FENG, X., M. CHARLTON, M. HOLZSCHEITER, R. A. LEWIS and Y. YAMAZAKI: *Tank circuit model applied to particles in a Penning trap.* Journal of Applied Physics, 79(1):8–13, jan 1996.

[30] NYQUIST, H.: *Thermal Agitation of Electric Charge in Conductors.* Physical Review, 32(1):110–113, jul 1928.

[31] JOHNSON, J. B.: *Thermal Agitation of Electricity in Conductors.* Physical Review, 32(1):97–109, jul 1928.

[32] SMORRA, C., K. BLAUM, L. BOJTAR, M. BORCHERT, K.A. FRANKE, T. HIGUCHI, N. LEEFER, H. NAGAHAMA, Y. MATSUDA, A. MOOSER, M. NIEMANN, C. OSPELKAUS, W. QUINT, G. SCHNEIDER, S. SELLNER, T. TANAKA, S. VAN GORP, J. WALZ, Y. YAMAZAKI and S. ULMER: *BASE – The Baryon Antibaryon Symmetry Experiment.* The European Physical Journal Special Topics, 224(16):3055–3108, nov 2015.

[33] Cornell, Eric A., Robert M. Weisskoff, Kevin R. Boyce and David E. Pritchard: *Mode coupling in a Penning trap:pulses and a classical avoided crossing.* Physical Review A, 41(1):312–315, jan 1990.

[34] Brown, Lowell S. and Gerald Gabrielse: *Geonium theory: Physics of a single electron or ion in a Penning trap.* Reviews of Modern Physics, 58(1):233–311, jan 1986.

[35] Wineland, D., P. Ekstrom and H. Dehmelt: *Monoelectron Oscillator.* Physical Review Letters, 31(21):1279–1282, nov 1973.

[36] Dehmelt, H.: *Continuous Stern-Gerlach effect: Principle and idealized apparatus.* Proceedings of the National Academy of Sciences, 83(8):2291–2294, apr 1986.

[37] Häffner, H., T. Beier, S. Djekić, N. Hermanspahn, H.-J. Kluge, W. Quint, S. Stahl, J. Verdú, T. Valenzuela and G. Werth: *Double Penning trap technique for precise g factor determinations in highly charged ions.* The European Physical Journal D, 22(2):163–182, feb 2003.

[38] Schwabl, Franz: *Statistical Mechanics (Advanced Texts in Physics).* Springer, 2006.

[39] Press, William H.: *Numerical Recipes in C: The Art of Scientific Computing.* Cambridge University Press, 1997.

[40] Bevington, Philip and D. Keith Robinson: *Data Reduction and Error Analysis for the Physical Sciences.* McGraw-Hill Education, 2002.

[41] Wolf, Roger: *Rechnernutzung in der Physik.* Lecture Notes, 2019.

[42] D'Urso, B., B. Odom and G. Gabrielse: *Feedback Cooling of a One-Electron Oscillator.* Physical Review Letters, 90(4), jan 2003.

[43] Stahl, S, J Alonso, S Djekic, H-J Kluge, W Quint, J Verdu, M Vogel and G Werth: *Phase-sensitive measurement of trapped particle motions.* Journal of Physics B: Atomic, Molecular and Optical Physics, 38(3):297–304, jan 2005.